Final Report

Development of acoustic methods to measure oil droplet size and slick thickness on ROV and AUV platforms

Paul D. Panetta[1,2], Ted Argo[1], Hualong Du[1,2], Donglai Gong[2], L. N. Ferris[2], and Jeanna Kidwell[2]

[1]Applied Research Associates, Inc.

[2] The College of William & Mary, Virginia Institute of Marine Science

Report For

U.S. Department of the Interior
Bureau of Safety and Environmental Enforcement (BSEE)
Sterling, VA

May 31, 2017

This study was funded by the U.S. Department of the Interior, Bureau of Safety and Environmental Enforcement (BSEE), Oil Spill Preparedness Division (OSPD), Washington, DC under Contract Number E15PC00009.

ACKNOWLEDGMENTS

The authors wish to thank the Ohmsett staff for their assistance with this work.

DISCLAIMER

This final report has been reviewed by the Bureau of Safety and Environmental Enforcement (BSEE). Approval does not signify that the contents necessarily reflect the views and policies of the BSEE, nor does mention of the trade names or commercial products constitute endorsement or recommendation for use.

Table of Contents

EXECUTIVE SUMMARY

In this project we have begun the transition of acoustic measurements of slick thickness, gas bubble size distribution, and oil dispersant effectiveness to free swimming ROV and glider platforms. Using a SeaBotix LBV150 ROV vehicle, we have demonstrated the ability to effectively measure both oil slick thickness as well as gas bubble/oil droplet size distribution while operating the ROV in free swimming mode in our labs and at Ohmsett. We also demonstrated the ability to measure the slick thickness using acoustic sensors mounted on a Slocum glider. The oil slick thickness measurements were performed both in the absence of waves as well as the presence of waves. Acoustic transducers were mounted externally on the frame of the ROV and the glider and tethered via cables to data collection and processing hardware.

While the extra sensors and cabling associated with oil slick thickness measurements do impact the performance and flight dynamics of the ROV, proper ballasting and mounting of the sensors allowed the vehicle to remain controllable and flyable. The existing setup could be deployable in an open water setting if the currents and waves are within specific limits.

The measurement of bubble size and oil droplet size distribution required the mounting of a relatively large and heavy low-frequency transducer and receiver on top of the ROV. This sensor configuration severely affected the stability, controllability and flight dynamics of the vehicle. While extensive ballasting measures allow the vehicle to become stable, it was still difficult to control and move. A larger ROV would be able to deal with the size and mass of the low frequency sensor much more effectively. For the purposes of research deployment at Ohmsett, the setup was functional but unlike the measurement of oil slick thickness, it would be too difficult to use in an open water deployment scenario.

To better understand the influence of sea state on vehicle motion and thus measurement precision, the team designed and built a custom inertial motion sensor package to quantify the motion of the vehicle while making oil slick thickness measurements as well as subsurface measurements of gas bubble distribution measurement and dispersant effectiveness.

The technical progress made to measure the gas bubble size distribution using acoustic backscattering is significant and opens the opportunity to provide gas bubble size measurements as well as oil dispersant effectiveness from a single set of acoustic sensors on a single platform. The measurements of oil droplet scattering related to dispersant efficiency show the proof of concept from ROV platforms and produced results similar to static platforms from previous work. We advanced these capabilities to TRL 6 through multiple measurements at Ohmsett in many spill scenarios including surface slicks in various sea states and subsurface releases of methane and dispersed oil.

1. OVERVIEW AND OBJECTIVE

Combatting oil spills requires an array of instruments and methods to improve collection and physical removal of oil from the environment, burning the oil, or dispersing the oil into the water column. Ensuring that instrumentation exists to characterize the oil is crucial for responding to both surface spills as well as subsurface releases of oil and gas. To help improve oil spill response, we are developing acoustic measurements of the thickness of an oil slick the droplet size distributions of oil and gas. Mapping the slick thickness will help direct spill responders to the thickest areas of the slick and can be used to measure the burn rate and efficiency during In-Situ Burning (ISB), measuring the oil droplet size distribution and gas bubble size distribution at the source of a subsurface release, throughout the water column, and just below a slick to monitor the effect of aerial or surface applications of dispersant will help determine dispersant efficiency and provide input into fate and transport models. The goal of this project is to begin the transfer of acoustic methods for measurement of slick thickness and oil droplet and bubble size distributions from static platforms to free swimming ROV and AUV platforms. The technical objectives of this program are to optimize the measurement electronics and begin compensating for the relative motion of the free-swimming platforms and the slick surface.

To address this goal, measurement methods previously developed for slick thickness, oil droplet sizing, and bubble size distribution measurement were integrated onto an ROV platform. Three weeks of testing in the simulated spill environment at Ohmsett provided an opportunity to test, evaluate, and improve all three of these measurement methods while for various aspects of the potential operational environments including sea states, slick thicknesses, and slick configuration. In addition, measurements of the temperature-dependent speed of sound in various oils was measured to aid in determining the slick thickness in various environments. In the following sections, a description of the slick thickness measurements using Alaska North Slope (ANS) crude oil and subsurface release measurements of ANS dispersed with Corexit 9500, air bubbles, and methane bubbles, will be presented. Results of these measurements and implications for future implementation of this technology will be discussed.

2. SLICK THICKNESS MEASUREMENTS FROM ROV AND AUV PLATFORMS

2.1. OHMSETT TANK SETUP

We accomplished this goal through several measurements of surface slicks and subsurface releases at our lab and during three trips to Ohmsett. For our work at Ohmsett the oil in the tank was arranged as shown in Figure 1.

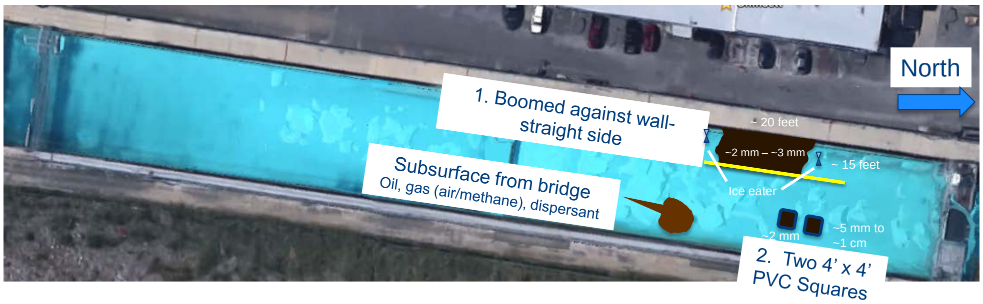

Slicks
1. Boomed against wall– straight edge
2. Contained with Ice Eaters
2. Two 4 foot x 4 foot PVC squares

Oil: ANS

Subsurface releases

- Oils: ANS ~ 1+ L/min
- Dispersant: Corexit 9500
- Methane
- Nozzle in vertical position ~ 3 feet from vertical mast
- Bubbler beneath nozzle

Figure 1. The tank at Ohmsett was configured with various surface slicks and subsurface releases during each of the three weeks the ARA team was performing measurements.

2.2. OIL CONFIGURATION

We performed measurements with two different boom configurations in sea states 0 to 3. In one configuration the boom was placed along the side of the tank and corralled with ice eaters as shown in Figure 2. The oil did not form a uniform slick on the surface as it spread out and moved around the boomed area due to wind and wave action. Typically, between 70 L to 132 L of oil was placed in the boomed region resulting in slick thicknesses of approximately 3 mm and 5 mm, respectively. The setup showing the arbitrary shaped boomed region are in Figure 3 and Figure 4.

Figure 2. A linear boomed area was filled with 70 L to 132 L of ANS oil and contained with ice eaters at either end to prevent oil loss during testing.

Figure 3. The arbitrary shaped boom configuration tested at Ohmsett more closely simulated an operational environment by allowing for more maneuverability under the slick, less control over the surface area and slick thickness.

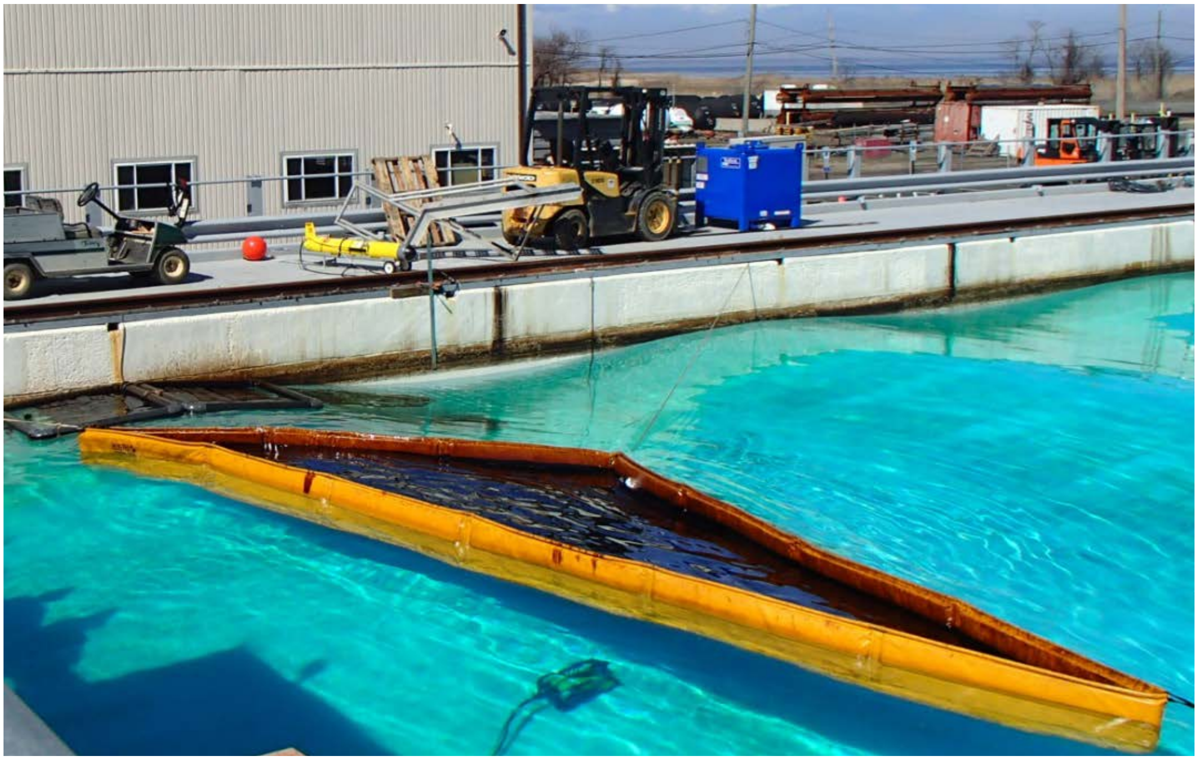

Figure 4. Upon collapsing to its minimum surface area, the arbitrary boom slick allowed measurements of a thicker slick.

Multiple acoustic transducers were mounted to the ROV and glider platforms as shown in Figure 5. The sensors were mounted at various angles to accommodate for the pitch and roll of the ROV and the motion of the glider as it yos through the water column and the motion of the surface of the slick due to the waves. A more detailed description of the angles will be given in a latter section. A schematic of the acoustic beams propagating through the water column under the waves is shown in Figure 9 for the ROV and glider platforms.

Figure 5. Configurations of the acoustic sensors on the ROV and glider platforms

Figure 6. Waves varied in height throughout the experiments at Ohmsett; the waves made during Test 14 had a mean height of 15.9 Inches and wavelength of 39.8 Feet.

Figure 7. Waves varied in height throughout the experiments at Ohmsett; the waves made during Test 17 had a mean height of 21.4 Inches and wavelength of 39.3 Feet.

Figure 8. Waves varied in height throughout the experiments at Ohmsett; the harbor chop made during Test 20C had a mean height of 6.0 Inches and wavelength of 11.6 Feet

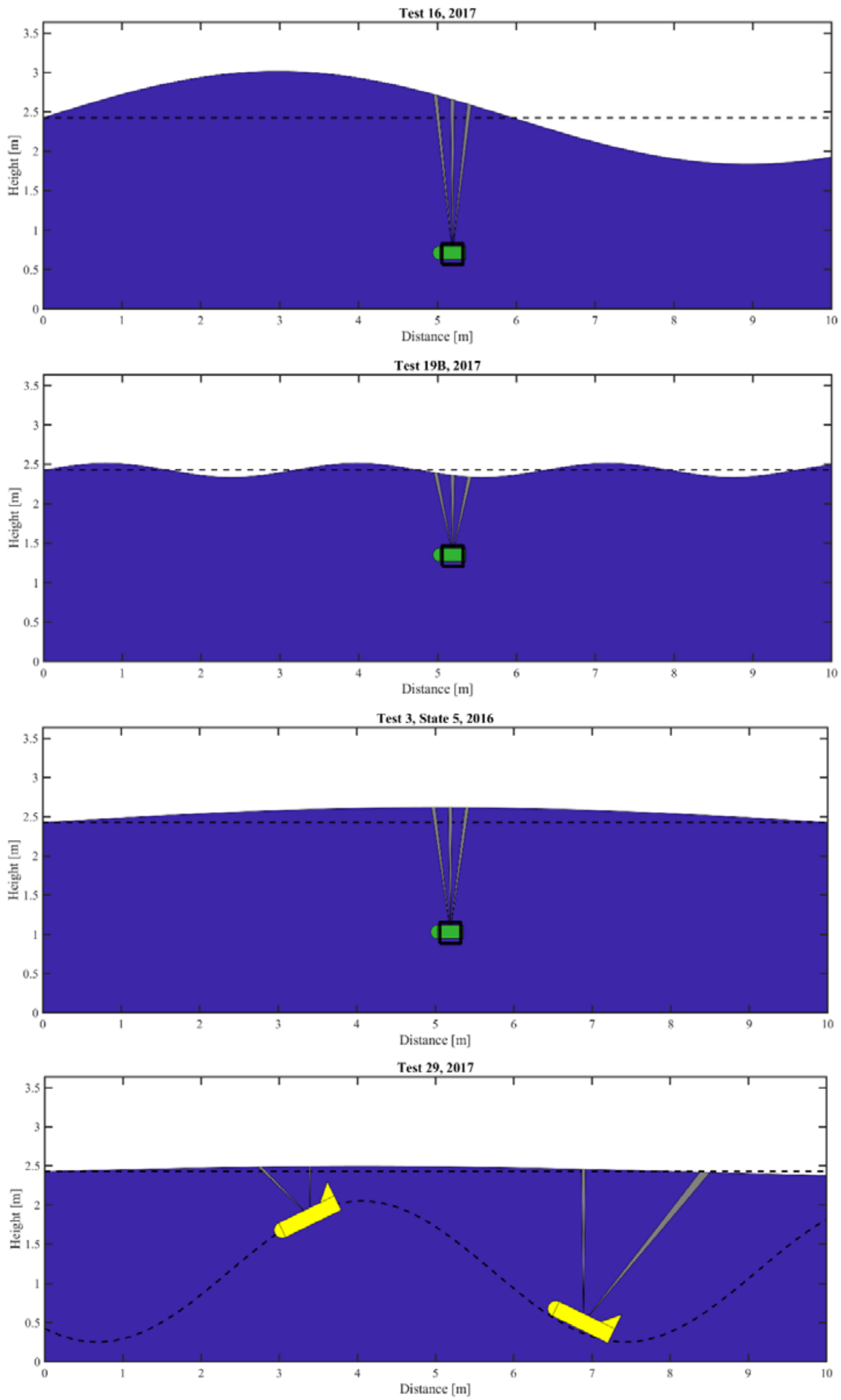

Figure 9. Slick thickness was measured from ROV and AUV platforms in sea states with the following extremes (from top to bottom): Sea State 3 at 0.56 meter wave height, Sea State 1 Harbor Chop, Sea State 2 at 10.3 meter wavelength, and Sea State 1 at 16.4 meter wavelength.

To successfully transition these measurements to the open water to help with a real spill requires operation in multiple sea states. Sample sea states are shown in Figure 6 through Figure 8. The extremes of the sea states experienced throughout this testing are depicted, to scale, in Figure 9 for the highest sea state, shortest wavelength, and longest wavelength tested with the ROV, and a representative sea state tested with the glider.

Figure 10 and Figure 11 show the sea states where the acoustic measurements measured the slick thickness at Ohmsett. Figure 10 shows the average wave height vs wavelength for a given measurement period and Figure 11 shows the highest 1/3 of the waves. The sea states included no waves, harbor chop with small heights and short wavelengths and traveling waves with amplitudes as over 0.5 meters and wavelengths over 20 meters. The World Meteorological Organization Sea State ranged from 0 where no waves were present to a Sea State 3.

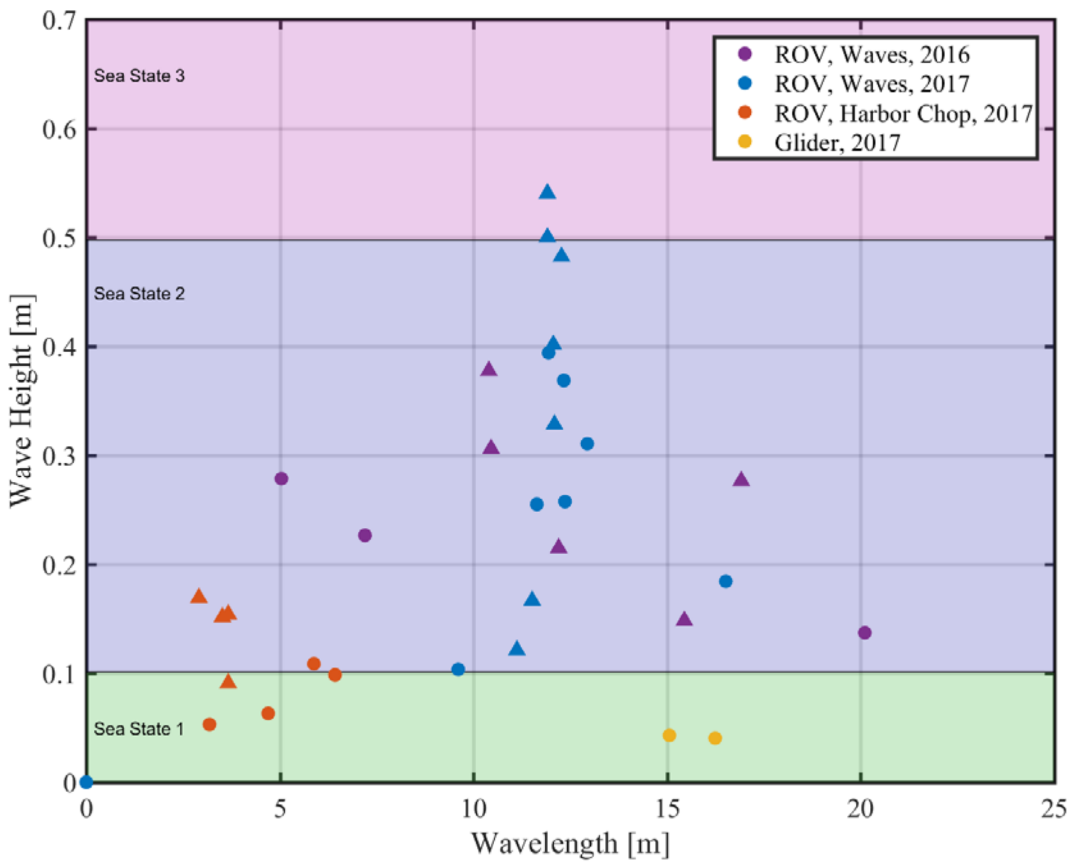

Figure 10. Slick thickness measurements were performed in a variety of sea states for a variety of wavelengths. The sea state, based on mean wave height, is presented here for each collection of tests. Circles and triangles represent separate days of testing within each test paradigm denoted by different colors.

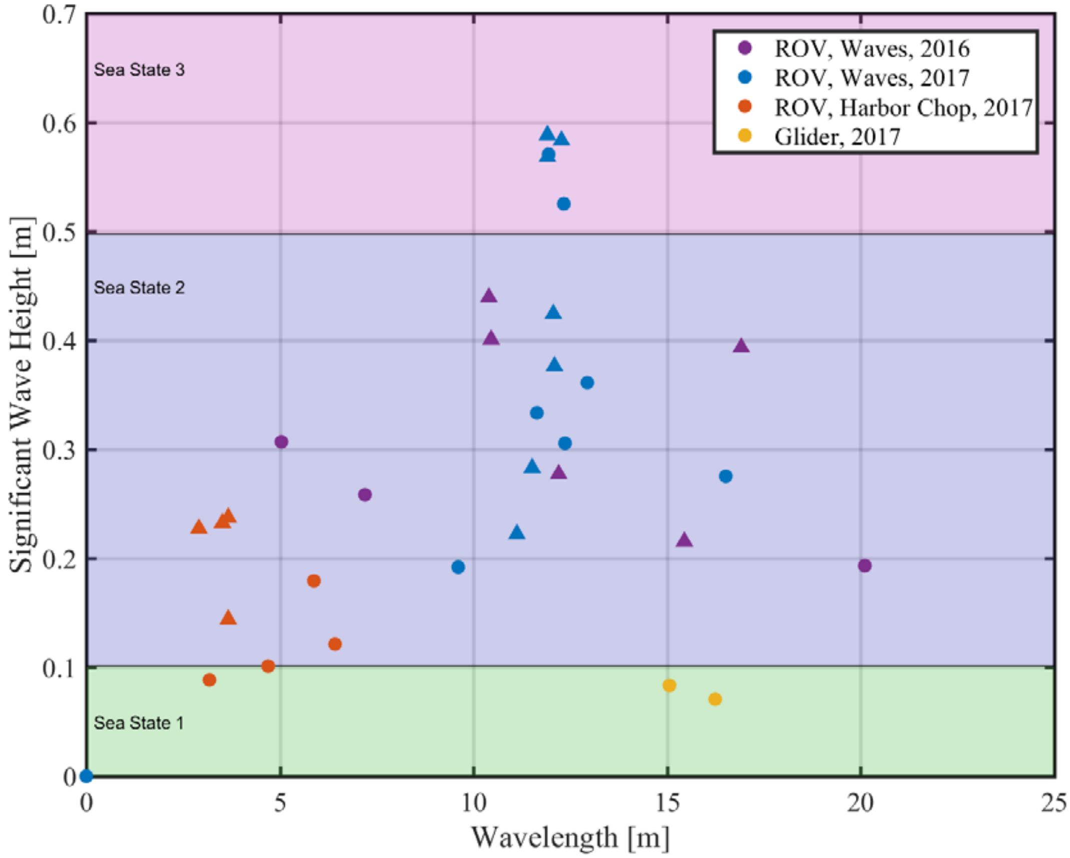

Figure 11. Slick thickness measurements were performed in a variety of sea states for a variety of wavelengths. The sea state, based on the highest one third of waves, is presented here for each collection of tests. Circles and triangles represent separate days of testing within each test paradigm denoted by different colors.

The detailed specifications of these sea states along with the dates of our measurements are shown in Table 1.

Table 1. All wave states studied under this program includes data from February 2016 and March 2017.

Year	Test #	Oil Volume (L)	Mean Wave Height (inches)	Significant Wave Height (top 1/3) (inches)	Average Wavelength (feet)	World Meteorological Organization Sea State*
Sine Waves						
2016	1.1		5.6	7.7	66.4	2 (Smooth)
2016	1.2		5.4	7.7	66.4	2 (Smooth)
2016	2.1		5.8	10.2	23.8	2 (Smooth)
2016	2.2		6.8	10.2	23.8	2 (Smooth)
2016	2.3		5.4	10.2	23.8	2 (Smooth)
2016	2.4		5.5	10.2	23.8	2 (Smooth)
2016	2.5		6.2	10.2	23.8	2 (Smooth)
2016	2.6		6.3	10.2	23.8	2 (Smooth)
2016	2.7		6.3	10.2	23.8	2 (Smooth)
2016	2.9		6.2	10.2	23.8	2 (Smooth)
2016	2.10		6.4	10.2	23.8	2 (Smooth)
2016	2.11		6.7	10.2	23.8	2 (Smooth)
2016	3.1		6.9	12.2	16.6	2 (Smooth)
2016	3.2		6.2	12.2	16.6	2 (Smooth)
ANS, Arbitrary Boom, Sine Waves						
2016	1		1.6	0.0	0.0	0 (Calm)
2016	2		1.5	8.5	51.0	2 (Smooth)
2016	2A		1.9	11.0	51.0	2 (Smooth)
2016	2B		2.1	11.0	51.0	2 (Smooth)
2016	3		1.9	15.6	40.3	2 (Smooth)
2016	3A.1		2.2	15.6	40.3	2 (Smooth)
2016	3A.2		2.2	15.6	40.3	2 (Smooth)
2016	3A.3		2.2	15.6	40.3	2 (Smooth)
ANS, Parallel Boom, Sine Waves						
2016	5.2		5.5	15.9	34.5	2 (Smooth)
2016	5.3		5.4	15.9	34.5	2 (Smooth)
2016	5.4		5.8	15.9	34.5	2 (Smooth)
2016	6.1		5.1	17.4	34.3	2 (Smooth)
2016	6.2		5.2	17.4	34.3	2 (Smooth)
2016	6.3		4.0	17.4	34.3	2 (Smooth)
Sine waves						
2017	4	70	10.1	13.2	38.4	2 (Smooth)
2017	5	70	10.2	12.1	40.8	2 (Smooth)
2017	6	70	12.3	14.3	42.7	2 (Smooth)
2017	7	70	7.3	10.9	54.5	2 (Smooth)
2017	8	70	14.6	20.8	40.7	3 (Slight)
2017	9	70	15.6	22.6	39.4	3 (Slight)
2017	10	70	4.1	7.6	31.7	1 (Calm)
2017	11	132	No Waves			0 (Calm)
2017	12	132	19.1	23.1	40.5	3 (Slight)
2017	13	132	13.0	14.9	39.9	2 (Smooth)
2017	14	132	15.9	16.8	39.8	2 (Smooth)
2017	15	132	4.8	8.8	36.7	2 (Smooth)
2017	16	132	19.8	22.5	39.3	3 (Slight)
2017	17	132	21.4	23.3	39.3	3 (Slight)
2017	18	132	6.6	11.2	38.0	2 (Smooth)
Harbor Chop State 1						
2017	19A	132	3.9	4.8	21.2	2 (Smooth)
2017	19B	132	2.1	3.5	10.5	1 (Calm)
2017	19C	132	2.5	4.0	15.5	2 (Smooth)
2017	19D	132	4.3	7.1	19.4	2 (Smooth)
Harbor Chop State 2						
2017	20A	132	6.7	9.0	9.6	2 (Smooth)
2017	20B	132	6.1	9.4	12.1	2 (Smooth)
2017	20C	132	6.0	9.2	11.6	2 (Smooth)
2017	20D	132	3.6	5.7	12.1	2 (Smooth)
2017	20E	132	No Waves			0 (Calm)
Sine waves						
2017	29	132	1.6	2.8	53.6	1 (Calm)
2017	30	132	1.7	3.3	49.7	1 (Calm)

*Based on Significant Wave Height (top 1/3) as defined by the World Meteorological Organization sea state code, https://en.wikipedia.org/wiki/Sea_state

2.3. ACOUSTIC MEASUREMENT OF SLICK THICKNESS

Data was collected by flying the platforms under the slick at various heights similar to previous work for BSEE [Panetta et al.] where we developed an ROV which rolled along the bottom of the tank. The free swimming platforms offered a more realistic deployment scenario and thus provided the opportunity to study the effects of the motion of the platforms and the surface of the slick. Figure 12 shows a “sonar-like” image of the reflection from the water surface and the slick surfaces. The slick is most visible as multiple reflections around 10 seconds and in the 30 to 70 second range. A closer look at the raw ultrasonic time-domain signal in Figure 13 shows the reflection from the bottom of the slick arriving first followed by the reflection from the top of the slick. The third signal is a reverberation inside the slick. To calculate the thickness we calculated the difference in the arrivals of the bottom and top of the slick.

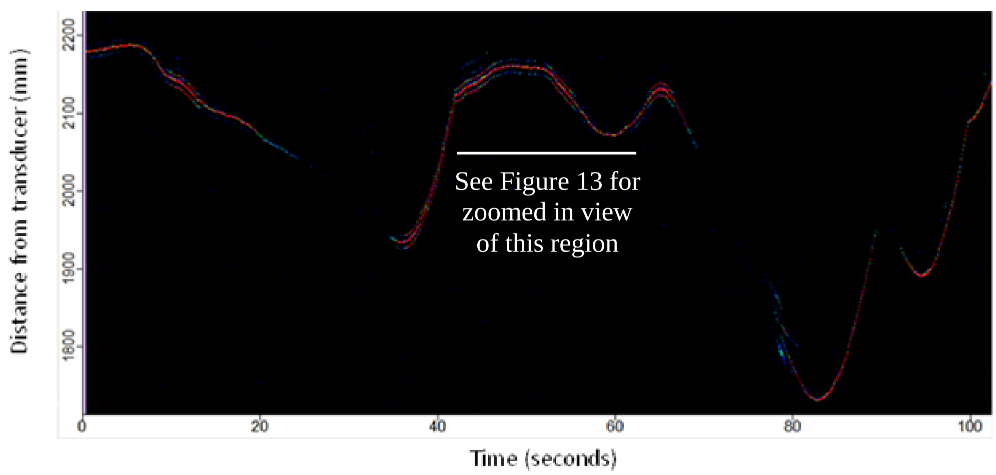

Figure 12. The acoustic signals from the surface and the slick in the sonar-like image of the slick from the glider platform shows the motion of the glider platform as it is tilted up and down independent of waves.

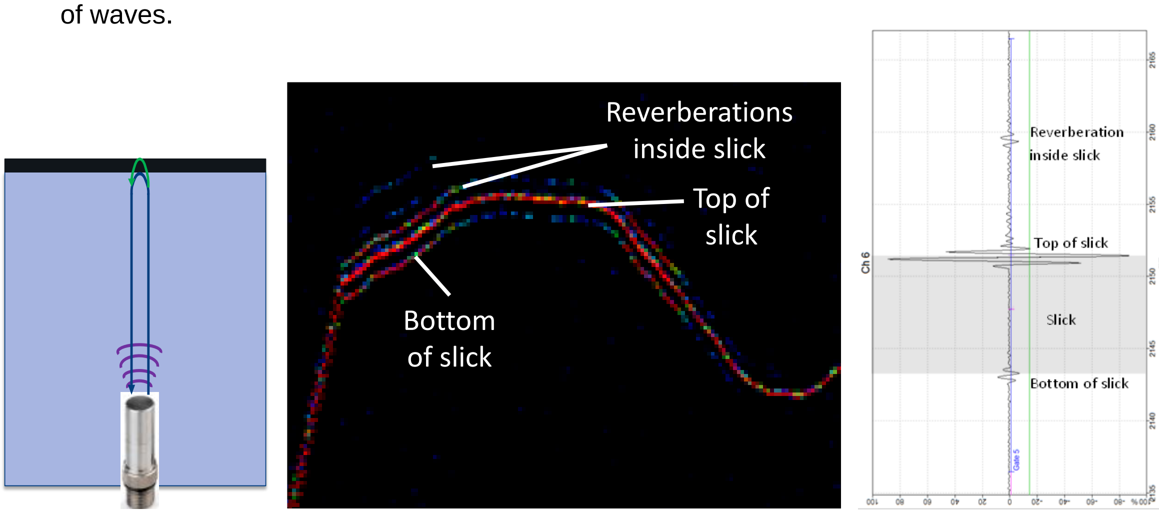

Figure 13: Schematic of measurement, zoomed in region of reflections from slick in the 40 to 60 second region and a typical acoustic “ping” from the glider platform showing a slick approximately 7.5mm thick.

2.4. SPEED OF SOUND OF OIL AS A FUNCTION OF TEMPERATURE

The acoustic wave speed in oil is significantly affected by the temperature. Thus knowing speed of sound is necessary to accurately determine the thickness of the slick. Figure 14 shows the experimental set up for measuring the speed of sound as a function of temperature. The oil chamber was fabricated from stainless steel and surrounded with insulation. Thermal insulation fibers were used to wrap the 3.5'' diameter cylindrical stainless tube to keep the temperature of the oil constant. The stainless tube was welded onto a 7.0'' diameter steel plate and placed on a hot plate to heat the oil. An acoustic transducer mounted on a 5-axis positioning system was lowered through a central hole in the top thermal insulation cap and transmitted the acoustic signal into the oil and received the reflection from the bottom of the oil filled container. Three thermocouples were mounted in the insulated cap to measure temperatures at different depths in oil. The temperature was collected by the National Instruments data collection device and acquired simultaneously with the acoustic data. Figure 15 shows a closer view of the inside of the oil chamber. Figure 16 shows three thermocouples mounted through the insulated cap for measuring the temperature in the oil at different depths.

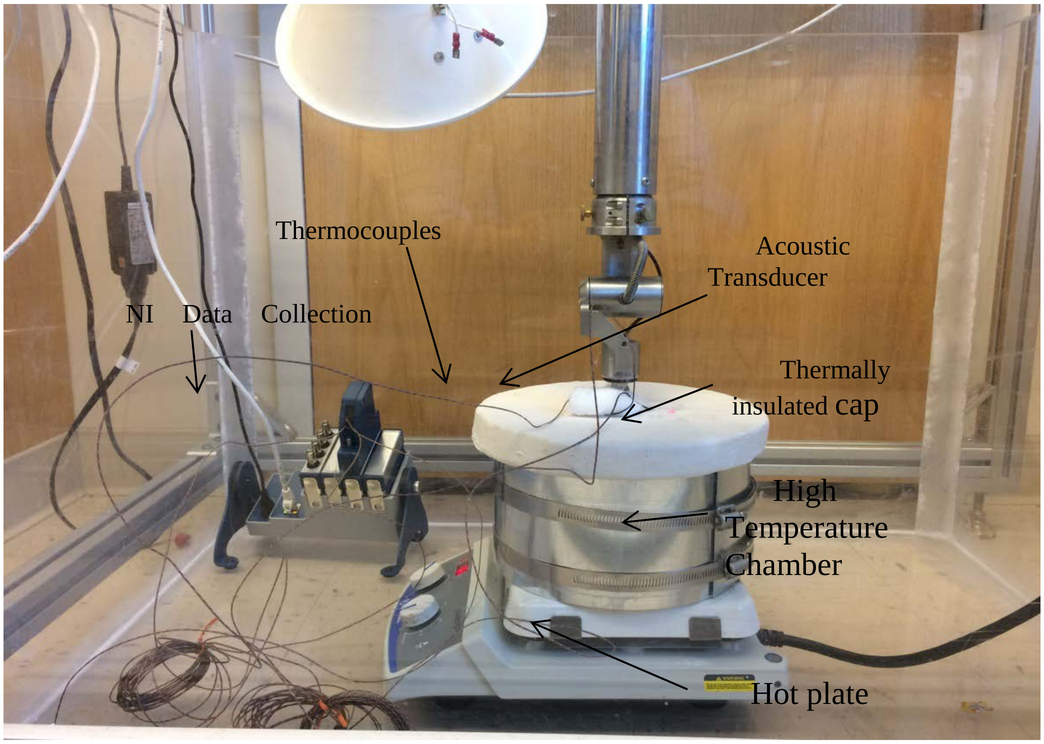

Figure 14. The experimental setup for measuring compression wave speed in oil at high temperature was maintained using an insulated vessel on a hot plate.

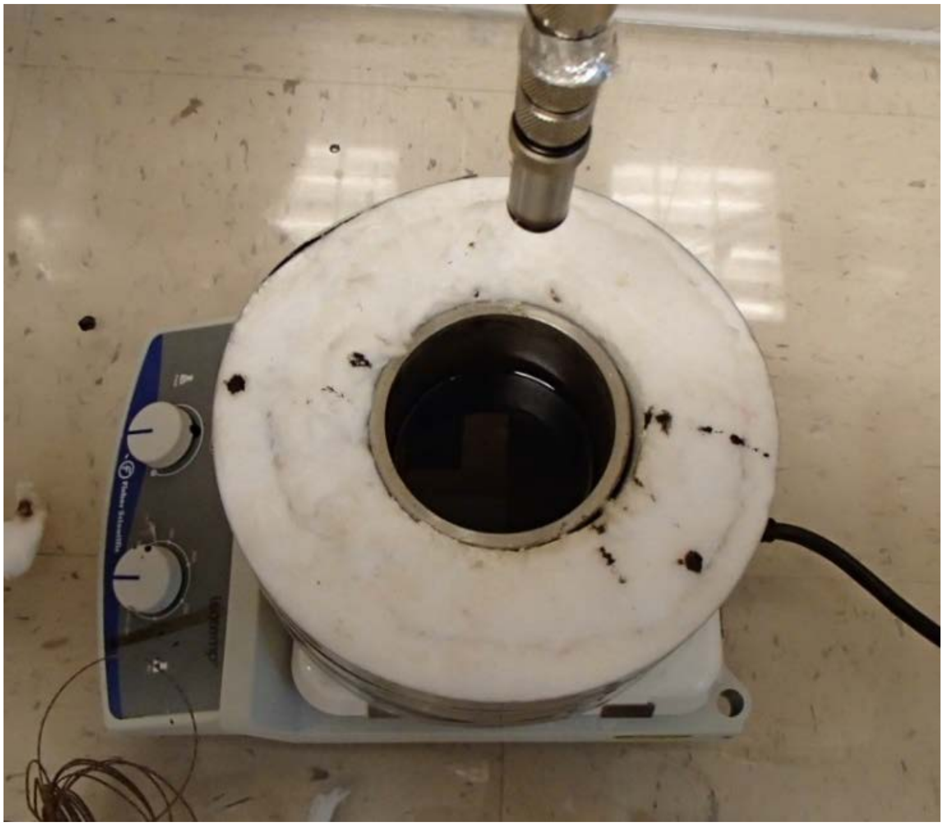

Figure 15. The cylindrical oil container was wrapped with insulation fiber to maintain temperature.

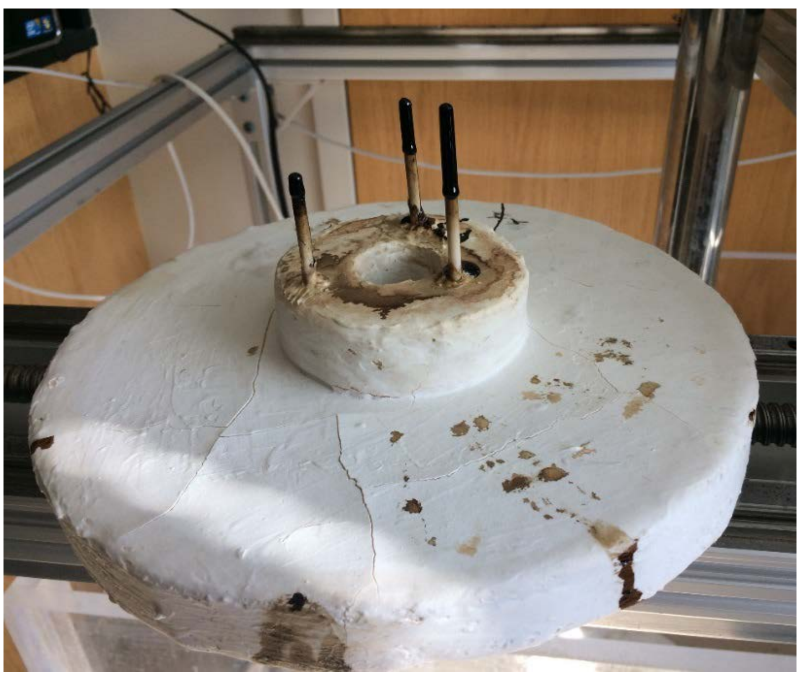

Figure 16. The thermal insulation cap for the oil container supported three protruding thermocouples.

Figure 17 shows the dependence of the measured speed of sound on temperature from 30°C to 180°C in ANS, Dorado and Rock crude oils.

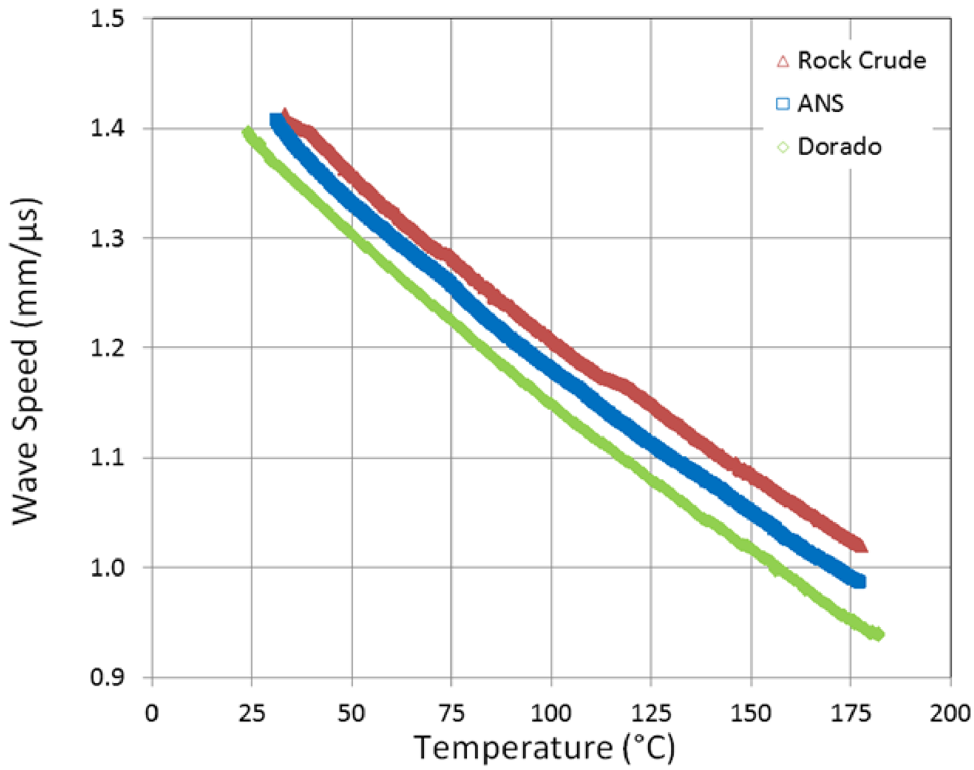

Figure 17. Wave speed Vs. Temperature in various crude oils demonstrate a change of nearly 40% over the 25 to 180 degree temperature range.

2.5. ROV MEASUREMENT OF SLICK THICKNESS

2.5.1. ROV acoustic sensor set up, and deployment

Multiple acoustic transducers were mounted on the ROV to account for the relative motion of ROV and the slick. Figure 18 shows our final configuration of six acoustic transducers with a center frequency of 2.25 MHz mounted to the ROV. Three were attached on the left side with angles (-15°, 0, 15°) to accommodate the pitch of the ROV and three were attached to the back of the ROV with angles (-10°, 0, 10°) to accommodate the roll of the ROV. These angles were chosen based on the results from our measurements in waves at Ohmsett and at our facility at VIMS in Gloucester Point, VA.

Figure 18. Side, top, and back views of the ROV showing the placement of the acoustic transducers mounted at various angles to account for the pitch and roll of the ROV platform.

Images of the ROV are shown in Figure 19 at two different depths. As the acoustic beam propagates through the water from the small transducer, it diverges causing the acoustic “spot size” on the surface of the slick to increase with increasing distance. To determine if the spot size affects the ability of the acoustics to measure the slick thickness for various sea states we performed measurements at two different depths, 1.2 m and 1.8 m as shown in Figure 19.

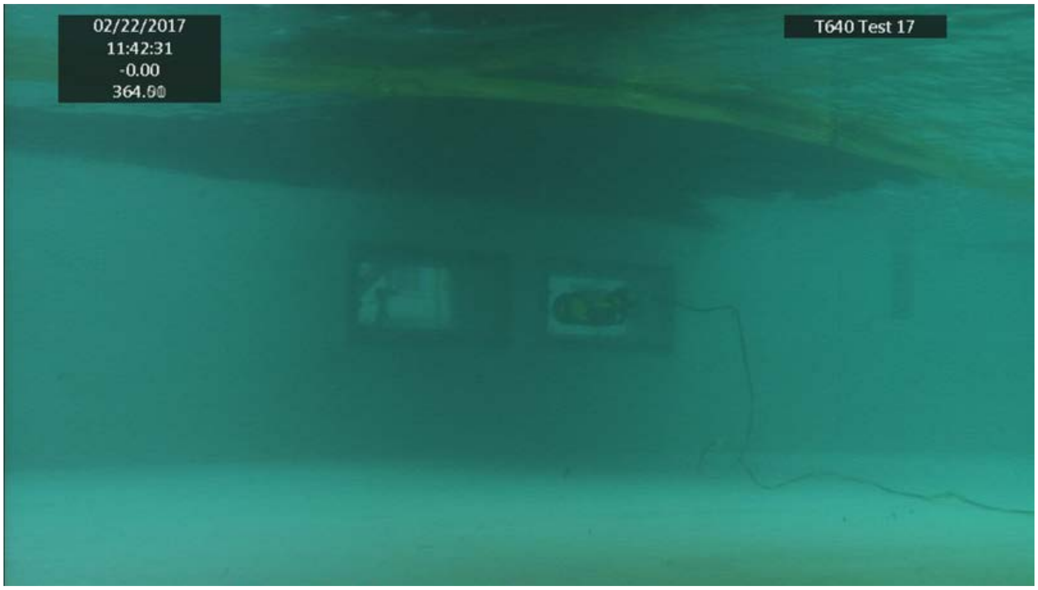

Figure 19. The ROV performed acoustic measurements of oil slick thickness at two depths – 1.2 meters (top) and 1.8 meters (bottom).

At these depths, the spot size on the surface of the slick is 10.7 cm (4.1 inches) and 15.7 cm (6.2 inches), respectively. Figure 20 shows a schematic of these depths along with the theoretical prediction of the beam diameter as a function of distance assuming the beam has a Gaussian shape. The pictures are not to scale. Details of these calculations are in previous reports. We found no significant effect on the resultant slick thickness from performing measurements at these two depths for the sea states we studied. For transition to open water, the beam diameter and the interaction with real waves will be an important topic to study.

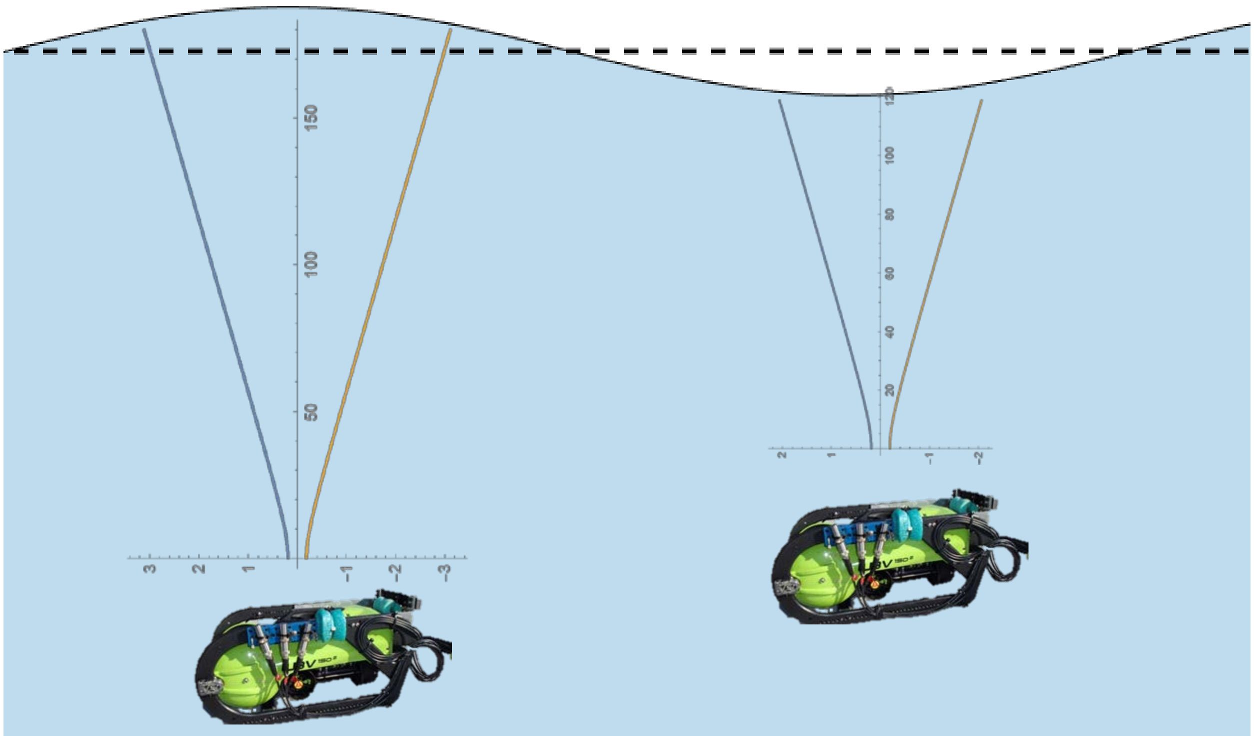

Figure 20. The spot size of the acoustic beam on the surface increases as depth increases, though measurements were successfully made using the spot sizes experienced in this program with the sea states studied.

2.5.2. Slick thickness results from ROV platform

The slick thickness was measured using the ROV in the sea states described in Table 2 along with the thicknesses obtained.

Table 2. The table of all surface slick measurements performed under this program including slick thickness data from February 2016 and March 2017.

Year	Test #	Oil Volume (L)	Mean Wave Height (inches)	Significant Wave Height (top 1/3) (inches)	Average Wavelength (feet)	World Meteorological Organization Sea State*	Thickness		
							Average (mm)	Range (mm)	Standard Deviation (mm)
Sine Waves									
2016	1.1		5.6	7.7	66.4	2 (Smooth)	5.6	1.3	0.3
2016	1.2		5.4	7.7	66.4	2 (Smooth)	5.4	1.8	0.3
2016	2.1		5.8	10.2	23.8	2 (Smooth)	5.8	1.5	0.2
2016	2.2		6.8	10.2	23.8	2 (Smooth)	6.8	1.8	0.3
2016	2.3		5.4	10.2	23.8	2 (Smooth)	5.4	3.6	0.8
2016	2.4		5.5	10.2	23.8	2 (Smooth)	5.5	3.1	0.4
2016	2.5		6.2	10.2	23.8	2 (Smooth)	6.2	2.9	0.4
2016	2.6		6.3	10.2	23.8	2 (Smooth)	6.3	1.1	0.2
2016	2.7		6.3	10.2	23.8	2 (Smooth)	6.3	1.6	0.4
2016	2.9		6.2	10.2	23.8	2 (Smooth)	6.2	1.0	0.3
2016	2.10		6.4	10.2	23.8	2 (Smooth)	6.4	1.1	0.2
2016	2.11		6.7	10.2	23.8	2 (Smooth)	6.7	1.4	0.4
2016	3.1		6.9	12.2	16.6	2 (Smooth)	6.9	1.5	0.4
2016	3.2		6.2	12.2	16.6	2 (Smooth)	6.2	2.1	0.6
ANS, Arbitrary Boom, Sine Waves									
2016	1		1.6	0.0	0.0	0 (Calm)	1.6	1.1	0.1
2016	2		1.5	8.5	51.0	2 (Smooth)	1.5	2.7	0.6
2016	2A		1.9	11.0	51.0	2 (Smooth)	1.9	1.5	0.4
2016	2B		2.1	11.0	51.0	2 (Smooth)	2.1	1.7	0.5
2016	3		1.9	15.6	40.3	2 (Smooth)	1.9	1.8	0.5
2016	3A.1		2.2	15.6	40.3	2 (Smooth)	2.2	1.8	0.5
2016	3A.2		2.2	15.6	40.3	2 (Smooth)	2.2	1.8	0.6
2016	3A.3		2.2	15.6	40.3	2 (Smooth)	2.2	2.0	0.5
ANS, Parallel Boom, Sine Waves									
2016	5.2		5.5	15.9	34.5	2 (Smooth)	5.5	4.4	1.4
2016	5.3		5.4	15.9	34.5	2 (Smooth)	5.4	4.7	1.4
2016	5.4		5.8	15.9	34.5	2 (Smooth)	5.8	4.1	1.0
2016	6.1		5.1	17.4	34.3	2 (Smooth)	5.1	3.5	1.2
2016	6.2		5.2	17.4	34.3	2 (Smooth)	5.2	3.2	0.9
2016	6.3		4.0	17.4	34.3	2 (Smooth)	4.0	3.4	0.8
Sine waves									
2017	4	70	10.1	13.2	38.4	2 (Smooth)	2.8	1.8	0.3
2017	5	70	10.2	12.1	40.8	2 (Smooth)	3.4	3.0	0.5
2017	6	70	12.3	14.3	42.7	2 (Smooth)	3.3	3.8	1.2
2017	7	70	7.3	10.9	54.5	2 (Smooth)	3.0	4.3	1.0
2017	8	70	14.6	20.8	40.7	3 (Slight)	3.3	3.7	1.0
2017	9	70	15.6	22.6	39.4	3 (Slight)	2.9	3.7	1.0
2017	10	70	4.1	7.6	31.7	1 (Calm)	3.1	3.4	1.0
2017	11	132	No Waves			0 (Calm)	no data		
2017	12	132	19.1	23.1	40.5	3 (Slight)	4.2	3.6	1.0
2017	13	132	13.0	14.9	39.9	2 (Smooth)	4.0	2.6	0.8
2017	14	132	15.9	16.8	39.8	2 (Smooth)	5.0	3.1	0.7
2017	15	132	4.8	8.8	36.7	2 (Smooth)	4.7	4.2	0.9
2017	16	132	19.8	22.5	39.3	3 (Slight)	4.5	3.3	0.9
2017	17	132	21.4	23.3	39.3	3 (Slight)	5.4	3.8	1.1
2017	18	132	6.6	11.2	38.0	2 (Smooth)	4.8	4.2	1.0
Harbor Chop State 1									
2017	19A	132	3.9	4.8	21.2	2 (Smooth)	3.8	3.5	0.8
2017	19B	132	2.1	3.5	10.5	1 (Calm)	4.2	3.5	1.0
2017	19C	132	2.5	4.0	15.5	2 (Smooth)	3.8	3.5	0.9
2017	19D	132	4.3	7.1	19.4	2 (Smooth)	4.1	3.5	0.9
Harbor Chop State 2									
2017	20A	132	6.7	9.0	9.6	2 (Smooth)	4.0	3.2	0.8
2017	20B	132	6.1	9.4	12.1	2 (Smooth)	3.2	3.4	0.9
2017	20C	132	6.0	9.2	11.6	2 (Smooth)	3.6	3.5	1.0
2017	20D	132	3.6	5.7	12.1	2 (Smooth)	3.2	6.4	1.2
2017	20E	132	No Waves			0 (Calm)	6.9	2.7	0.8
Sine waves									
2017	29	132	1.6	2.8	53.6	1 (Calm)	3.8	3.7	1.1
2017	30	132	1.7	3.3	49.7	1 (Calm)	4.3	3.8	1.2

*Based on Significant Wave Height (top 1/3) as defined by the World Meteorological Organization sea state code, https://en.wikipedia.org/wiki/Sea_state

For brevity we will present the detailed results of the acoustic measurements of slick thickness in calm water and for Tests 6, 11, 15, 16, 17, 18 which covers the range of wave heights from 0 inches to 23.5 inches. An example of the measurements for calm water are shown in Figure 21 for the transducer mounted in the center of the back of the ROV. The reflection from the surface was measurable throughout the data collection time and the slick was measureable for most of that time. The top pane of Figure 21 shows the time of arrival of the acoustic reflections versus measurement time and the bottom pane shows a single acoustic signal depicting (1) the reflection from bottom of the slick, (2) the reflection from the top of the slick, and (3) the reverberation inside the slick. Two regions labeled “Gate 2” and “Gate 3” highlight the reflection from the bottom of the slick and the reverberation inside the slick, respectively. The large signal in the center is the reflection for the top of the slick at the oil-air interface.

The reflection from the oil slick surface was dynamically changing throughout the measurement due to surface and ROV motion, especially when waves were applied, resulting in reflections from the bottom of the slick which were not always clearly separated from the reflection from the surface or the electronic noise. Therefore, we selected signals with visible and clear separation between these returns for processing and optimized the analysis algorithm to calculate the slick thickness using the time difference between the reflections of the top and bottom of the slick. The following figures show the measurements of oil slick thickness as a function of measurement time using the zero degree roll transducer mounted in the back of the ROV for each test.

For Test 15 through 20E, the ROV was moved closer to the water surface to decrease the spot sizes of acoustic transducers at the water surface. The goal was to diminish the negative effects of dynamic wave surfaces on the reflection from the oil slick so that more usable signals were collected in the following tests. Based on this limited data set no effect due to depth was observed.

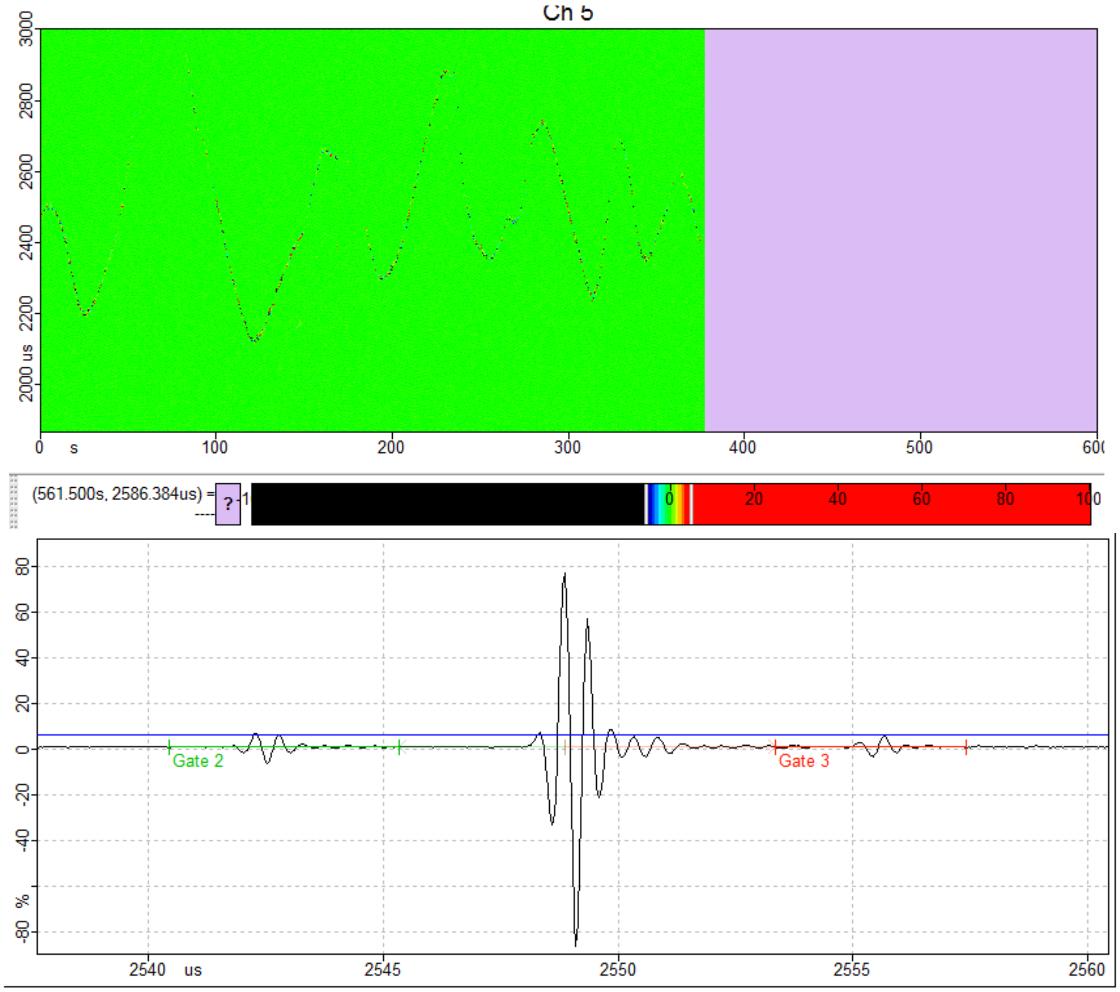

Figure 21 Acoustic measurements of oil slick thickness from the zero degree roll transducer for calm water show the arrival of the individual acoustic signals versus time (top) and a single acoustic return (bottom).

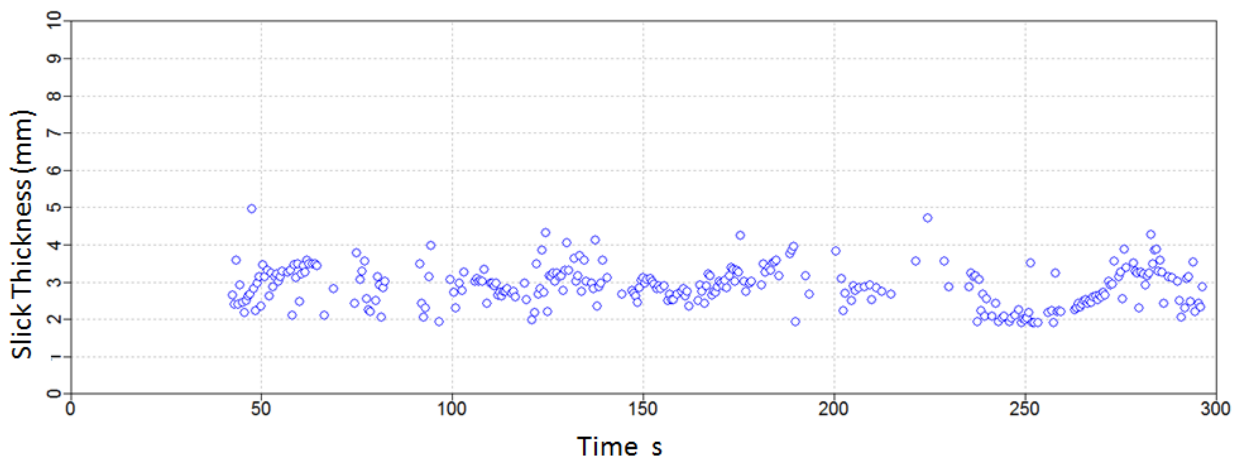

Figure 22. The measured oil slick thickness without waves in Test 3 was approximately 3.5 mm.

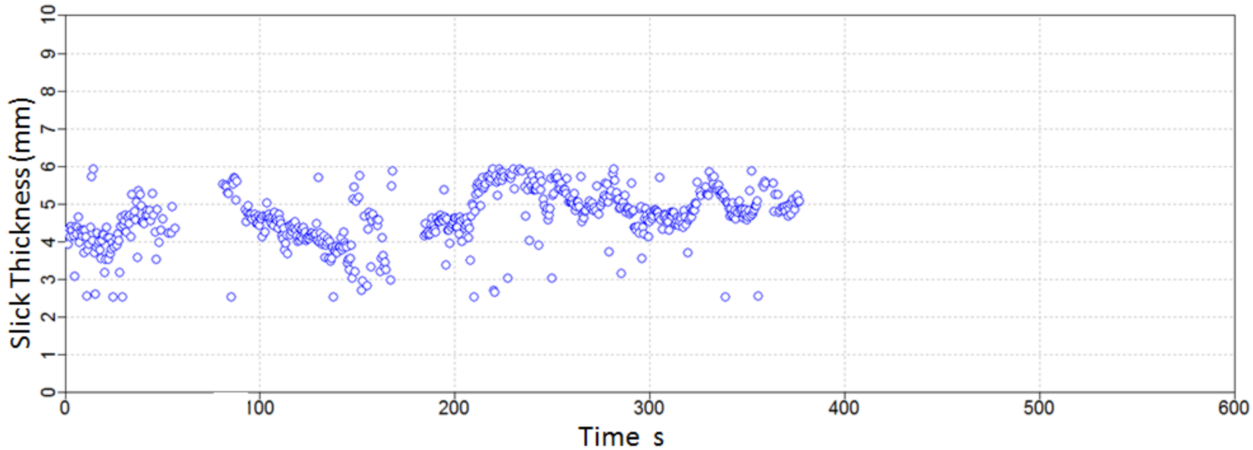

Figure 23. The measured oil slick thickness without waves in Test 11 was approximately 5 mm.

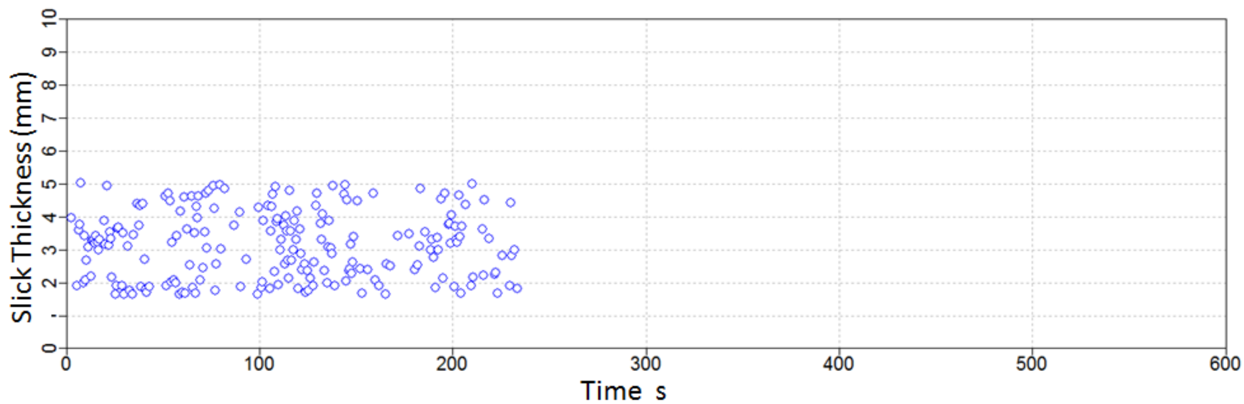

Figure 24. The measured oil slick thickness for waves as high as 14 inches in Test 6 was approximately 4.5 mm.

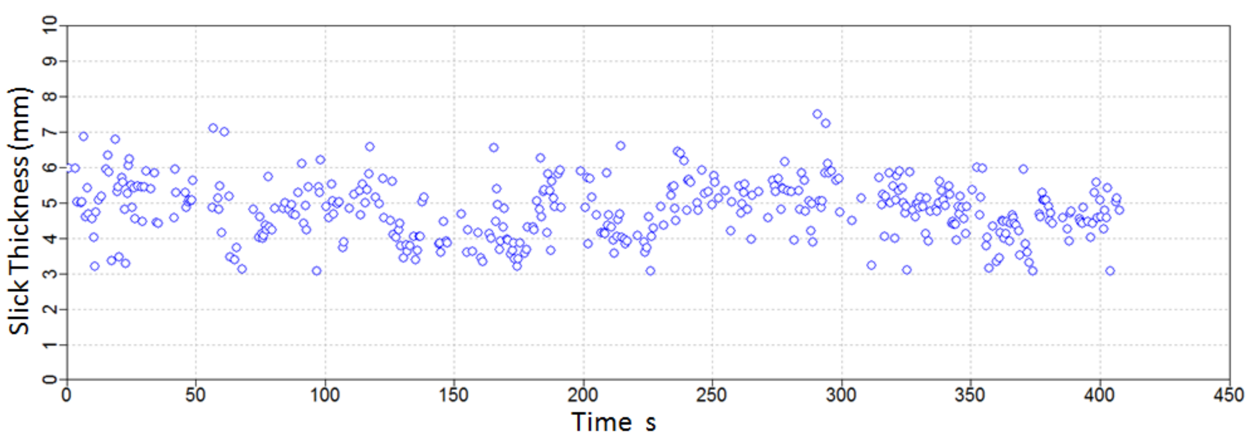

Figure 25. The measured oil slick thickness for waves as high as 8.8 inches in Test 15 was approximately 5 mm.

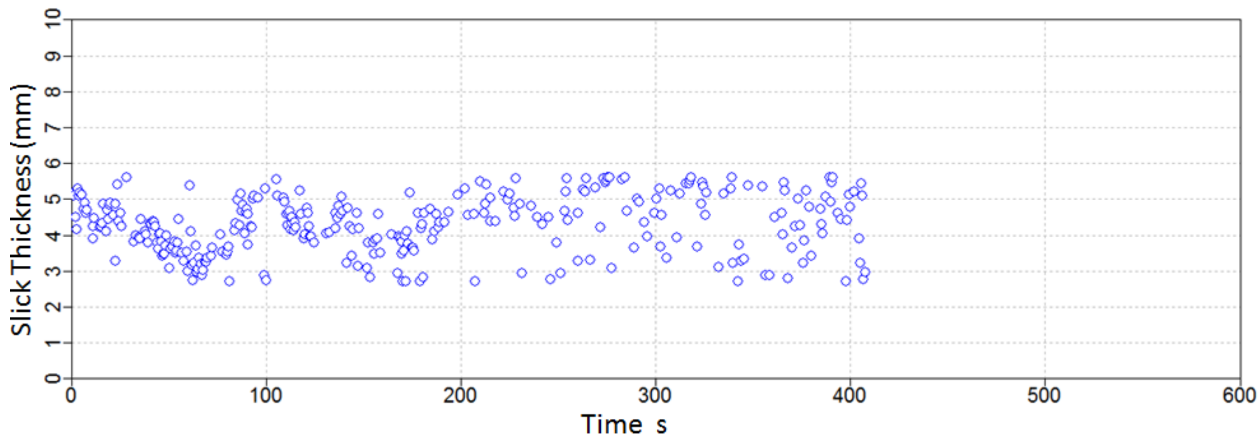

Figure 26. The measured oil slick thickness for the Test 18 where the waves where as high as 11 inches.

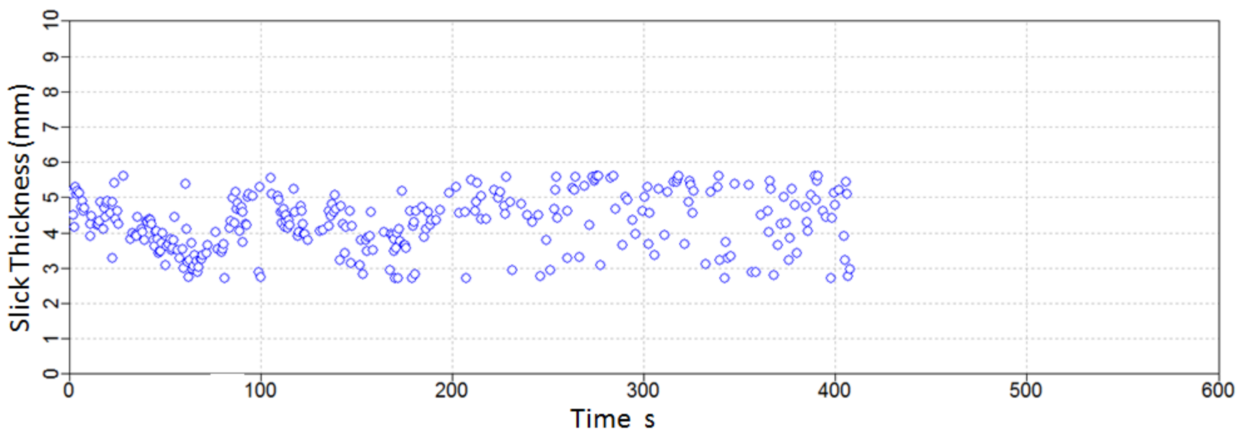

Figure 27. The measured oil slick thickness for the Test 16 where the wave as high as 22 inches.

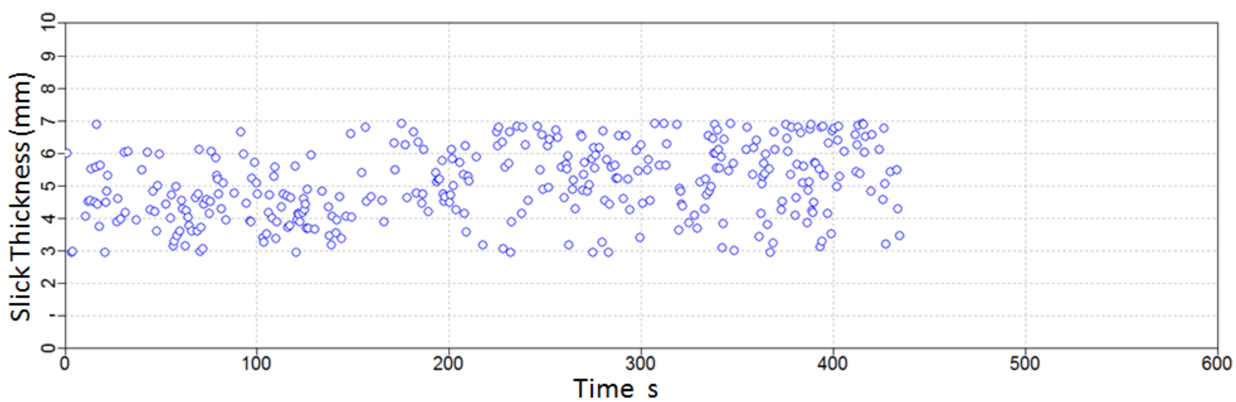

Figure 28. The measured oil slick thickness for the Test 17 where the waves where as high as 23 inches.

2.6. GLIDER MEASUREMENT OF SLICK THICKNESS

2.6.1. Glider Acoustic Sensor Mount setup and deployment

The glider was prepared by Professor Donglai Gong and Lauren Ferris from VIMS for oil slick thickness measurements. The glider was ballasted for coastal seawater densities of 1020 kg/m^3 to 1026 kg/m^3. During an open water deployment, the glider would operate untethered at water depths from the surface down to 30 to 1000 meters. The maximum depth for each vehicle depends on the vehicle's buoyancy pump configuration. The glider has a buoyancy pump that can move roughly 460 cc of seawater into and out of the glider's forward wet section. The glider can also move its forward battery fore and aft by roughly 1-2 inches. Both the buoyancy pump and the battery can be used to control the glider's pitch. For directional control, the glider has a rudder in the tail section. Under normal flight conditions, the glider would glide with a pitch angle of 26 degrees and a forward speed of 25-35 cm/s. The gliders inflect near the surface at an average depth of 3-5 meters.

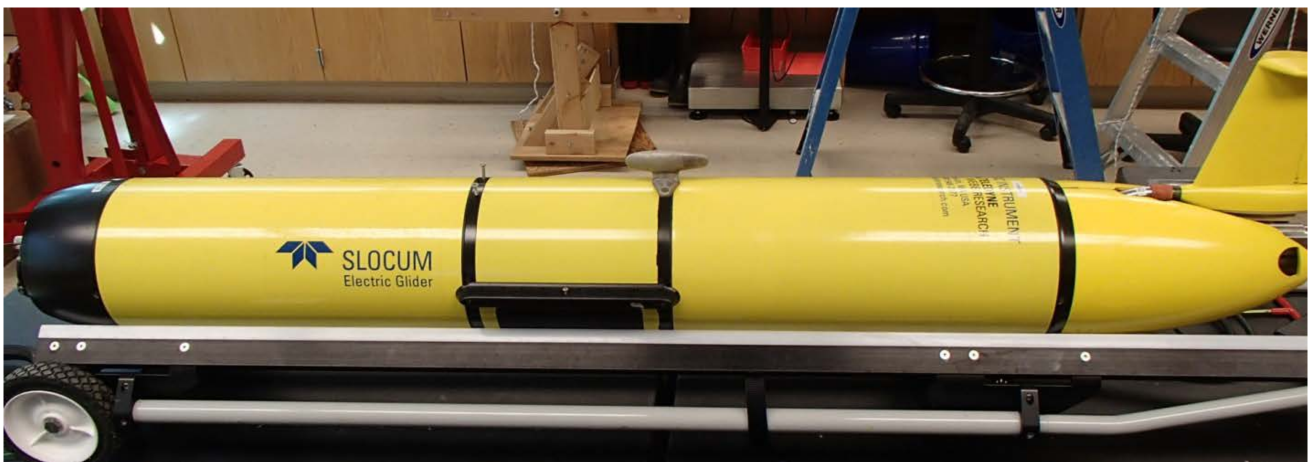

Figure 29: ARA's VIMS partners prepared this Slocum Glider for testing acoustic transducers at Ohmsett during February 2017.

The acoustic sensors were mounted onto the glider at two pitch angles (-26°, +26°) as shown in Figure 30; the angles were chosen to study the effects of the glider inflection motion near the surface on the acoustic measurements of surface slick thickness. The sensor mount was custom designed at VIMS and was rapid-prototyped using one of ARA's 3D printers from our Littleton, CO office. The acoustic transducers were powered and controlled from the surface for this study using the same acoustic equipment used on the ROV. The Raspberry Pi inertial motion sensors were also installed on the glider and ROV to record the pitch, roll, and yaw of the glider as shown in Figure 31. The results from this motion sensor are described in the appendix.

Figure 30. The acoustic transducers were mounted on the glider at +/- 26 degrees from vertical to match the dive and surface angles during the glider flight path.

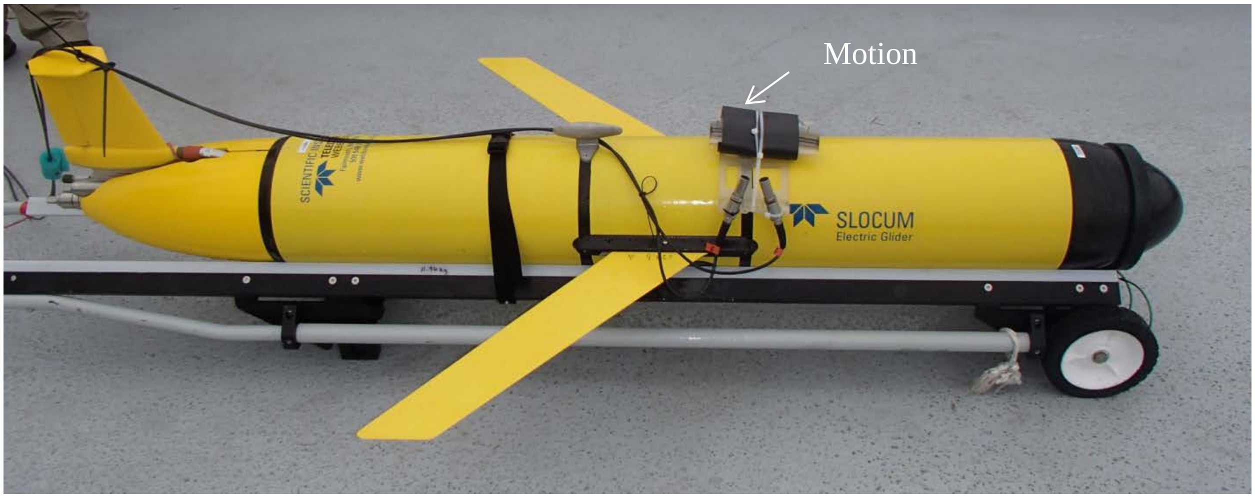

Figure 31. Inertial motion sensors and transducers were mounted on the glider to obtain slick thickness measurements for measured glider orientations.

The glider was deployed and manually placed in the boomed area before being moved underneath the oil slicks as shown in Figure 32 and Figure 33. The glider was near perfectly ballasted for the experiment which allowed the team the maximum flexibility in maneuvering the platform. The glider was programed to automatically maneuver the tilt and depth of the glider for series of yos to enable slick thickness measurements as shown in Figure 34.

Figure 32. The glider was deployed into the tank from the side using deployment techniques similar to techniques used in the open water.

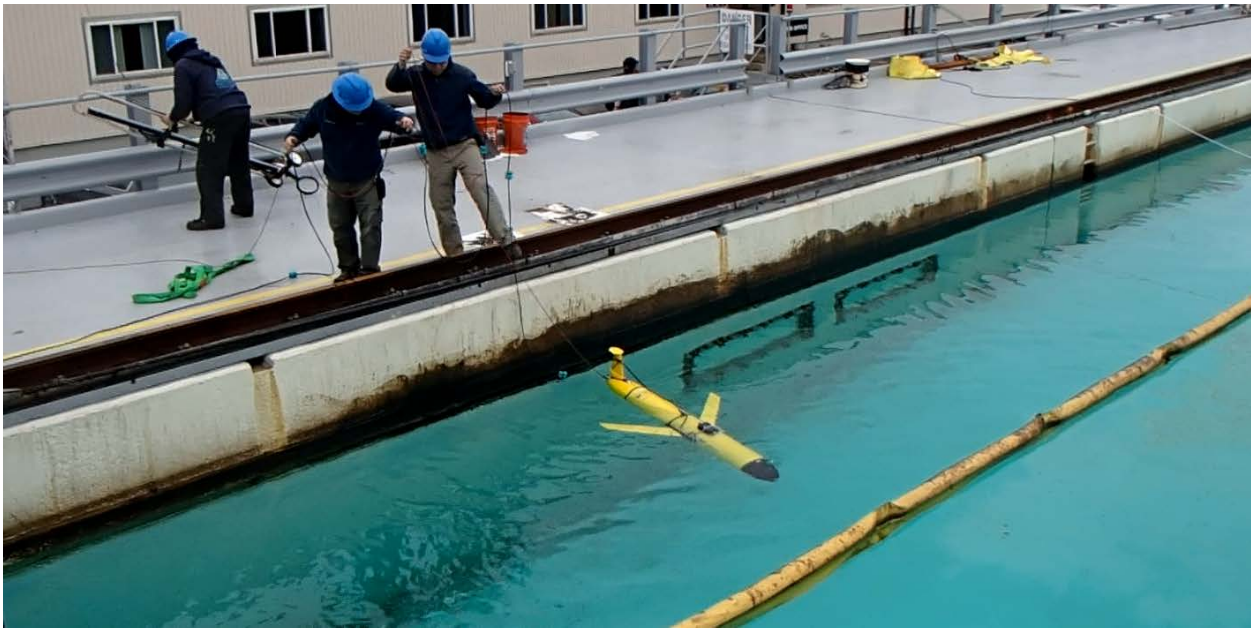

Figure 33. Additional adjustments were made to the glider's tethering and operational profile before flying under the oil slick.

Figure 34. The glider was programmed to perform a standard yo profile (+/- 26 degrees) spanning the 8 foot depth of the water column.

2.6.2. Slick thickness results from glider platform

The thickness of oil slicks was measured from the glider in sea states ranging from no waves to small amplitude long wavelength waves as shown in Table 2. Figure 35 shows results for the acoustic transducer at tilted 26° towards the front of the glider. The top pane shows the time of the acoustic arrival with respect to measurement time. The bottom pane shows the acoustic arrival at the cursor location shown in the top pane. The acoustic arrival shows multiple reflections: (1) the reflection from bottom of the slick arriving first, (2) the reflection from the top of the slick arriving second, and (3) a reverberation inside the slick arriving third. The two regions labeled “Gate 2” and “Gate 3” show the bottom of the slick and the reverberation. The time differences between the reflection from the top and the bottom of the slick and the time difference between the reflection from the top of the slick and reverberation were obtained for each A-scan. The oil slick thickness was calculated by multiplying the wave speed of sound in the oil by the measured one way acoustic travel time. Figure 36 and Figure 37 show thickness of the ANS oil slick measured from the glider platform without waves over two different time periods as it ascended and descended through the water column.

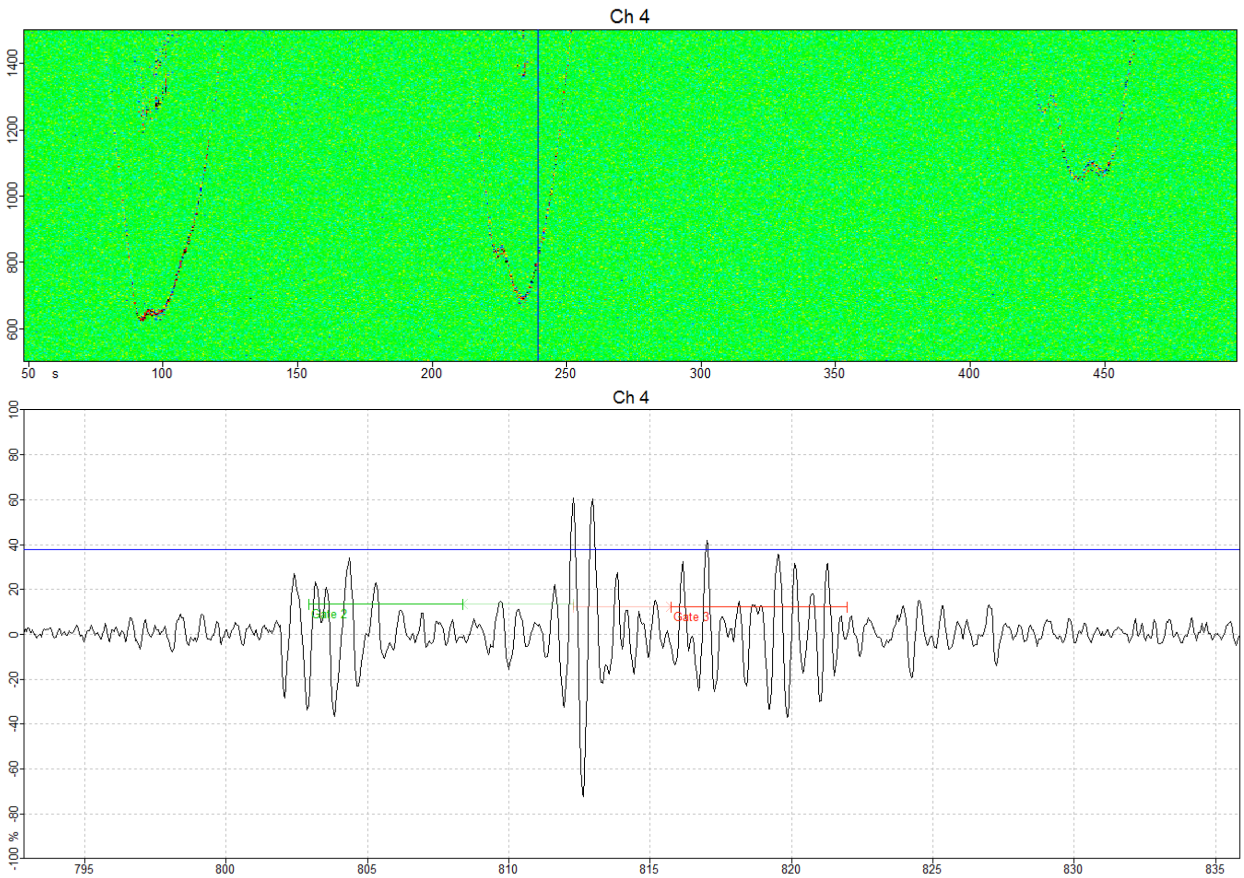

Figure 35. The acoustic return versus time (top) and the single acoustic return at the vertical cursor (bottom) as measured from the transducer at 26° angled towards toward the front of the glider was measured without waves during Run 1 without waves.

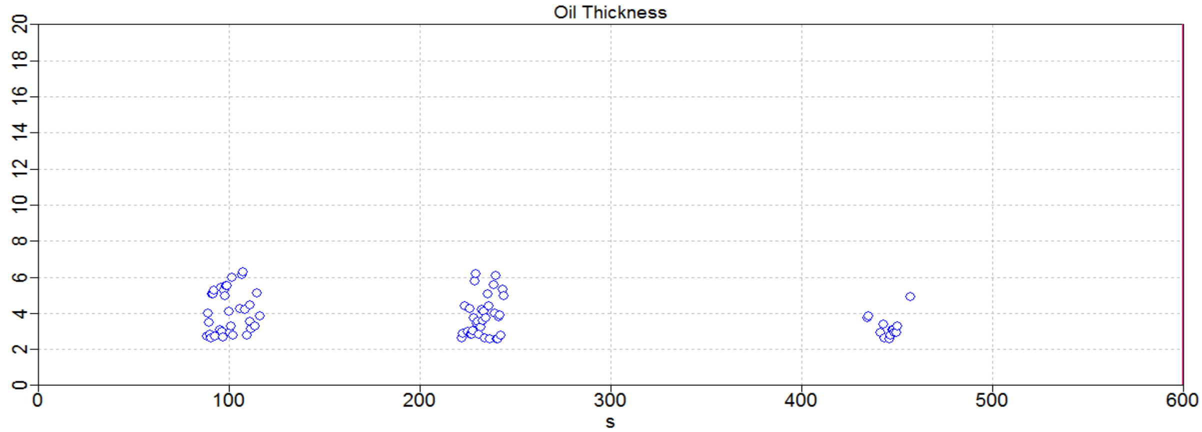

Figure 36. The oil slick thickness in the absence of waves measured by the transducer angled 26° toward the front of the glider was approximately 4 mm during Run 1 without waves.

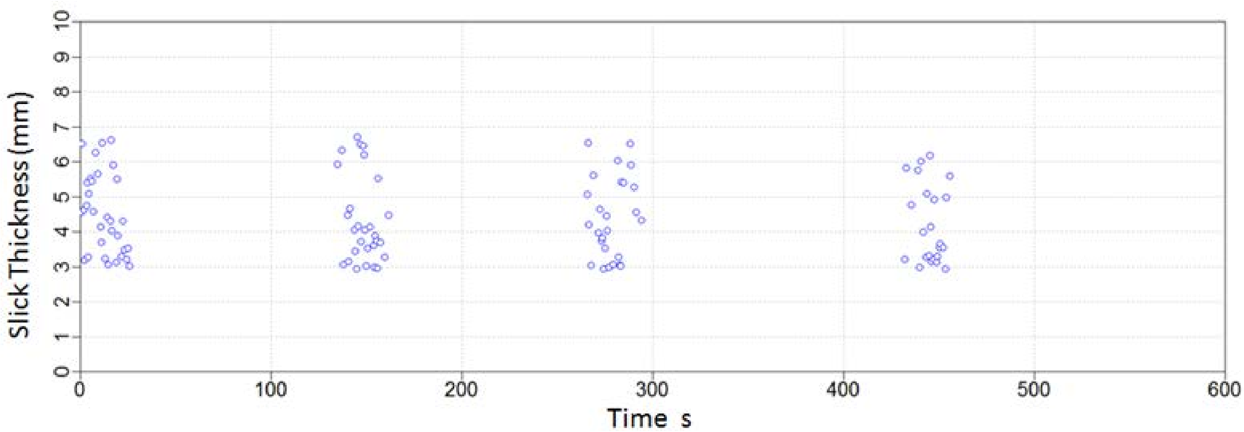

Figure 37. The oil slick thickness in the absence of waves measured by the transducer angled 26° toward the front of the glider was approximately 4 mm during Run 2 without waves.

The oil slick thickness was also measured from the glider platform when the sine waves were produced during Test 29 and Test 30. Figure 38 shows the acoustic arrival versus time and a single acoustic signal measured by the transducer angled 26° toward the front of the glider. Thus the data was collected while the glider was pointed up moving vertically through the water column towards the surface. Figure 39 shows the calculated thickness of the oil slick measured from the transducer angled 26° toward the front of the glider during Tests 29 and 30 where the height of the waves was at most 3.3 inches (Sea State 1).

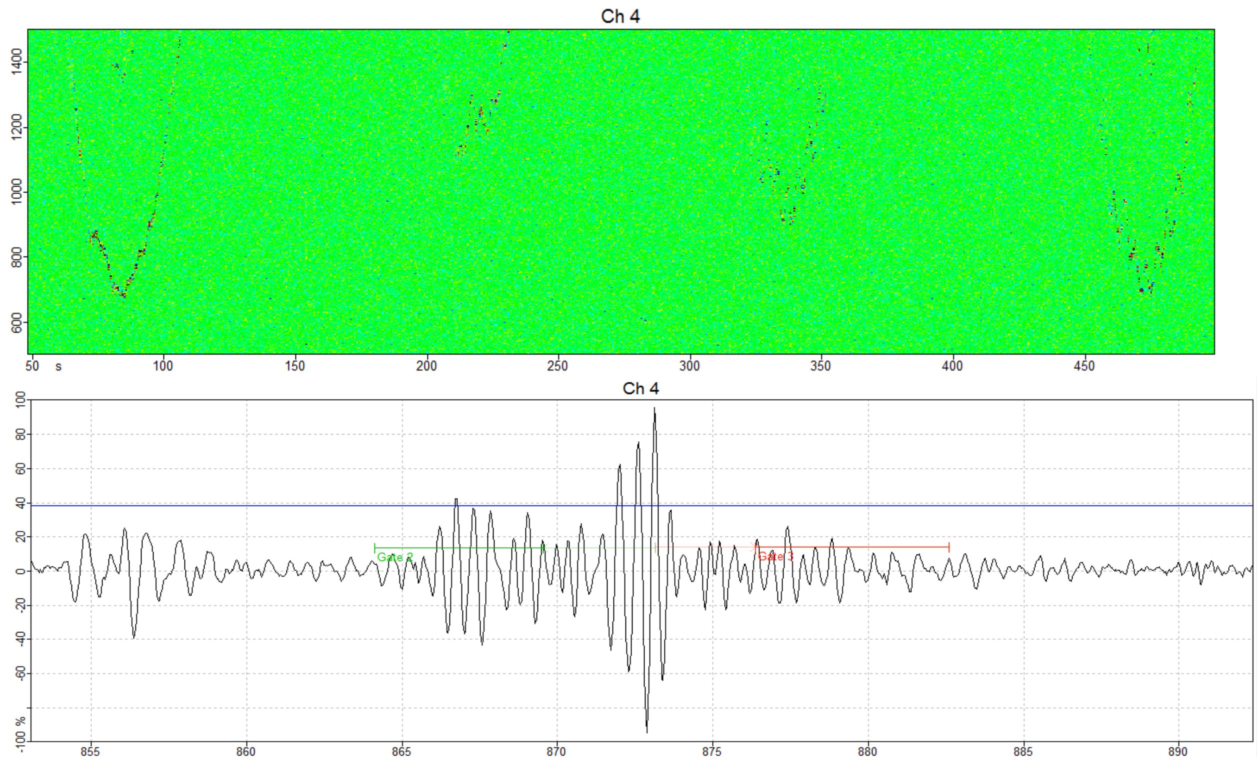

Figure 38. The acoustic return versus time (top) and the single acoustic return at the vertical cursor (bottom) as measured from the transducer at 26° toward the front of the glider (Run 3).

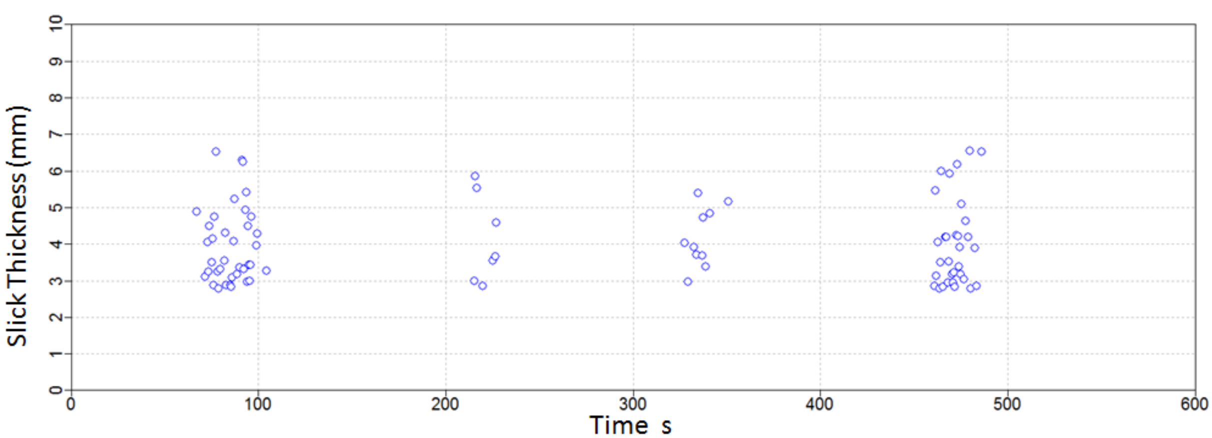

Figure 39. The oil slick thickness in the absence of waves measured by the transducer angled at 26° toward the front of the glider was approximately 3.5 mm (Run 3)

3. ACOUSTIC MEASUREMENT OF SUBSURFACE RELEASES OF OIL AND GAS FROM AN ROV PLATFORM

Measurements of the gas bubble size distribution and the scattering from the oil droplets were performed from the ROV platform. The gas bubble size distribution was measured with low frequency acoustic waves using a transducer that was mounted to a custom-designed rapid-prototyped bracket as shown in Figure 40. The transducer was bolted into the bracket and the bracket subsequently attached to the frame of the ROV using cable ties. The scattering from the oil droplets were measured using high frequency acoustic waves above 2 MHz using two ultrasonic transducers mounted to the underside of the bracket.

Figure 40. The large low frequency AirMar transducer was mounted on the ROV and floatation was added to ensure the ROV was neutrally buoyant. The high frequency acoustic measurements were performed using the two transducers mounted beneath the large AirMar low frequency transducer.

Once the transducers were mounted, the ROV was lowered into the water from the side of the tank at Ohmsett. Careful ballasting of the ROV with the large transducer attached was performed to ensure both the ROV and trailing cable were neutrally buoyant to ensure maneuvering was possible. Once buoyancy was achieved, the free-floating ROV was maneuvered to face the target bubble column and was held at station keeping while each dataset was collected (Figure 41). During tests where oil was present, the ROV maintained a distance of approximately 1 to 2 meters from the releases as shown in Figure 42.

Figure 41. The ROV was deployed in the tank by carefully lowering over the side (Left) before maneuvering near the bubble generator (Right).

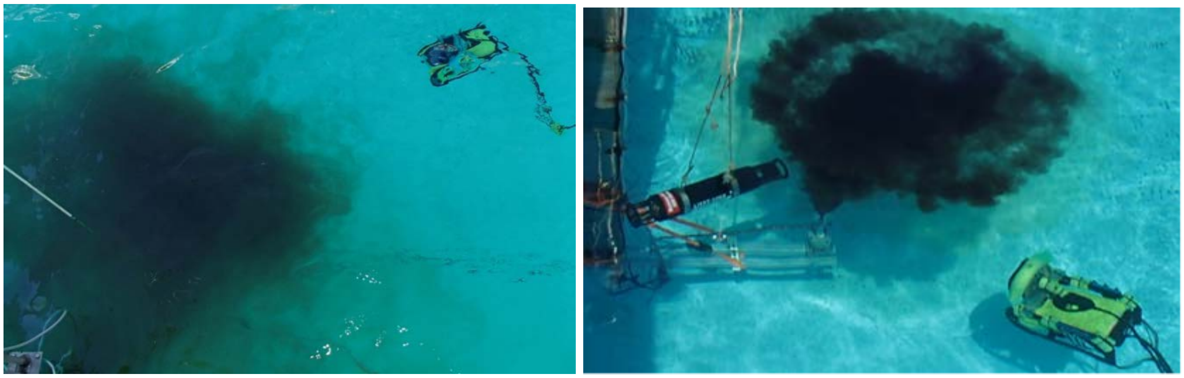

Figure 42. Left – The top view of ROV measuring the scattering from the air bubble and dispersed oil with the low and high frequency transducers. Right – The top view of the ROV with the low and high frequency transducers measuring the scattering from the crude oil droplets and air bubble.

We performed measurements multiple subsurface releases of methane, ANS and methane, and dispersed ANS and methane using Corexit 9500 at a dispersant to oil ration (DOR) of 1:20 as shown in Figure 43.

Figure 43. ROV performing measurements in three scenarios, methane (top), ANS and methane (middle), and dispersed ANS and Methane (bottom).

In the remainder of this section we will describe the measurements of the gas bubble size distribution followed by the oil droplet measurements.

3.1. ACOUSTIC MEASUREMENT OF GAS BUBBLE SIZE DISTRIBUTION

In this program, measurements of the bubble size distribution of a bubble plume during a subsurface release of oil and gas were performed. Acoustic transducers were mounted to an ROV which aimed them at a bubble plume with and without oil droplets present; the measurement paradigm is shown in Figure 44. A single acoustic pulse is transmitted toward the bubble cloud and the reflected signal is received by the same transducer. Based on the known properties of the water, distance to target, and transducer properties, the bubble size distribution can be inferred from the received signal. In this section, the experimental, theoretical, and data processing development necessary to capture this bubble size distribution is presented.

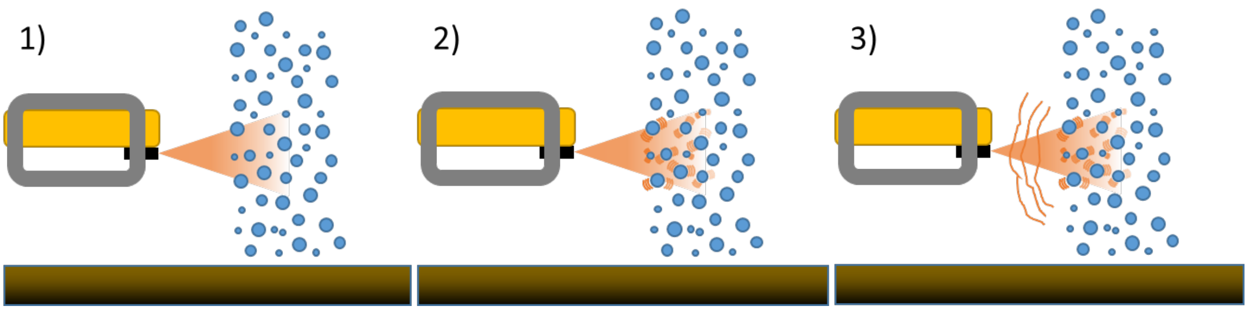

Figure 44. Measurement processes for acoustic scattering from a bubble cloud. A single transducer transmits (1), bubbles scatter sound in all directions (2), and the backscattered signal is received using the same transducer (3).

3.1.1. Measurement Apparatus

3.1.1.1. Bubble Generation

Bubbles for this program were generated using bubblers developed and proven on previous research and development programs. The bubbler consisted of a porous ceramic disc sealed into a cylindrical aluminum plenum, as shown in Figure 45. Each porous disc is designed to be used with a given pressure differential; in these experiments a 2 Bar disc was used for air bubbles and a 1 Bar disc was used for methane measurements.

The bubbler was installed at the base of the wing onto which the oil release nozzle was mounted. The bubbler was placed below the oil nozzle to allow gas bubbles to mix with any released oil without fouling the bubbler and rendering it inoperable. A single gas supply line was attached to a quick-disconnect fitting at the base of the manifold and extended to the surface where it was attached to a gas source, in this case a gas bottle for laboratory grade methane or a compressor for air.

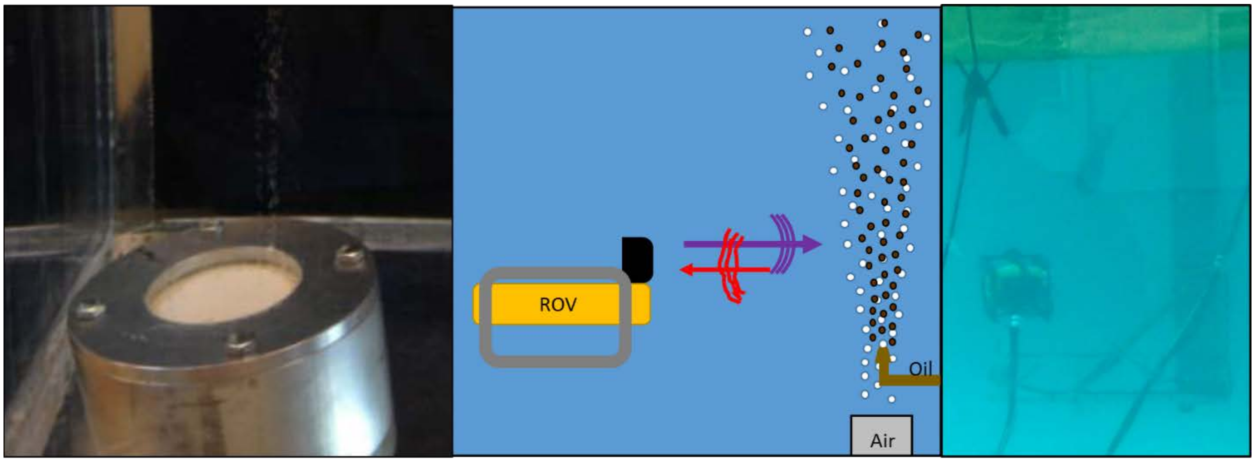

Figure 45. Left – A bubbler forced gas through a porous ceramic disc. Center – The transducer mounted to the ROV was aimed at the bubble and oil cloud created by the bubbler and oil release nozzle. Right – The ROV in Situ aimed at a bubble cloud.

3.1.1.2. Acoustics

The acoustic system used for the measurement of the bubble cloud size distribution is shown in Figure 46. A computer triggered a waveform generator which created a signal suited to the rest of the acoustic system, as described below. The signal passed through an amplifier to ensure the transmit signal strength was adequate for detecting the backscattered return. A diplexer was used to pass the high power transmit signal from the amplifier to the two-sided transducer and the low power received signal from the transducer to a filter/preamplifier. After passing through the filter/preamplifier, the signal was digitized by a data acquisition board for storage on the computer. The capabilities of this equipment is outlined in the following sections.

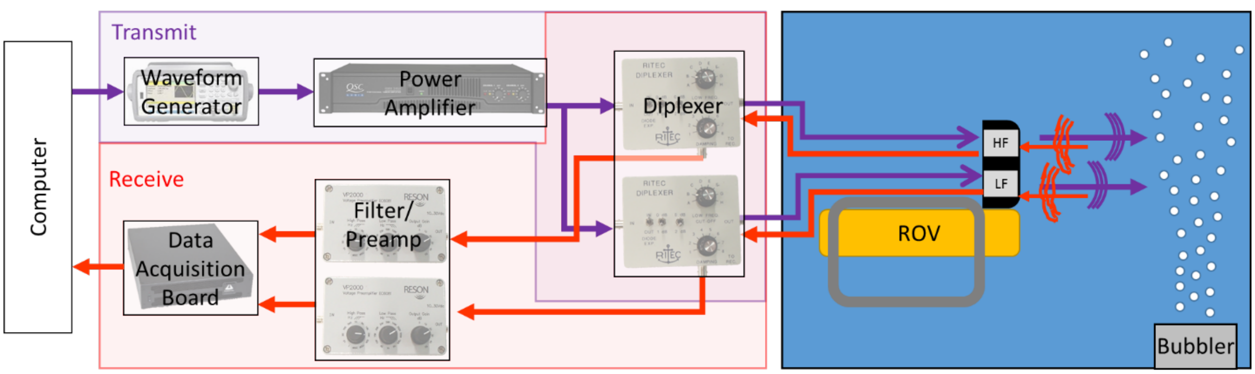

Figure 46. Setup for the acquisition of bubble cloud backscatter data. A computer-controlled arbitrary waveform generator creates a square wave impulse that is amplified, passed through a diplexer, and transmitted toward the bubble cloud. The received signal passes through the diplexer, is captured by a data acquisition board, and the waveforms are stored on the computer for further analysis.

Computer

The computer utilized for the effort was a laptop running a custom InspectionWare interface capable of controlling the function generator and data acquisition board through USB and ExpressCard connections, respectively. The use of the InspectionWare interface allowed for rapid changes to data collection routines and triage processing of datasets as they were collected to ensure high quality data was produced.

Function Generator

An Agilent arbitrary waveform generator was used to synthesize and generate the source signals for all tests. A single negative going square wave with an amplitude of 2 V and varying durations was used as a source signal. When measurements were performed using one side of the transducer to transmit and other to side to receive, the transmitted signals were tuned to the center frequency of the transmitting side of the transducer, either 50 or 110 kHz. When measurements were performed with both sides of the transducer transmitting simultaneously, a 50 kHz signal was generated.

Amplifier

The signal synthesized by the function generator was amplified by a QSC RMX 1450 two channel amplifier. The signal was passed through one channel of the amplifier to the transmitting side of the transducer. Typical gain values provided by the amplifier were approximately 26 dB which resulted in a 40 V signal directed toward the transducer.

Diplexer

A Ritec RDX-6-1K diplexer was used for each transmit channel to protect the receive electronics from the high voltage transmit signal. Damping was set to its minimum value of 10 Ohms to allow the broadband pulse to propagate through the system without being attenuated. The minimum low frequency cutoff of 1 kHz was also set to allow frequencies necessary for detection of larger bubbles to pass through the diplexer.

Transducer

An AirMar CM265LM transducer was used to project sound at and receive sound backscattered from the bubble cloud. For this device, the transducer housing has two independent transducers: one with an operational band of 42-65 kHz and the other with an operational band of 85-135 kHz. Each side is operated separately and is capable of transmitting and/or receiving the acoustic signal. For tests with air, one side of the transducer was used as a transmitter and the other as a receiver with each side used as both transmitter and receiver for different tests. For tests with methane, both sides of the transducer were excited simultaneously with each side of the transducer alternately recording.

Preamplifier

Each signal received from the diplexer was passed through a Teledyne Reson VP2000 voltage preamplifier powered by a Teledyne Reson EC6069 battery module. A 1 kHz to 250 kHz hardware band pass filter was applied to the signal to remove radiofrequency interference and maintaining the lowest frequencies of interest. Gain was also applied to each signal with 20 dB of gain for the low frequency side of the transducer and 30 dB of gain for the high frequency side of the transducer to maximize the utilization of the dynamic range of the data acquisition system.

Data acquisition

An Acquisition Logic Data Acquisition Card [DAQ] housed in a Magma PCI expansion chassis for connection to the control computer. Five ms of data was digitized at a sampling rate of 2 MHz. For tests with air bubbles, the data was collected for one transmitter and receiver per dataset and for tests with methane bubbles the data was collected alternately between each transmitter at half second intervals. Once digitized, the data was stored for off-line analysis.

3.1.2. Analysis

3.1.2.1. Mathematical Derivation

Following the work from Freinert and Nützel, measurements of the bubble size distribution based on acoustic backscatter were derived from the sonar equation,

$$M_v = RL - SL + TL - 10\log V \quad ,$$

where M_v is the volume backscattering defined by

$$M_v = 10\log m_V \quad ,$$

TL is the transmission loss in seawater defined by

$$TL = 2\left(20\log r + \frac{\alpha r}{1000}\right)$$

with α, the attenuation of sound in seawater, defined by Ainslie and McColm, *V* is the volume insonified by the acoustic beam, *RL* is the received pressure as a function of frequency from the receive transducer and *TL* is the transmitted pressure as a function of frequency from the transmit transducer. The backscattered signal per unit volume is defined as

$$m_v = \int_0^\infty n(a)\,\sigma_s(a)\,da$$

where *n(a)* is the bubble size distribution and $\sigma_S(a)$ is the scattering cross section for a bubble of radius *a*. The scattering cross section for a backscattering measurement is

$$\sigma_s = \frac{4\pi a^2}{\left[\left(\frac{f_0}{f}\right)^2 - 1\right]^2 + (ka)^2}$$

where f_o is the resonance frequency of a bubble of radius *a* defined by Commander and Prosperetti *k* is the wavenumber in water, and *f* is the insonification frequency.

The equation can be reformulated to

$$m_V = \int_0^\infty n(a)\,\sigma_s(a)\,da = 10^{(RL-SL+TL-10\log V)/10}$$

which can be used to extract the bubble size distribution term. Specifically, through a change of variables and using the approximation that the resonant bubbles will be the primary contributors to the backscattered signal as described in Section 8.3 of Medwin and Clay, the integral portion of the equation is reduced to

$$m_V = \frac{\pi a_0^3 n(a)}{2\delta_0}$$

where a_0 is the resonant radius and δ_0 is the damping term for a bubble resonant at frequency f_0. The resonant radius is again determined by Medwin and Clay and the total damping term (sum of thermal, radiation, and viscous terms) is defined in Chapter 3 of Leighton. This approximation introduces an error of a few percent but is adequate for estimating the bubble size distribution. Therefore, the final equation used in the analysis is

$$n(a) = \frac{2\delta_0}{\pi a_0^3}\,10^{(RL-SL+TL-10\log V)/10}.$$

When performing the measurements each of these terms, with the exception of the bubble size distribution is known.

3.1.2.2. Data Processing

Determining the bubble size distribution from the backscattered acoustic energy follows the following steps according to the analytical development above:

1. Record raw data
2. Subtract the mean signal from each signal
3. Perform a Fast Fourier Transform (FFT) on each signal
4. Adjust each signal for gain and transducer sensitivity (SL and RL terms)
5. Calculate the transmission loss for seawater (TL term)
6. Derive the volume scattering term (V term)
7. Derive the bubble size distribution

The signal processing steps will be outlined using the analysis for one dataset for a methane bubble plume in the following sections.

Record

Figure 47 shows ten recordings of the acoustic backscatter measurement on a methane bubble plume. At the beginning of each signal, the recorded signal is clipped due to high amplitude acoustic cross-talk between the two sections of the transducer. The bubble signal is clearly visible as the time variable portion of the recordings whereas the crosstalk is the time invariant portion of the recordings.

Such recordings are collected at a rate of one per second per transducer and form a B-Scan which demonstrates the development of the bubble cloud with respect to time. Figure 48 shows a B-Scan for the bubble only case, bubbles plus ANS, and bubbles plus dispersed ANS. Each individual backscatter result is shown as a vertical line in the B-Scan with the evolution in time shown as the horizontal axis. Variation from green denotes oscillation about zero pressure. Each of these B-Scan images has approximately the same amount of color variation which demonstrates that this measurement is robust against the introduction of oil droplets.

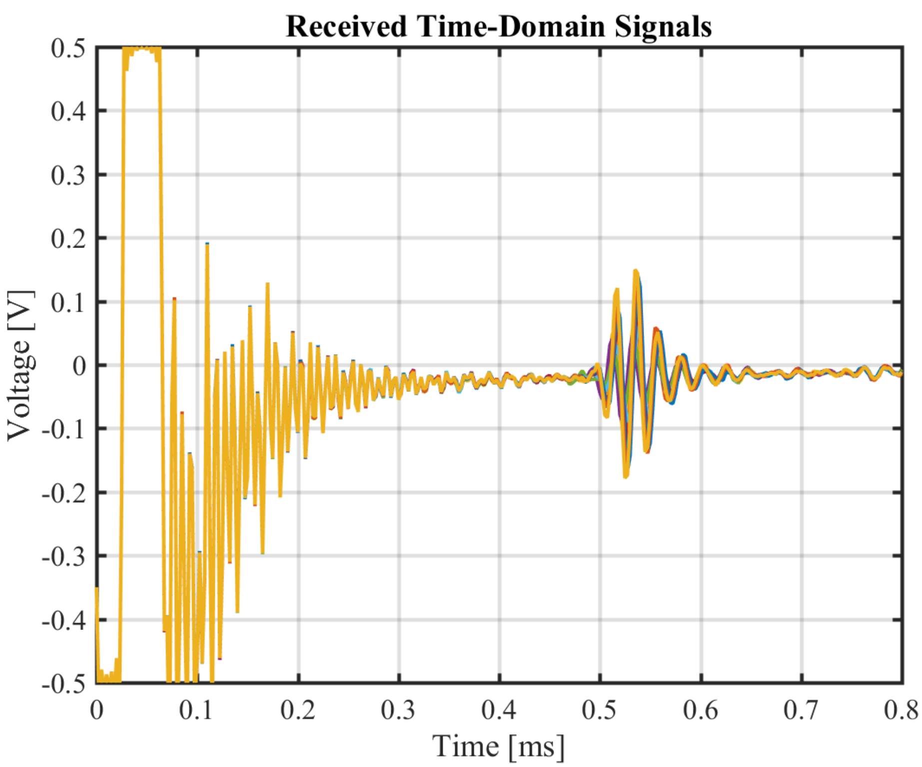

Figure 47. Ten different acoustic backscatter signals from a methane bubble plume.

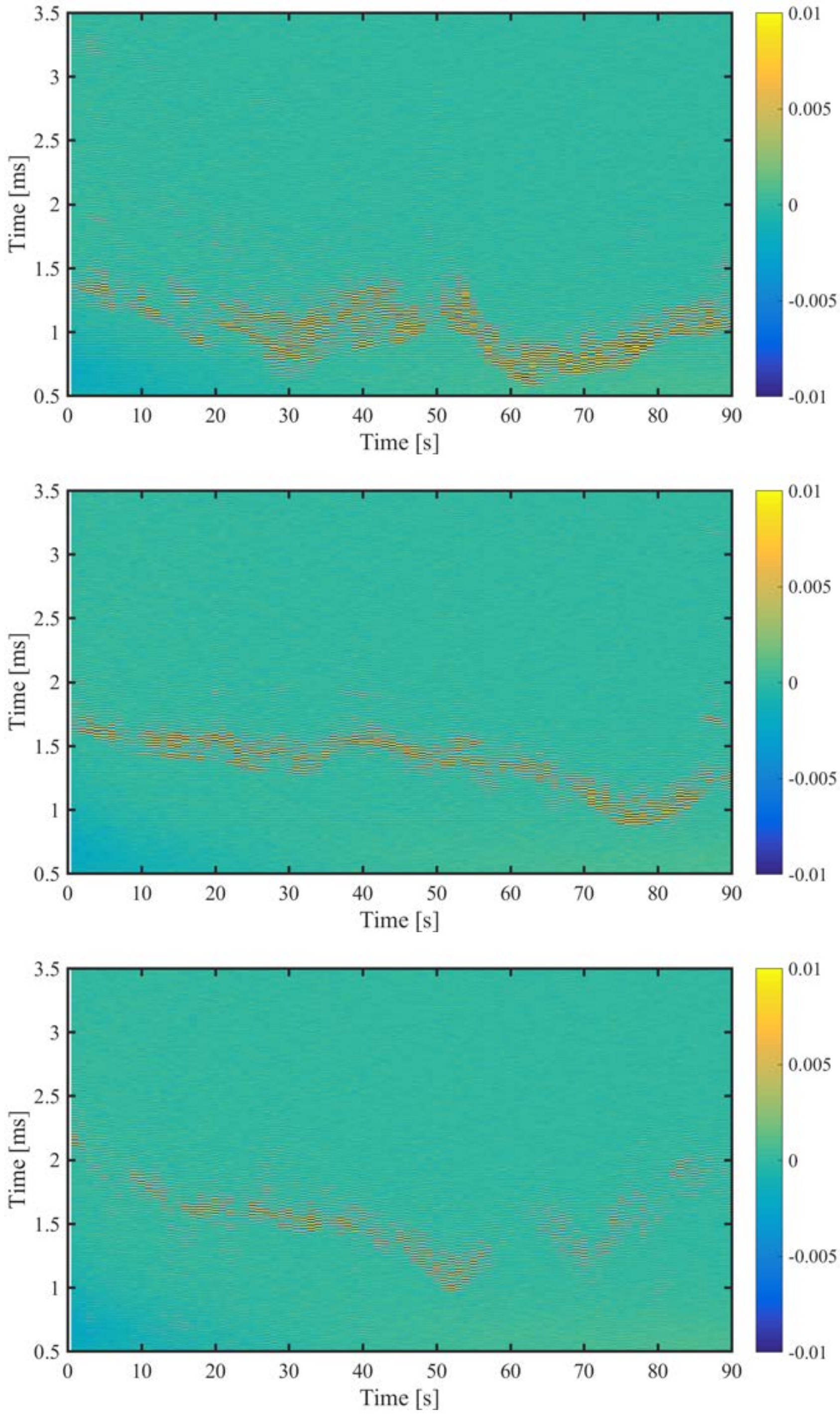

Figure 48: B-Scans for Methane, Test 39 (top); Methane and ANS, Test 47 (middle); and Methane and dispersed ANS, Test 53 (bottom).

Subtract

The mean signal from all of the recorded signals is found, as shown in Figure 49 - Left. This signal is a composite of the transducer response, acoustic crosstalk, and persistent reflections from non-bubble sources. The mean signal is subtracted from the rest of the signals to produce the approximate backscattered bubble signal, as shown in Figure 49 – Right for the same signals shown in Figure 47. Note that the signal with the mean removed has a much higher signal to noise ratio than the raw data, thereby improving the automated detection and analysis routine.

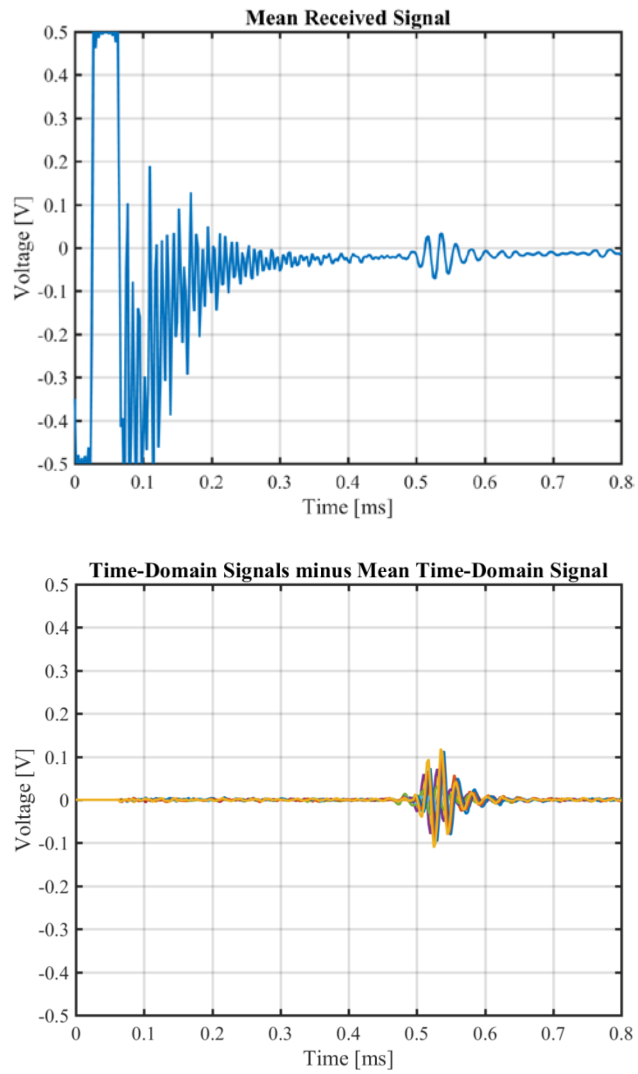

Figure 49: Top – The mean of 300 received signals used to represent the electrical and mechanical system response. Bottom – The same ten received signals from Figure 47 with the mean signal subtracted from each. These signals are taken to be the approximate backscatter response of the bubble column.

Fourier Transform

To ascertain the frequency response of the bubbles, a Fast Fourier Transform (FFT) is performed on each signal. The resultant spectrogram (frequency vs. time) is shown in Figure 50. The frequency content fluctuates as the bubble size distribution changes in time. The evolution with time is shown along the horizontal axis with the individual frequency content for each backscattered signal shown as a line along the vertical axis.

The brighter yellow the signal is, the more prevalent that frequency component is in the received signal.

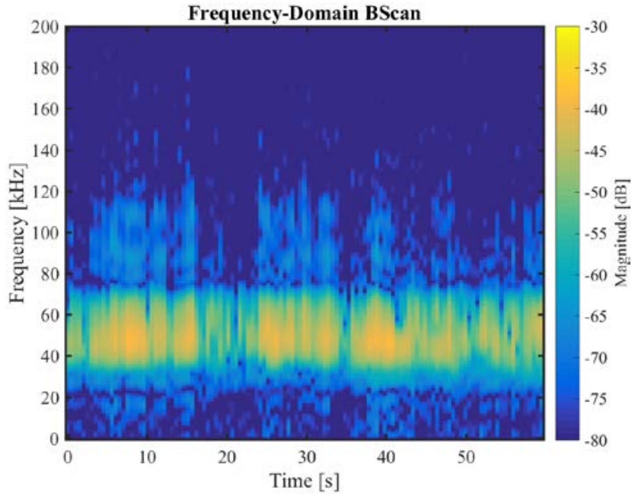

Figure 50. The frequency content of the backscattered signal is found.

Gain/Sensitivity Adjustment

Correction of the average receive signal through removal of the transducer sensitivity is shown in Figure 51. The mean receive signal is shown in blue and is the average of all backscattered returns. The transducer calibration is shown in orange and was determined by performing an FFT on a signal reflected from the near-perfectly reflecting air-water interface. By subtracting the calibration (orange) from the received signal (blue), the effect of the frequency-dependence of the transmit and receive sensitivities of the transducer is removed, resulting in the yellow frequency response. This response is then used to derive the bubble size distribution.

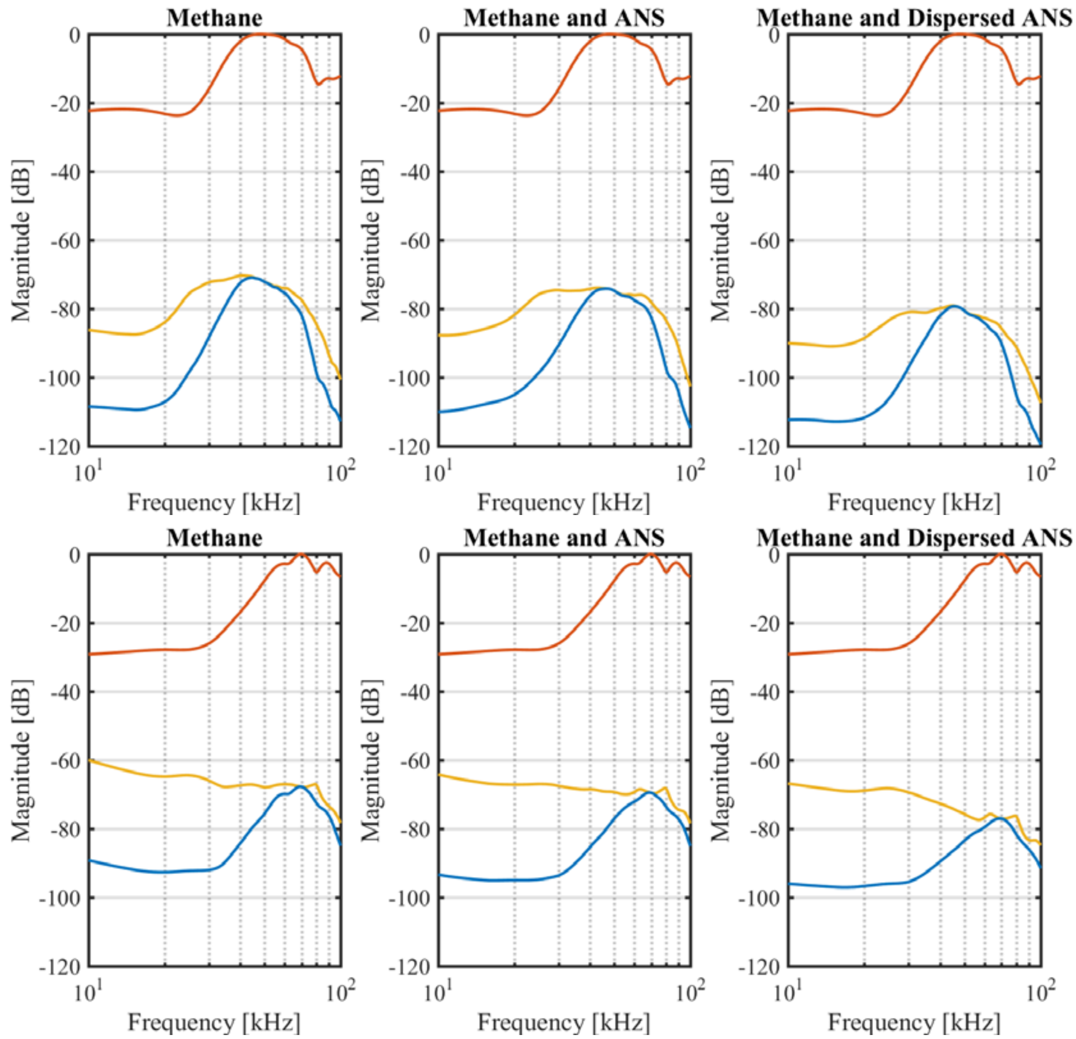

Figure 51: Correction of the received signals to remove the transducer sensitivity is performed in processing step 4. The low frequency (top) and high frequency (bottom) transducers have different sensitivity curves shown in orange which correct the received signal in blue to the actual backscatter amplitude in yellow.

Transmission Loss (TL)

The *TL* term was determined from the known properties of the water and the range to target as shown in Figure 52.

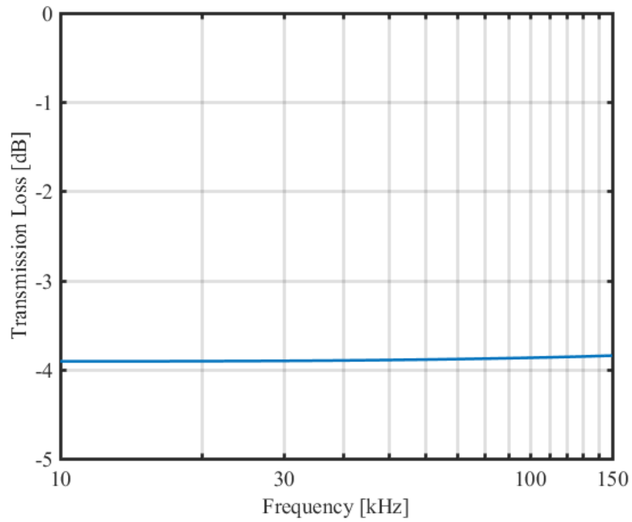

Figure 52. The transmission loss term in the sonar equation is dependent upon range and acoustic attenuation in seawater.

Volume Term

By calculating the frequency-dependent spot size, the fraction of that diameter and the height of the column insonified can be determined. The range to the target is calculated based on time of arrival of the reflected pulse. The duration of the reflected signal is then used to determine the overall two-way travel time through the cloud which results in the bubble plume diameter; in these tests, the plume was determined to be approximately 0.26 m in diameter at the height of the measurement. Based on the transducer specification, the beam width was interpolated for each frequency and the spot size was determined. Based on this spot size, the volume term can be calculated, as shown in Figure 53.

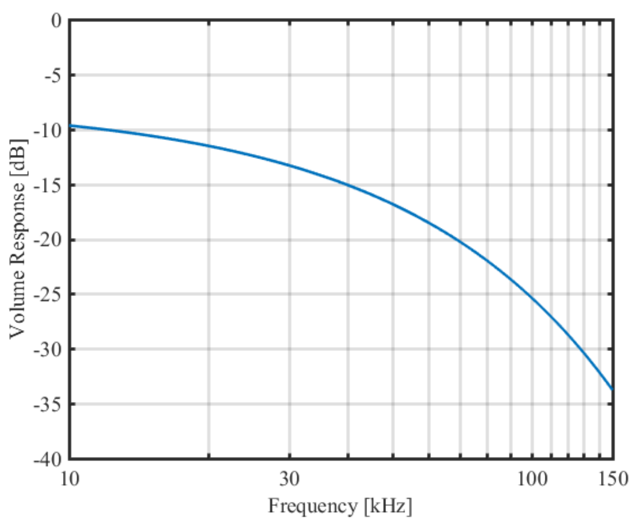

Figure 53. The volume term is calculated from the transducer spot size and the bubble cloud diameter.

3.1.3. Bubble Size Distribution

Table 3. Different parameters for bubble properties were used in the inversion of the backscatter measurements for air and methane.

Parameter Name	Air	Methane	Units
Density	1.21	0.716	kg/m^3
Ratio of Specific Heats	1.4	1.32	
Specific Heat at Constant Pressure	240.0	530.6	cal/kg-°C
Thermal Conductivity	5.6e-3	8.37e-3	cal/m-s
Thermal Diffusivity	1.9e-5	2.20e-5	m^2/s
Surface Tension	75e-3	6.42e-4	N/m

Using the gas parameters appropriate for the given test, bubble size distributions were obtained, as shown in Figure 54. The bubble size distribution for each dataset was averaged for both the low frequency transducer (Channel A, left) and high frequency transducer (Channel B, right). Each ROV flight generated a new test. Variations between tests are primarily governed by the ability of the ROV operator to aim the acoustic transducer at the center of the bubble cloud; during tests with ANS and dispersed ANS, visibility of the cloud was diminished, thereby making aiming more difficult and reducing the average backscattered acoustic return.

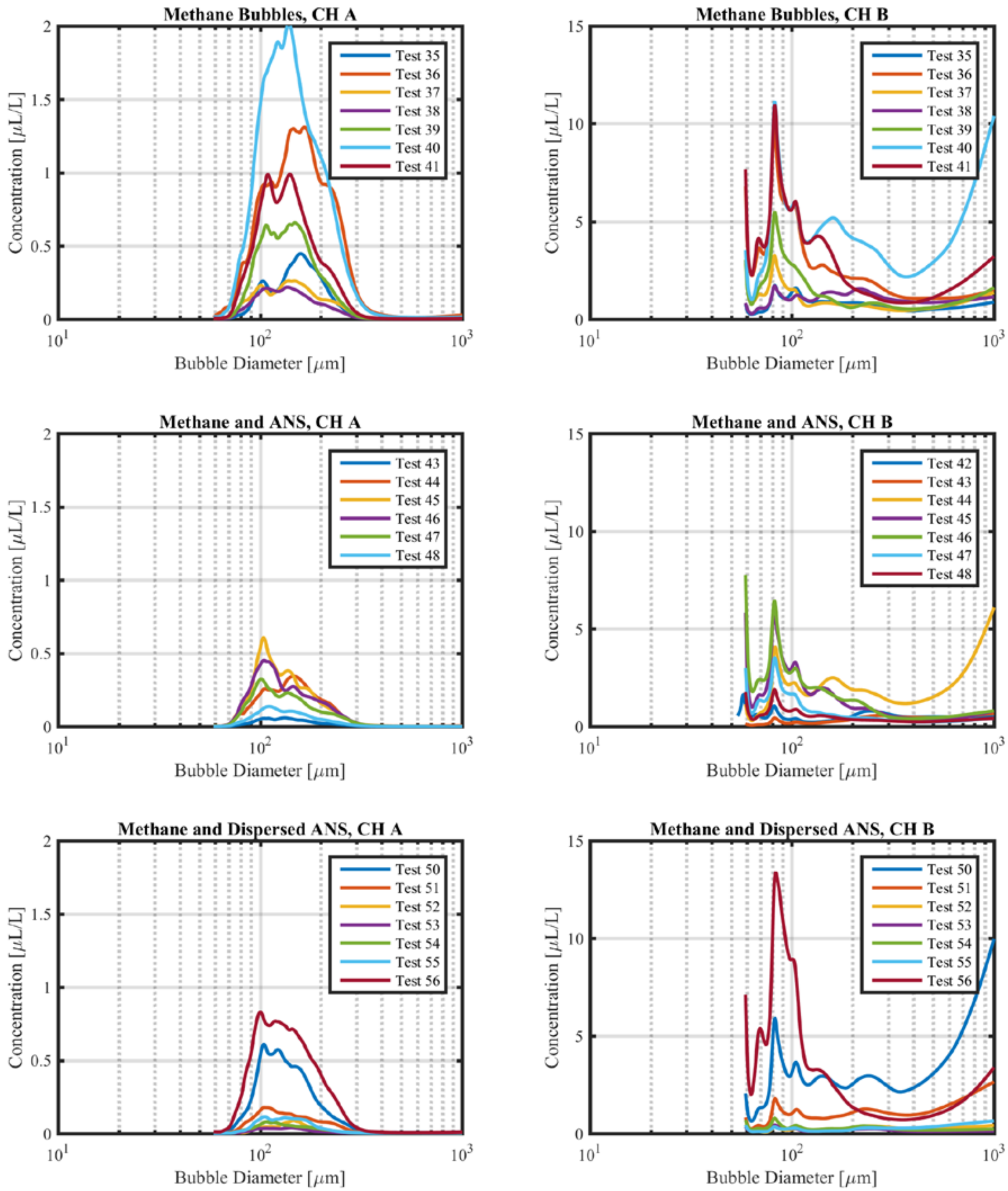

Figure 54. Results of the data processed for the subsurface gas releases at Ohmsett. Bubble size distributions from the low frequency (left) and high frequency (right) transducers were obtained for methane only (top), methane and ANS (middle), and methane and dispersed ANS (bottom) test cases.

For testing with air bubbles where one half of the transducer transmitted and the other received, the low and high frequency (large and small bubble diameter) measurements demonstrate different peak frequencies due to the resonance frequencies of the individual transmitters, as shown in Figure 55.

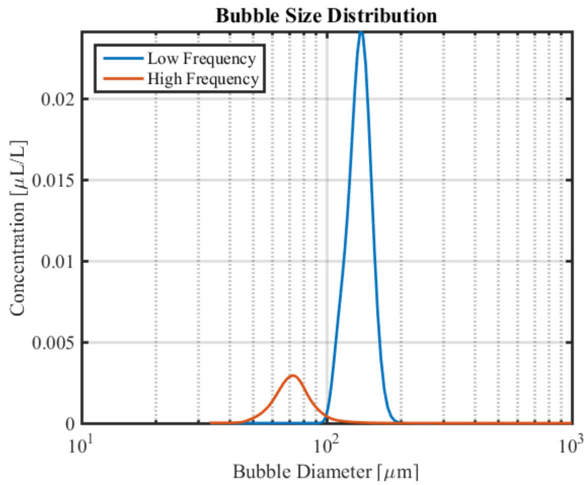

Figure 55. An example bubble size distribution calculations for air bubbles.

One benefit of using this measurement technique is the ability to observe the change in bubble population with respect to time. Figure 56 demonstrates the bubble size distribution evolution for both the high and low frequency transducers. It is noted that the size distribution is confined to the specific bands for each transmitter.

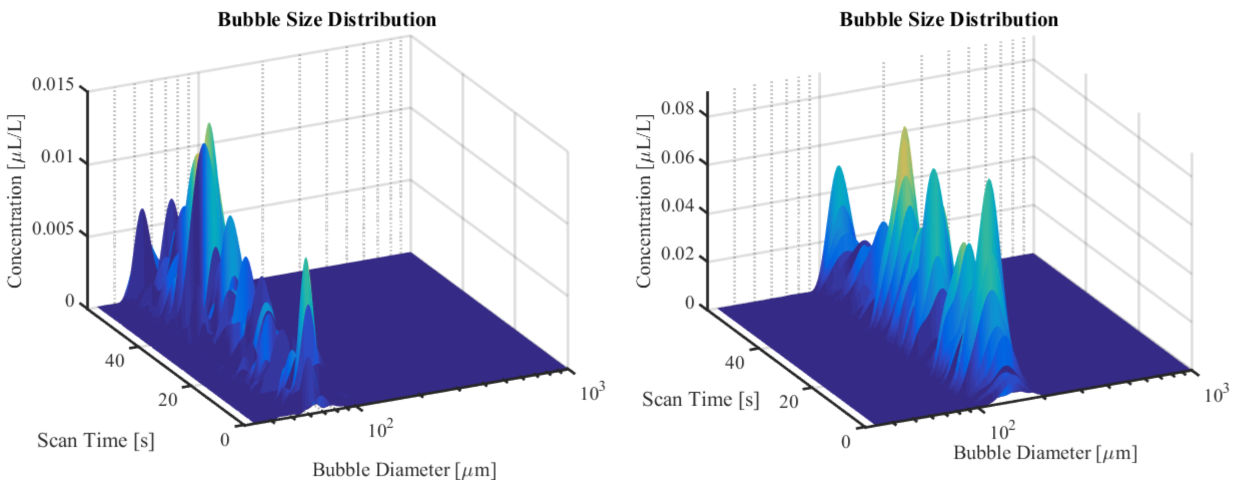

Figure 56. Bubble size distribution over time for the high frequency transmitter (Left) and low frequency transmitter (Right).

3.1.4. Comparison between static and free swimming platform

Data from the air and methane bubble-only tests are shown in Figure 57. In air bubble tests, the two halves of the transducer produced narrow bubble size distributions focused specifically on each transducer's operational band. In the methane measurements at Ohmsett, the signals are much more broadband. Therefore, for the bubble sizes generated by the bubblers used on this and other BSEE programs on which ARA performed, the low frequency transducer appears to be adequate to generate the bubble size distribution.

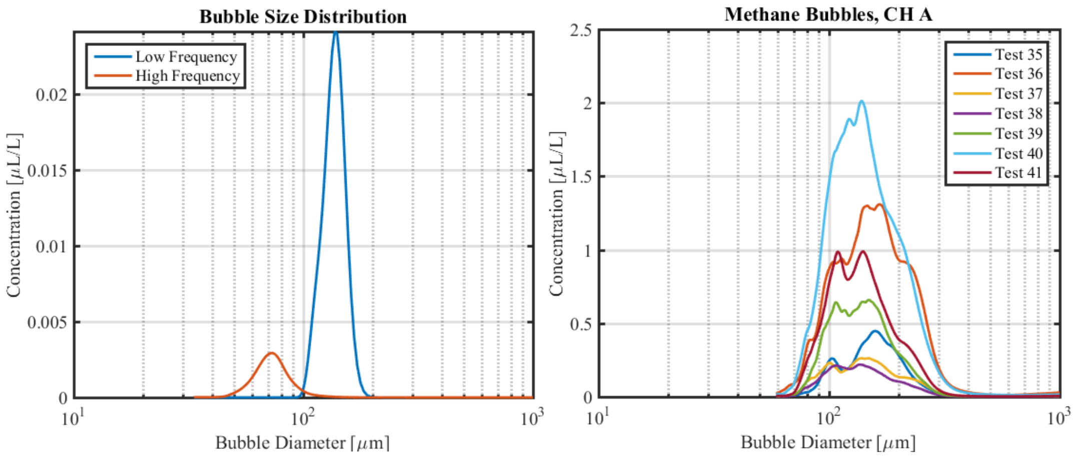

Figure 57. Bubble size distribution measurements were obtained using both the high and low frequency sides of the AirMar transducer with air at VIMS in November 2016 (left) and with just the low frequency side of the AirMar transducer with methane at Ohmsett in February 2017 (right).

In the final report for BSEE Project 1002, the right pane of Figure 67, reproduced here in Figure 58, shows the bubble size distribution for seven tests performed with air bubbles and dispersed oil using transducers mounted to a fixed frame. Figure 58 also shows the bubble size distribution for seven tests performed from a free-flying ROV during the current program. Less variation is shown in the maximum gas concentration for the fixed from the fixed frame (~5%) compared to the variation in the maximum gas concentration from the free-flying ROV (~70%) due to the nature of the motion of the ROV.

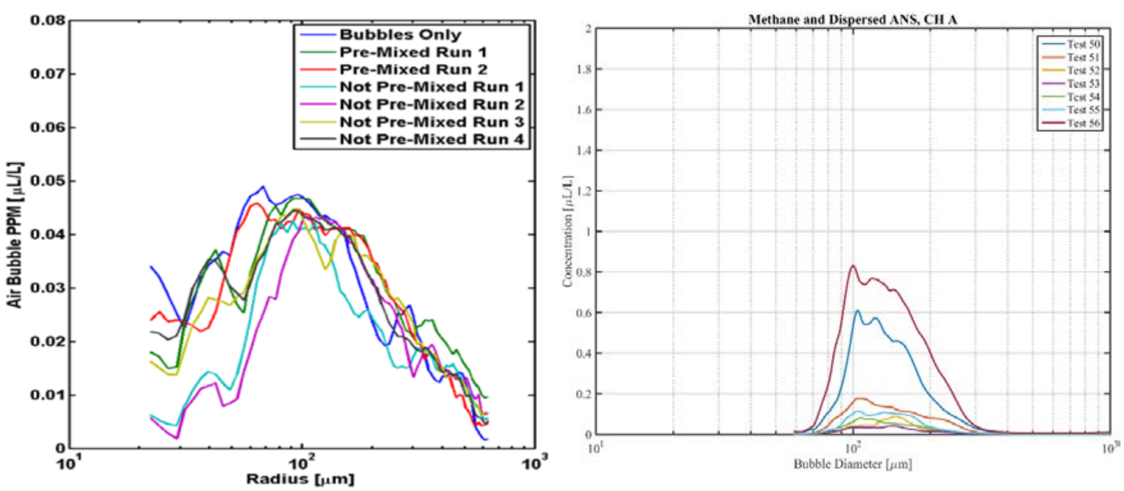

Figure 58. Bubble size distributions measured during BSEE Project 1002 (left) and during this project (right) for bubbles and dispersed oil. The variation in the gas concentration varies less for the measurements from the fixed from (left) than for the free-flying ROV (right).

One more point of comparison is use of a Laser In-Situ Scattering and Transmissometry (LISST) to obtain independent measurements of bubble size distribution. One such distribution, an average typical of an air bubble test, is shown in Figure 59. Both air and methane measurements, such as those shown in Figure 57, have mean bubble sizes near the LISST-measured mean bubble size and roll off toward larger and smaller bubble sizes at comparable rates.

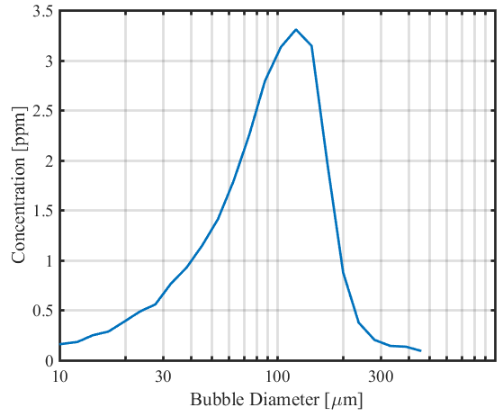

Figure 59. LISST measurements performed on the air bubbler produced a bubble size distribution consistent with both the air and methane bubble measurements.

3.2. Acoustic Measurement of Dispersant Effectiveness from ROV Platform

Acoustic scattering data from plumes of methane bubbles and oil were measured with the transducers mounted to the ROV. A "sonar-like" image of the scattering from a plume of dispersed ANS and methane is shown in Figure 60. The resultant average backscattering amplitude as a function of frequency for 3 methane releases, 6 ANS with methane releases, and 7 dispersed ANS with methane releases is shown in Figure 61.

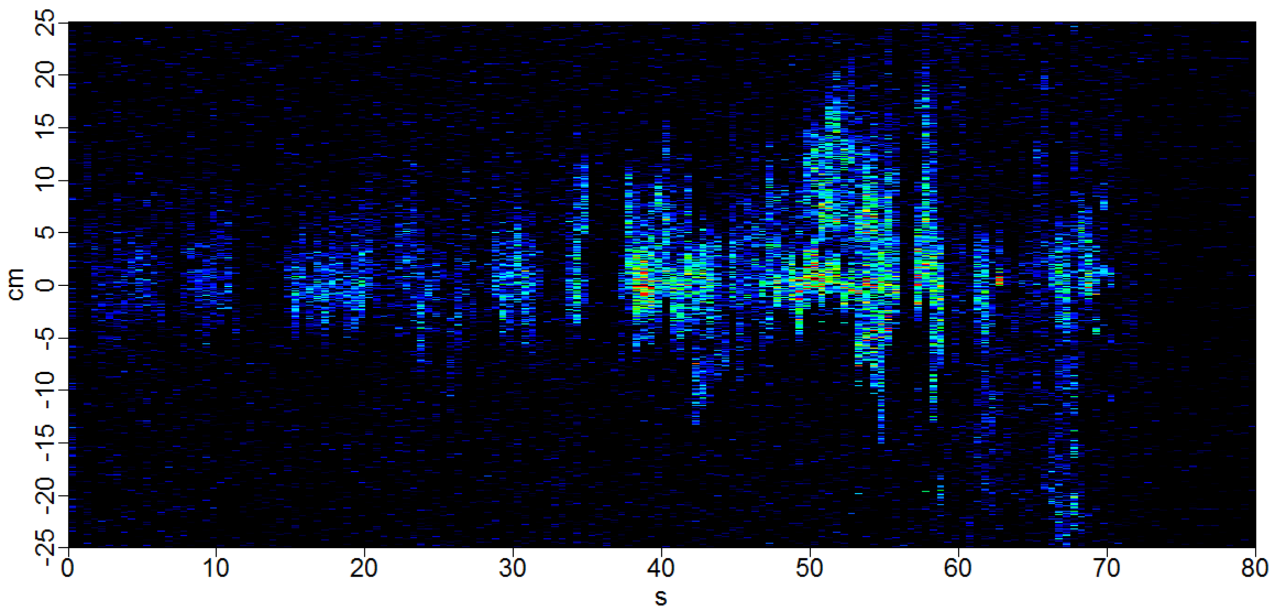

Figure 60. Acoustic sonar image from a plume of dispersed ANS and methane. The high scattering is red and low scattering is dark blue/black. Each vertical line is a single ping over the 80 second measurement time. The vertical axis is the distance from the center of the plume.

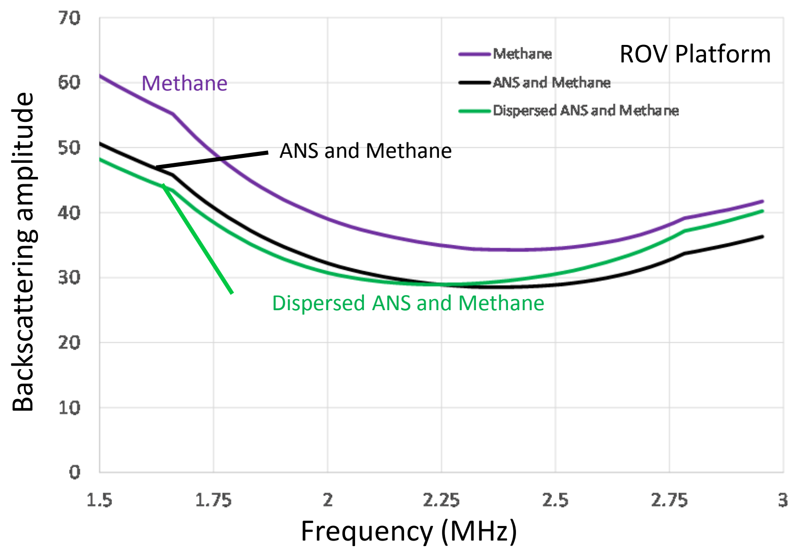

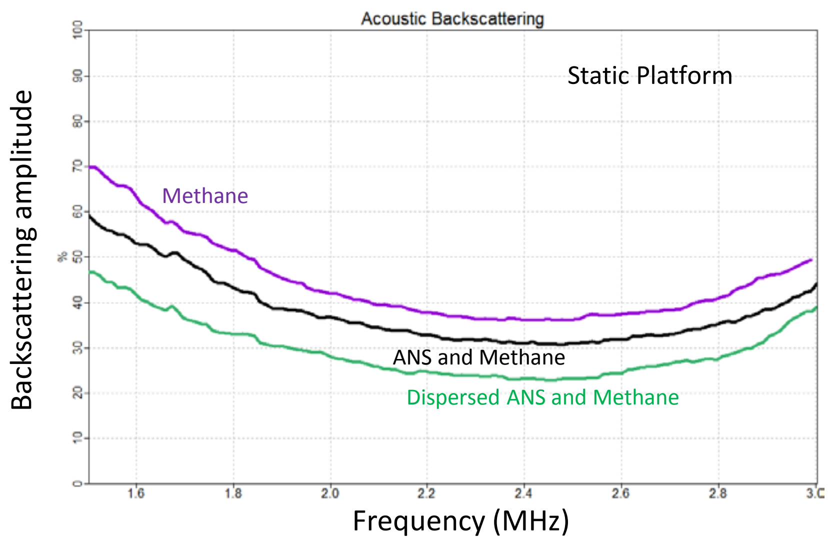

Figure 61. The backscattering amplitude as a function of frequency measured from the ROV platform (top) and static platform (bottom) for methane, ANS and methane, and dispersed ANS and methane.

The backscattering results from the free swimming ROV platforms are similar to measurements from static platforms with the methane showing the highest backscattering followed by ANS with methane, then dispersed ANS and methane for frequencies less than 2.25 MHz. Importantly, the dependence on frequency of the backscattering increased as oil was added to the methane, and the dependence on frequency increased even more when the oil was dispersed. This increased dependence on frequency observed as the oil became more dispersed is similar to measurements we performed from a static platform submersed under the water at Ohmsett [Panetta et al. 2014]. Coupled with our systematic measurements from static platforms, these measurements from the ROV show the feasibility of measuring dispersant effectiveness from ROV platforms.

4. DEPLOYMENT PLATFORMS FOR OIL SPILL RESPONSE

We explored only two options for deployment on free swimming ROV and glider platforms and were the first team to the author's knowledge to measure the slick thickness from ROV and glider platforms. To best transition these measurements to open water environments to characterize oil spills will require deployments on multiple platforms. The two main criteria that limit implementation on various platforms are power requirements and size. These restrictions are relaxed for ROV platforms since operations ROVs are large and carry power to the vehicle. More significant restrictions exist for AUV deployments because the payload space is small (typically 1 foot x 6 inch diameter) and the power requirements are stringent because the AUVs are battery operated.

5. SUMMARY AND CONCLUSIONS

In this project we have begun the transition of acoustic measurements of slick thickness, gas bubble size distribution, and oil dispersant effectiveness to free swimming ROV and glider platforms. Using a SeaBotix LBV150 ROV vehicle, we have demonstrated the ability to effectively measure both oil slick thickness as well as gas bubble/oil droplet size distribution while operating the ROV in free swimming mode in our labs and at Ohmsett. We also demonstrated the ability to measure the slick thickness using acoustic sensors mounted on a Slocum glider. The oil slick thickness measurements were performed both in the absence of waves as well as the presence of waves. Acoustic transducers were mounted externally on the frame of the ROV and the glider and tethered via cables to data collection and processing hardware.

While the extra sensors and cabling associated with oil slick thickness measurements do impact the performance and flight dynamics of the ROV, proper ballasting and mounting of the sensors allowed the vehicle to remain controllable and flyable. The existing setup could be deployable in an open water setting if the currents and waves are within specific limits.

The measurement of bubble size distribution required mounting of a relatively large and heavy low-frequency transducer and receiver on top of the ROV. This sensor configuration severely affected the stability, controllability and flight dynamics of the vehicle. While extensive ballasting measures allow the vehicle to become stable, it was still difficult to control and move. A larger ROV would be able to deal with the size and mass of the low frequency sensor much more effectively. For the purposes of research deployment at Ohmsett, the setup was functional but unlike the measurement of oil slick thickness, it would be too difficult to use in an open water deployment scenario.

To better understand the influence of sea state on vehicle motion and thus measurement precision, the team designed and built a custom inertial motion sensor package to quantify the motion of the vehicle while making oil slick thickness measurements as well as subsurface measurements of gas bubble distribution measurement and dispersant effectiveness.

The technical progress made to measure the gas bubble size distribution using acoustic backscattering is significant and opens the opportunity to provide gas bubble size measurements as well as oil dispersant effectiveness from a single set of acoustic sensors on a single platform. The measurements of oil droplet scattering related to dispersant efficiency show the proof of concept from ROV platforms and produced results similar to static platforms from previous work. We advanced these capabilities to TRL 6 through multiple measurements at Ohmsett in many spill scenarios including surface slicks in various sea states and subsurface releases of methane and dispersed oil.

6. REFERENCES

Greinert, J., & Nützel, B. (2004). Hydroacoustic experiments to establish a method for the determination of methane bubble fluxes at cold seeps. Geo-Marine Letters, 24(2), 75-85.

Ainslie, M. A., & McColm, J. G. (1998). A simplified formula for viscous and chemical absorption in sea water. The Journal of the Acoustical Society of America, 103(3), 1671-1672.

Commander, K. W., & Prosperetti, A. (1989). Linear pressure waves in bubbly liquids: Comparison between theory and experiments. The Journal of the Acoustical Society of America, 85(2), 732-746.

Medwin, H., & Clay, C. S. (1997). Fundamentals of acoustical oceanography. Academic Press.

Leighton, T. (2012). The Acoustic Bubble. Academic press

Panetta, P. D., McElhone, D., Carr, L., & Winfield, K. (2015). Acoustic Tool to Measure Oil Slick Thickness at Ohmsett For US Department of the Interior Bureau of Safety and Environmental Enforcement (BSEE).

Panetta, P. D., McElhone, D., Winfield, K., & Cartwright, G. (2014, May). Ultrasonic Scattering Measurements of Dispersed Oil Droplets in the Presence of Gas. In International Oil Spill Conference Proceedings (Vol. 2014, No. 1, pp. 266-282). American Petroleum Institute.

APPENDIX: INERTIAL POSITIONING MEASUREMENTS OF UNMANNED UNDERWATER VEHICLE (UUV) DYNAMICS

INTRODUCTION

This report is part of an ongoing study, of which main purpose is to develop innovative techniques for characterizing the size and flow rate of crude oil slicks and subsurface release, respectively. These techniques include (1) the measurement of oil slick thickness using the compression wave speed of oil and (2) the measurement of subsurface oil droplet size using ultrasonic backscattering. Both of these techniques are implemented using ultrasonic transducers, which emit and receive sound at an angle nominally normal to the slick surface or plume. However, limited UUV controllability in a stochastic open water environment prevents a singular transducer from remaining continuously normal to the slick or plume.

This problem is overcome by considering an array of several transducers positions at a range of off-axis angles, such that the probability of at least one transducer being sufficiently perpendicular to the target is substantially increased. For this reason it is important to characterize the dynamic response of an acoustic measurement UUV in stochastic conditions. Identifying the probabilistic angular orientation of a UUV will (1) improve the understanding of how angular displacements from normal influence effectiveness of the current technique and (2) aid in transducer array design for a future acoustic measurement UUV prototype.

The purpose of this paper is to characterize the dynamic response of UUVs during wave tests at OHMSETT, where acoustic measurements were made in conjunction with dynamic measurements. A Seabotix LBV150^2 ROV and a Teledyne Slocum Electric Glider were each used as platforms for measurement of oil slick thickness. The ROV was subsequently used as a platform for measurement of subsurface oil release in calm conditions; however, this paper principally addresses dynamics of UUVs during slick thickness measurement. (Data regarding ROV dynamics during subsurface release measurement is included separately in section 5). Of primary interest are the pitch (fore-to-aft rotation) and roll (port-to-starboard rotation) of each UUV during acoustic measurement, as well as the probabilistic distribution of these rotations. Additional investigated properties include the body-fixed 3-axis acceleration of each UUV, as well as the measurable oscillatory motion of the UUV (if present) that was induced by the amalgamation of deliberate control input and wave conditions.

BACKGROUND

Data was recorded using a Bosch 9-DOF absolute orientation sensor and a Raspberry Pi Zero. The sensor uses a black box fusion algorithm to derive Euler angles and linear acceleration from accelerometer, rate gyroscope, and magnetometer data. To address concerns regarding the interference of iron trusses present in the OHMSETT facility and the linearization techniques used in the fusion algorithm, raw accelerometer and rate gyroscope measurements were also recorded to be used for a duplicate, posterior reconstruction of pitch and roll. Measurements were sampled at an effective rate of approximately 30Hz, which was substantially higher than Nyquist frequency of possible wave conditions in OHMSETT's wave tank. The maximum allowable data output rate for the Bosch 9-DOF sensor is 100Hz for all of fused absolute orientation, linear acceleration, acceleration, and angular velocity. The accelerometer is capable of measuring within the range and zero-g offset of ±39.2m/s^2 ± 1.47m/s^2, while the gyroscope is capable of measuring within the range and zero-rate offset of ±34.91rad/s ± 0.05rad/s.

DATA PROCESSING

Coordinate Transformations

The UUV body-fixed coordinate system is defined by the x-axis-to-forward, y-axis-to-starboard, z-axis-to-downward convention. Positive angular position about each axis is defined using a counterclockwise convention. To circumvent the numerous differing conventions that can be used to define pitch and roll, angular positions from this point onward will be referred to as "X Euler," "Y Euler," and "Z Euler;" where "X Euler" is the counterclockwise rotation angle in degrees about the x-axis. The posterior reconstruction of X Euler will later be referred to as "Phi," while the posterior reconstruction of Y Euler will later be referred to as "Theta."

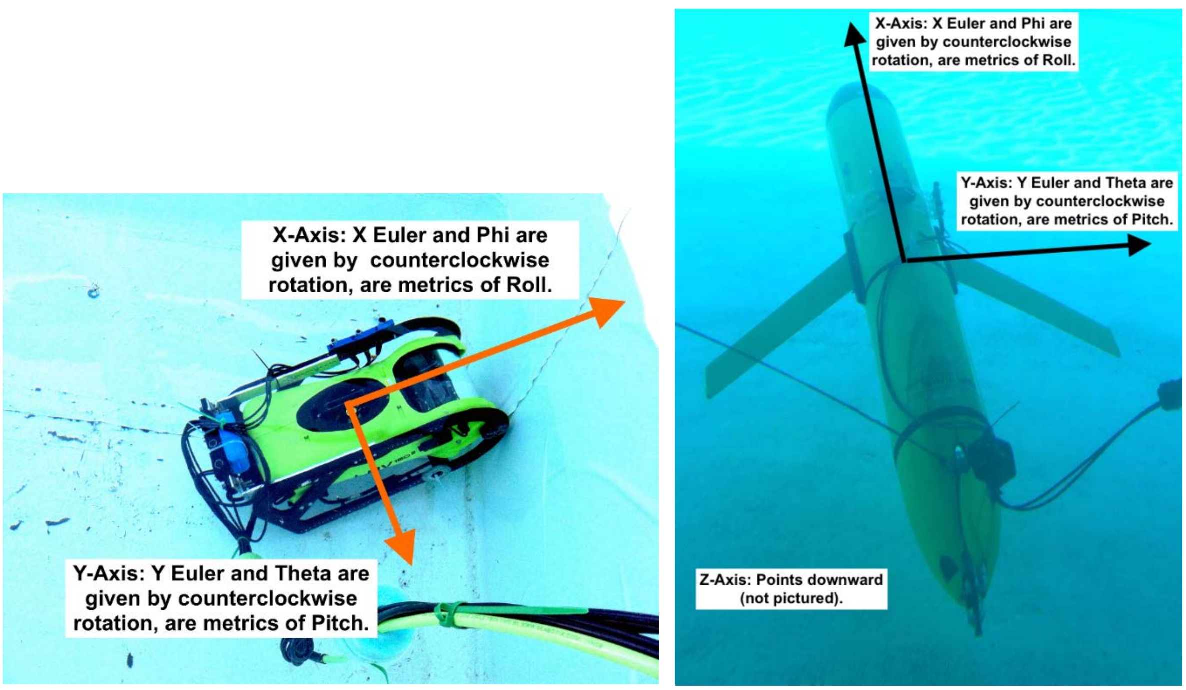

Figure 1: UUV body-fixed coordinate system. Showing axes conventions used for linear acceleration and angular position. The demonstrated convention was used for both the Slocum Glider and the Seabotix ROV (shown).

Electronic components of the measurement device were housed in a 1.4x3.1x 4.4cm waterproof, pressure-resistance case. This case was mounted on the ROV and Slocum Glider in a position that would allow for predicted minimal effect on the overall buoyancy and dynamics of each vehicle.

Figure 2: Mounting of the measurement device. Showing position of measurement device on (a) Seabotix ROV and (b) Slocum Gilder. Waterproof case was placed inside of a protective pressure-resistant bag with air removed to protect from crude oil contamination.

Measurements were subsequently transformed using a direction cosine matrix from the case-fixed coordinate system onto the UUV body-fixed coordinate system. The direction cosine matrix was used to transform measurements as follows [1]:

$$\mathbf{a} = \begin{bmatrix} a_x \\ a_y \\ a_z \end{bmatrix} \qquad \mathbf{R} = \begin{bmatrix} \cos\psi_{xc,xb} & \cos\psi_{xc,yb} & \cos\psi_{xc,zb} \\ \cos\psi_{yc,xb} & \cos\psi_{yc,yb} & \cos\psi_{yc,zb} \\ \cos\psi_{zc,xb} & \cos\psi_{zc,yb} & \cos\psi_{zc,zb} \end{bmatrix} \qquad \mathbf{a_{body}} = \mathbf{R^T}\,\mathbf{a_{case}} = \mathbf{R^{-1}}\,\mathbf{a_{case}}$$

$$\mathbf{E} = \begin{bmatrix} XEuler \\ YEuler \\ ZEuler \end{bmatrix} \qquad \mathbf{E_{body}} = \mathbf{E_{case}} - \begin{bmatrix} \psi_{xc,xb} \\ \psi_{yc,yb} \\ \psi_{zc,zb} \end{bmatrix}$$

$$\psi_{xc,xb} = \psi_{zc,zb} = \beta$$
$$\psi_{xc,zb} = \frac{\pi}{2} + \beta$$
$$\psi_{zc,xb} = \frac{\pi}{2} - \beta$$
$$\psi_{xc,yb} = \psi_{yc,xb} = \psi_{yc,zb} = \psi_{zc,yb} = \frac{\pi}{2}$$
$$\psi_{yc,yb} = 0$$

In this system, $\mathbf{a}$ is a vector of accelerations, $\mathbf{E}$ is a vector of Euler angles, and $\psi_{yc,xb}$ is the angle between the case-fixed y-axis and the body-fixed x-axis. The angle β is the rotation angle about the (unchanging) y-axis *from the body-fixed coordinate system to the case-fixed coordinate system*. For both mounting cases shown in Figure 1, the angle β is acute and negative. The angle β is determined prior to coordinate transformation by plotting the pre-transformed Y Euler (and its posterior reconstruction Theta), locating a region of the plot for which the UUV was resting motionless on the deck or bottom of the wave tank, and recording this approximate angle. Angles were probed at the commencement of the resting period to avoid additional error from gyroscopic drift.

Data File Name	Test Configuration	β (From Y Euler)	β (From Theta)	Averaged β
Feb-22_09_19_38.csv (Test 12 through 18)	ROV Slick Thickness	-5.6°	-5.6°	-5.6°
Feb-22_13_13_06.csv (Test 19a through 20e)	ROV Slick Thickness	-5.7°	-5.0°	-5.35°
Feb-23_09_12_47.csv (Test 29 through 30)	Glider Slick Thickness	-13.5°	-13.7°	-13.6°

Figure 3: Empirically determined approximate offset angle. Showing offset angle β to be used in coordinate transformation of accelerations using direction cosine matrix and rotational transformations of angular position vectors.

Posterior Approximation of Euler Angles

Angular position was posteriorly reconstructed from raw accelerometer and rate gyroscope data using a linear approximation algorithm. The posterior reconstructions of X Euler and Y Euler are referred to as "Phi" and "Theta," respectively. The approximation algorithm combines low-pass filtered acceleration data with high-pass filtered rate gyroscope data to prevent gradual gyroscopic drift. Frequency domain equations for Phi and Theta are given as follows [2]:

$$\phi(s) = -\frac{a_y(s)}{g}\left(\frac{1}{\tau s+1}\right) + \frac{\omega_x(s)}{s}\left(\frac{\tau s}{\tau s+1}\right)$$

$$\theta(s) = \frac{a_x(s)}{g}\left(\frac{1}{\tau s+1}\right) + \frac{\omega_y(s)}{s}\left(\frac{\tau s}{\tau s+1}\right)$$

In this system, a_y is the y-axis component of raw acceleration (m/s^2), g is the gravitational acceleration (m/s^2) in the z-axis direction, and ω_x is the x-axis component of angular velocity (rad/s). The parameter τ is an approximate time constant of the linearized time-invariant system. A time constant of 1/3 was selected for the algorithm. The posterior approximation of angular was evaluated for similarity to the Bosch sensor's fusion algorithm using data collected during both Seabotix ROV and Slocum Glider movement.

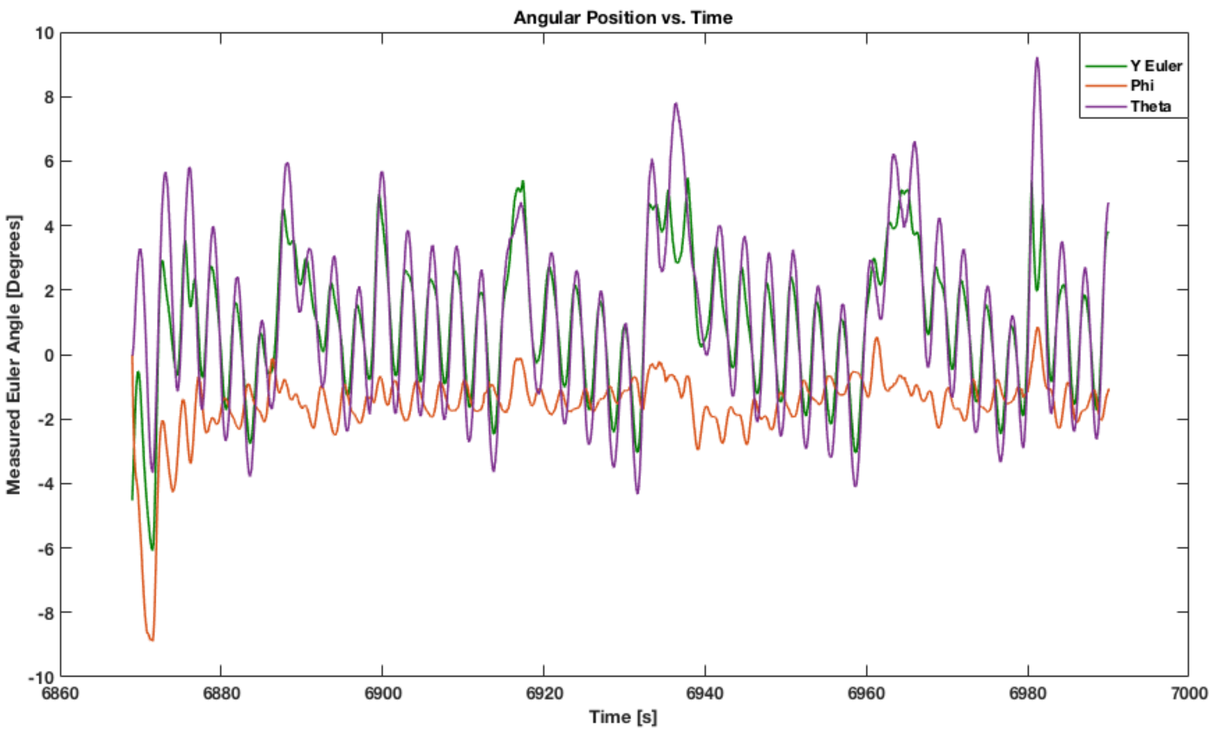

Figure 4: Comparison of Bosch sensor fusion algorithm vs. posterior approximation for Test 14b. Showing Seabotix ROV angular position in wave conditions.

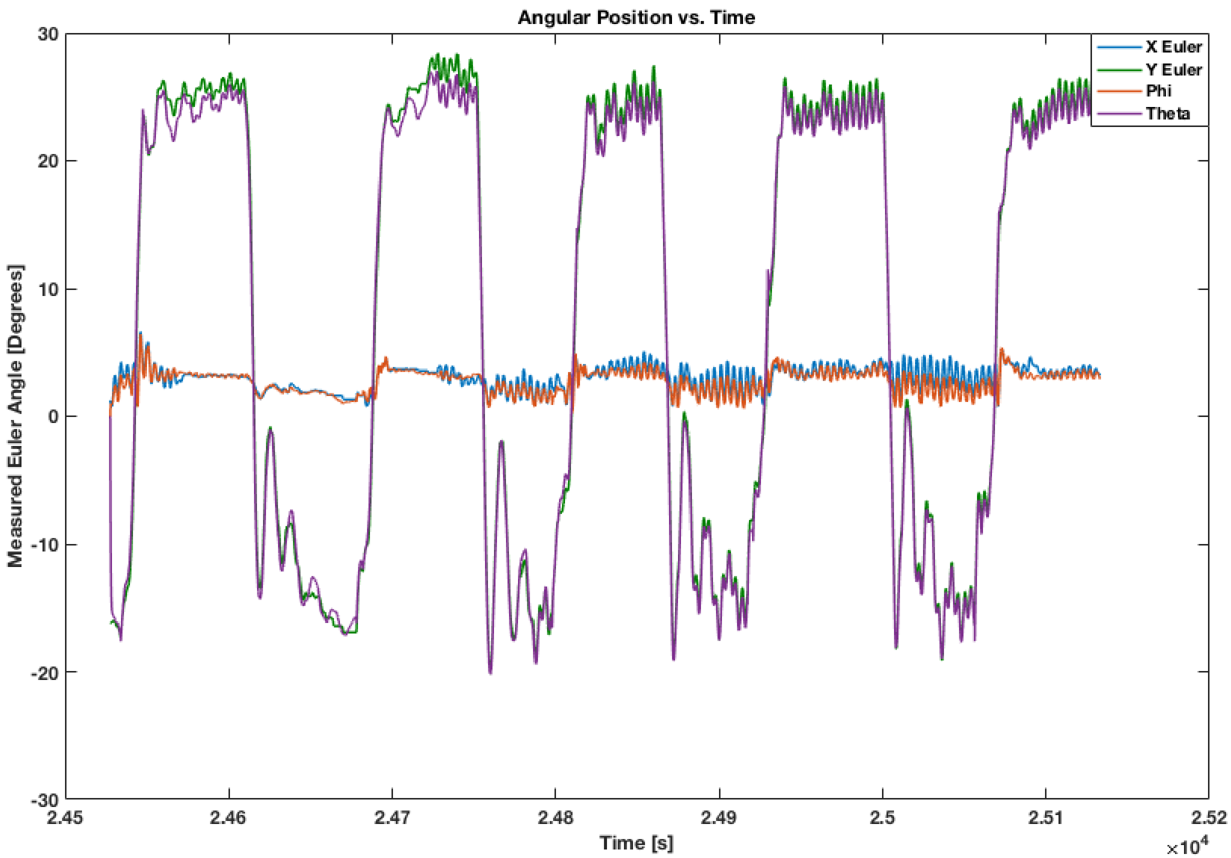

Figure 5: Comparison of Bosch sensor fusion algorithm vs. posterior approximation for Test 30. Showing Slocum Glider angular position during a diving and surfacing procedure.

Filtering

Linear acceleration data was filtered using a bilinear transform filter in order to remove high frequency electrical noise [2]. A bandwidth of 3Hz was selected for the filter. Raw and filtered linear acceleration data was examined to verify effectiveness of the selected bandwidth.

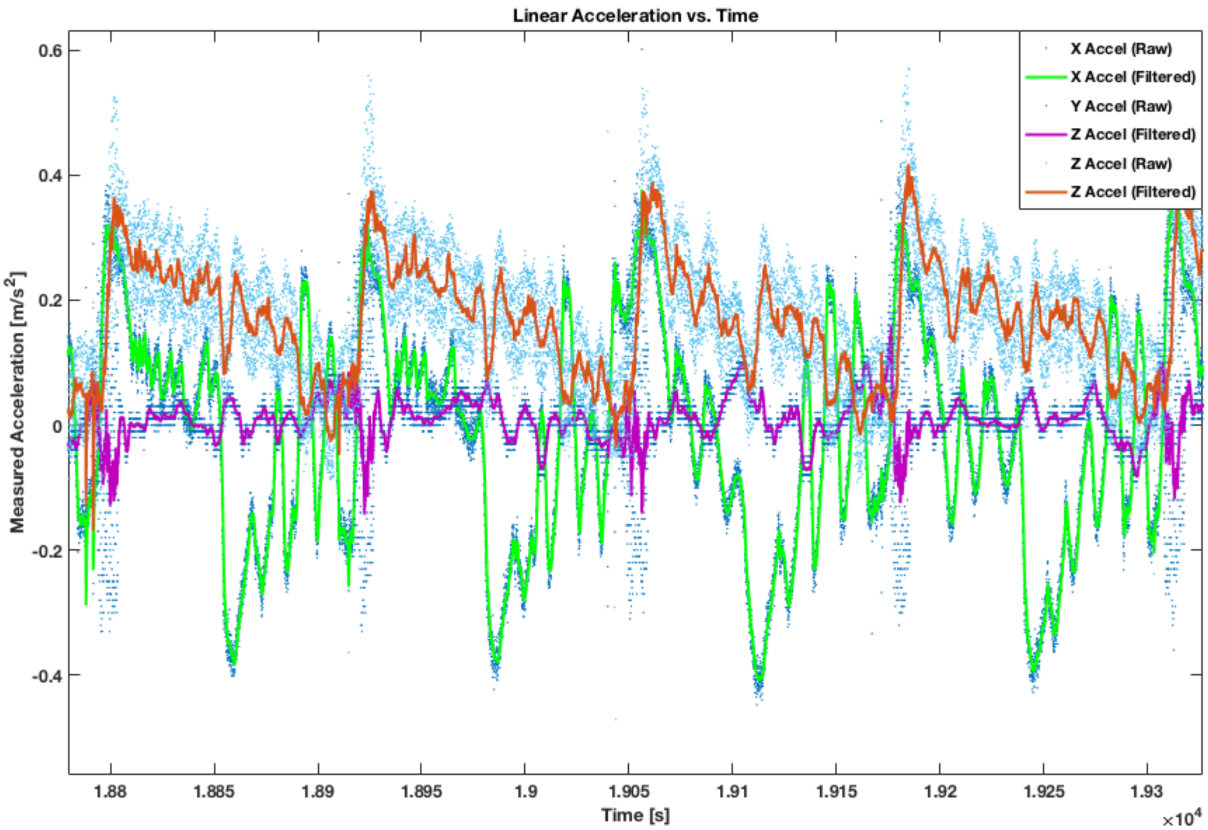

Figure 6: Comparison of raw linear accelerations vs. filtered linear accelerations for a preliminary maneuver that occurred before Test 29. Showing linear accelerations during a preliminary Slocum Glider diving and surfacing procedure.

Cross-Correlation

Cross-correlation of 3-axis acceleration signals was used to investigate the overall influence of wave conditions on UUV motion during each test. It is important to note that for the Seabotix ROV, periodicity of acceleration signals is the result of both stochastic conditions in the wave tank as well as active control from the ROV operator. A peak prominence algorithm was used to detect periodicity in each cross-correlation plot.

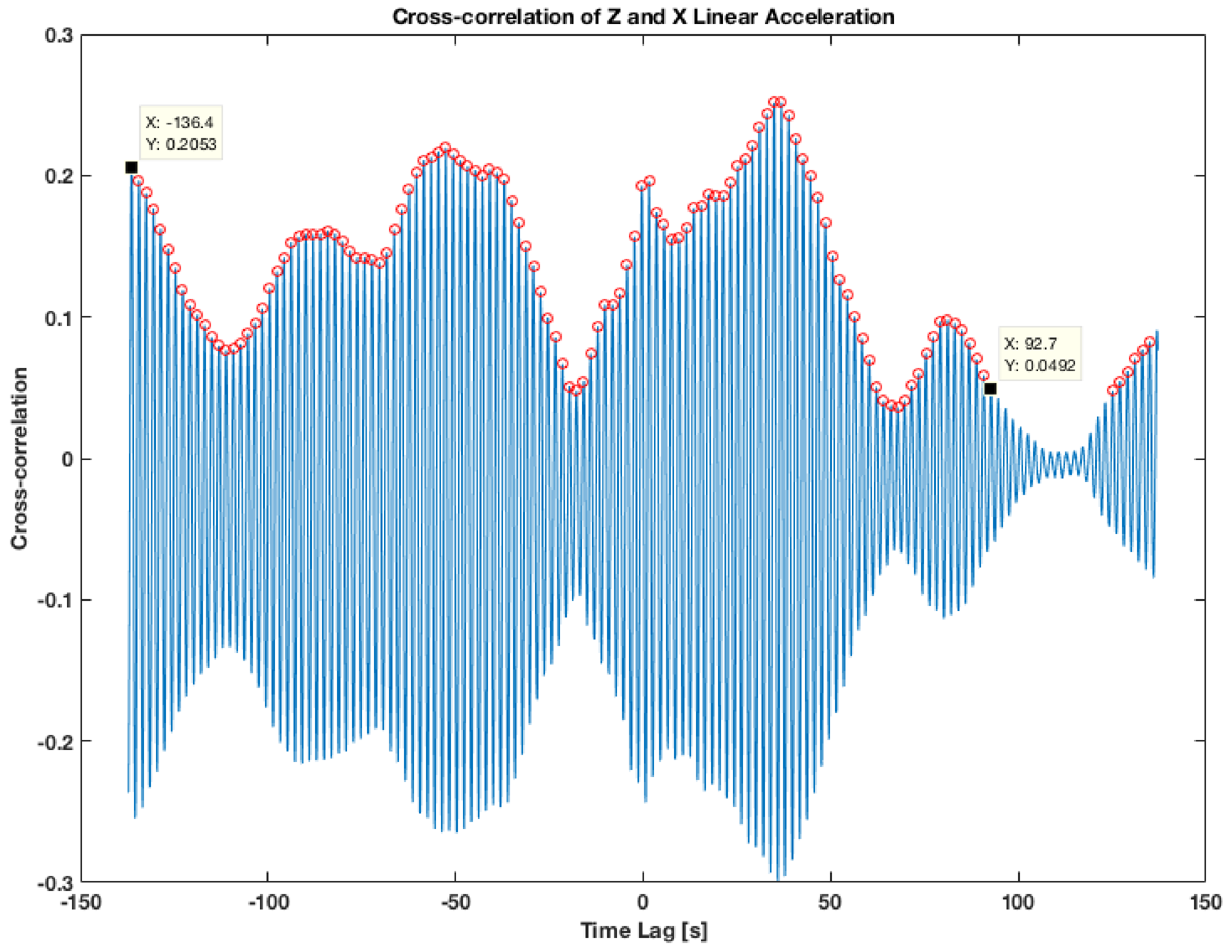

Figure 7: Cross-Correlation plot of ROV linear acceleration for Test 19c. Showing peak detection using a minimum threshold height of 0.1. Frequency of UUV motion was approximated from the mean difference in peak locations within the time lag domain of contiguously detected peaks (shown with annotation).

Metrics of Angular Position

Univariate histograms, bivariate histograms, and descriptive statistics were used to derive probabilistic information about the pitch and roll during wave tests. For tests using the Seabotix ROV, mean and standard deviation were of primary interest. Glider tests were characterized in terms of dive and climb angle, for the reason that mean and standard deviation of measurements for a full test would be of little meaning in a multimodal distribution.

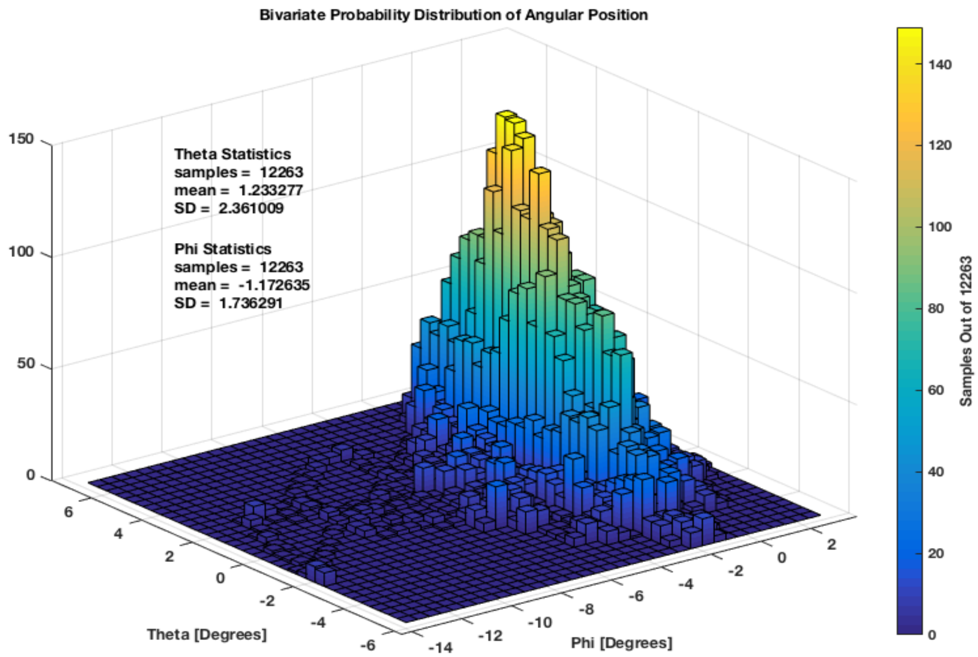

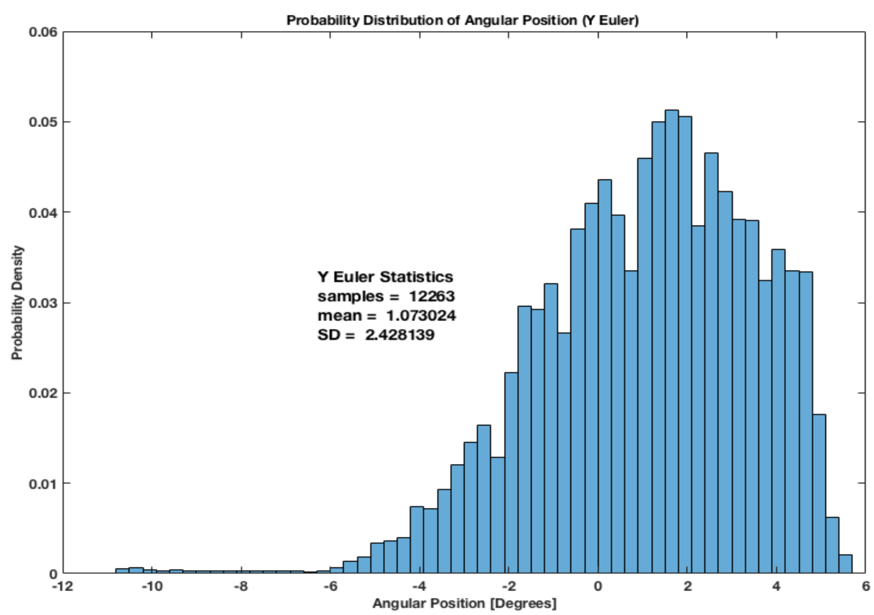

Figure 8: Probability distribution through time of Seabotix ROV angular position for Test 13. Showing **(a)** a univariate histogram for pitch (Y Euler) derived from the Bosch fusion algorithm and **(b)** a bivariate histogram for pitch (Theta) vs. roll (Phi) derived from the posterior approximation.

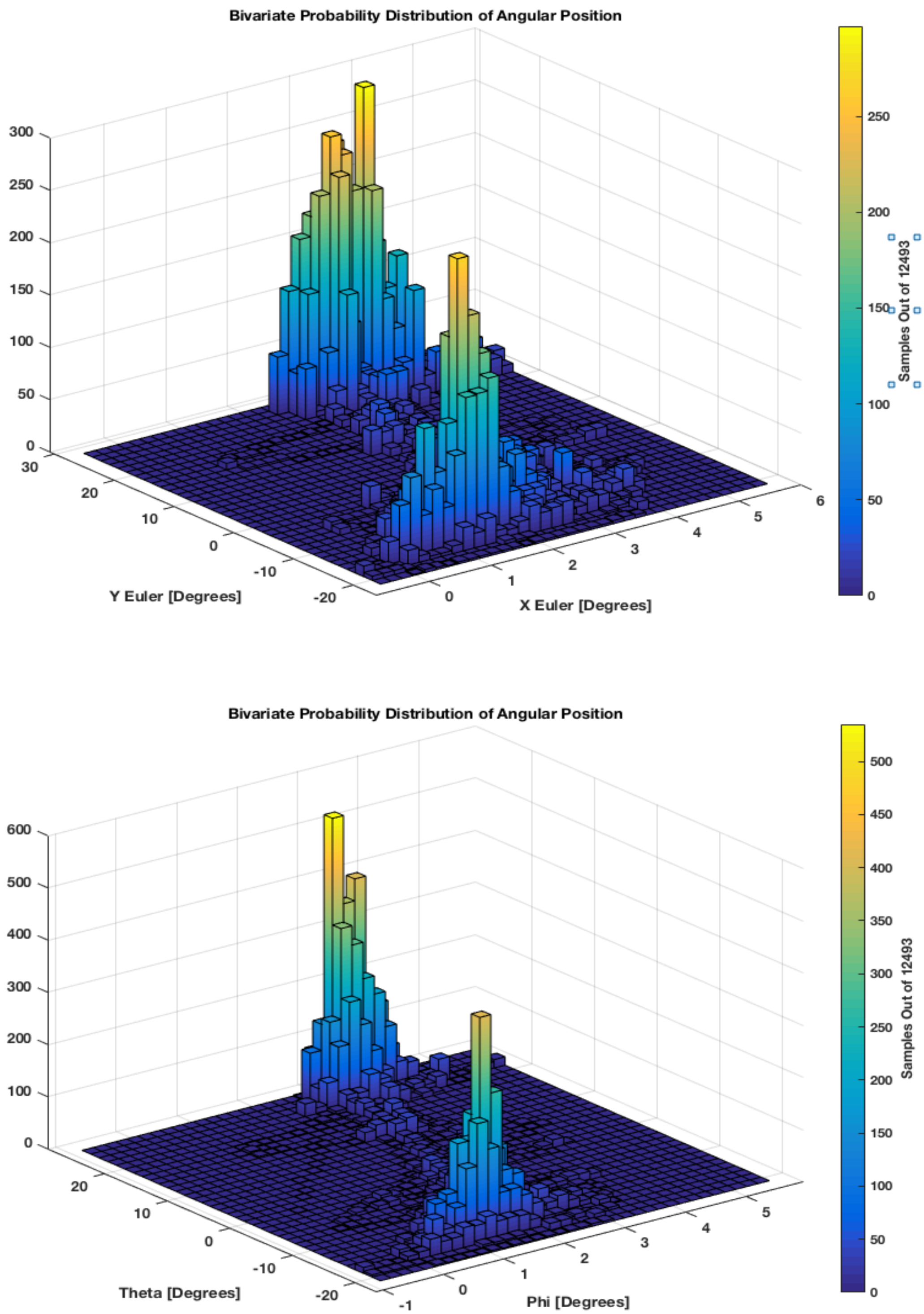

Figure 9: Probability distribution through time of Slocum Glider angular position for Test 29. Showing bivariate histograms for pitch (Y Euler, Theta) vs. roll (X Euler, Phi) derived from **(a)** the Bosch fusion algorithm and **(b)** the posterior approximation.

RESULTS

Test	Mean Wave Height [m]	Significant (Highest 1/3) Wave Height [m]	Mean Wavelength [m]	WMO Sea State	Wave Frequency [Hz]
12	0.4851	0.5867	12.3444	3 (Slight)	0.33
13	0.3302	0.3785	12.1615	2 (Smooth)	0.33
14a	0.4039	0.4267	12.1310	2 (Smooth)	0.33
14b	0.4039	0.4267	12.1310	2 (Smooth)	0.33
15	0.1219	0.2235	11.1862	2 (Smooth)	0.35
16	0.5029	0.5715	11.9786	3 (Slight)	0.33
17	0.5436	0.5918	11.9786	3 (Slight)	0.33
18	0.1676	0.2845	11.5824	2 (Smooth)	0.34
19a	0.0991	0.1219	6.4618	2 (Smooth),	0.49
19b	0.0533	0.0889	3.2004	1 (Calm)	0.70
19c	0.0635	0.1016	4.7244	2 (Smooth)	0.57
19d	0.1092	0.1803	5.9131	2 (Smooth)	0.51
20a	0.1702	0.2286	2.9261	2 (Smooth)	0.73
20b	0.1549	0.2388	3.6881	2 (Smooth)	0.65
20c	0.1524	0.2337	3.5357	2 (Smooth)	0.66
20d	0.0914	0.1448	3.6881	2 (Smooth)	0.65
20e	0	0	0	0 (Calm)	None
29	0.0406	0.0711	16.3373	1 (Calm)	0.26
30	0.0432	0.0838	15.1486	1 (Calm)	0.28

Figure 10: Summary of wave conditions. Showing mean and significant wave heights, mean wavelength, World Meteorological Organization sea state code, and wave frequency. Wave frequency was determined using the intermediate dispersion relation and a wave tank depth of 2.4 meters.

Test	Wave Frequency [Hz]	Acceleration Cross-correlation (XY, YZ, ZX) [Hz]	Mean Angular Position	Standard Deviation	Time Interval [Min.]
12	0.33	0.34, 0.35, 0.34	Phi -1.30°	Phi = 1.52°	73-82

			Y Euler = 0.46° Theta = 1.57°	Y Euler = 2.23° Theta = 3.28°	
13	0.33	0.34, 0.33, 0.33	Phi = -1.17° Y Euler = 1.07° Theta = 1.28°	Phi = 1.79° Y Euler = 2.43° Theta = 2.36°	84-91
14a	0.33	0.34, 0.34, 0.34	Phi = -0.77° Y Euler = 1.33° Theta = 1.79°	Phi = 2.08° Y Euler = 2.23° Theta = 2.97°	92-100
14b	0.33	0.34, 0.34, 0.34	Phi = -1.55° Y Euler = 0.97° Theta = 1.05°	Phi = 1.07° Y Euler = 1.99° Theta = 2.53°	115-117
15	0.35	Low, 0.25, 0.25	Phi = -1.09° Y Euler = 0.81° Theta = 1.36°	Phi = 1.59° Y Euler = 2.40° Theta = 2.91°	120-126
16	0.33	0.34, 0.34, 0.34	Phi = -1.50° Y Euler = 0.61° Theta = 2.05°	Phi = 1.44° Y Euler = 2.47° Theta = 3.64°	131-138
17	0.33	0.34, 0.34, 0.34	Phi = -1.15° Y Euler = 0.37° Theta = 1.55°	Phi = 1.69° Y Euler = 2.94° Theta = 4.36°	140-147
18	0.34	0.34, 0.34, 0.34	Phi = -0.60° Y Euler = 0.20° Theta = 1.05°	Phi = 2.33° Y Euler = 2.71° Theta = 3.40°	150-157
19a	0.49	0.50, 0.51, 0.50	Phi = -2.13° Y Euler = 0.51° Theta = 3.00°	Phi = 2.29° Y Euler = 2.35° Theta = 3.62°	27-34
19b	0.70	0.51, 0.51, 0.50	Phi = -2.48° Y Euler = 0.32° Theta = 2.06°	Phi = 2.40° Y Euler = 1.94° Theta = 1.99°	34-41
19c	0.57	0.51, 0.51, 0.52	Phi = -2.21°	Phi = 2.60°	42-49

			Y Euler = -0.51° Theta = 1.77°	Y Euler = 3.94° Theta = 4.70°	
19d	0.51	0.51, 0.51, 0.50	Phi = -1.98° Y Euler = 0.63° Theta = 2.28°	Phi = 1.35° Y Euler = 2.97° Theta = 3.47°	52-59
20a	0.73	Low, 0.73, 0.73	Phi = -1.87° Y Euler = -0.03° Theta = 2.97°	Phi = 2.24° Y Euler = 4.76° Theta = 6.02°	75-82
20b	0.65	Low, 0.61, 0.62	Phi = -2.72° Y Euler = -0.21° Theta = 3.90°	Phi = 2.46° Y Euler = 3.56° Theta = 4.72°	84-91
20c	0.66	0.58, 0.58, 0.58	Phi = -1.75° Y Euler = 1.71° Theta = 3.14°	Phi = 1.79° Y Euler = 1.68° Theta = 2.08°	92-99
20d	0.65	Low, Low, Low	Phi = -1.89° Y Euler = 0.94° Theta = 2.32°	Phi = 1.97° Y Euler = 2.53° Theta = 3.20°	99-107
20e	None	Low, Low, Low	Phi = -1.84° Y Euler = 1.77° Theta = 3.56°	Phi = 1.22° Y Euler = 1.58° Theta = 2.62°	117-122

Figure 11: Summary of Seabotix ROV dynamic response. Showing ROV periodicity of motion in comparison to wave frequency, and descriptive statistics for angular position through time.

Test	Wave Frequency* [Hz]	Acceleration Cross-correlation (XY, YZ, ZX) [Hz]	Peak Climb Angle	Dive Angle	Time Step (Min.)
29	0.26	Low, 0.25, Low	Y Euler = 25.50° Theta = 25.35°	Y Euler = -15.77° Theta = -15.60°	401-408
30	0.28	Low, 0.25, Low	Y Euler = 25.64° Theta = 25.68°	Y Euler = -17.37° Theta = -17.49°	409-419

Figure 12: Summary of Slocum Glider dynamic response. Showing Glider periodicity of motion in comparison to wave frequency, and highest-mode (through time) angles during diving and surfacing procedures.

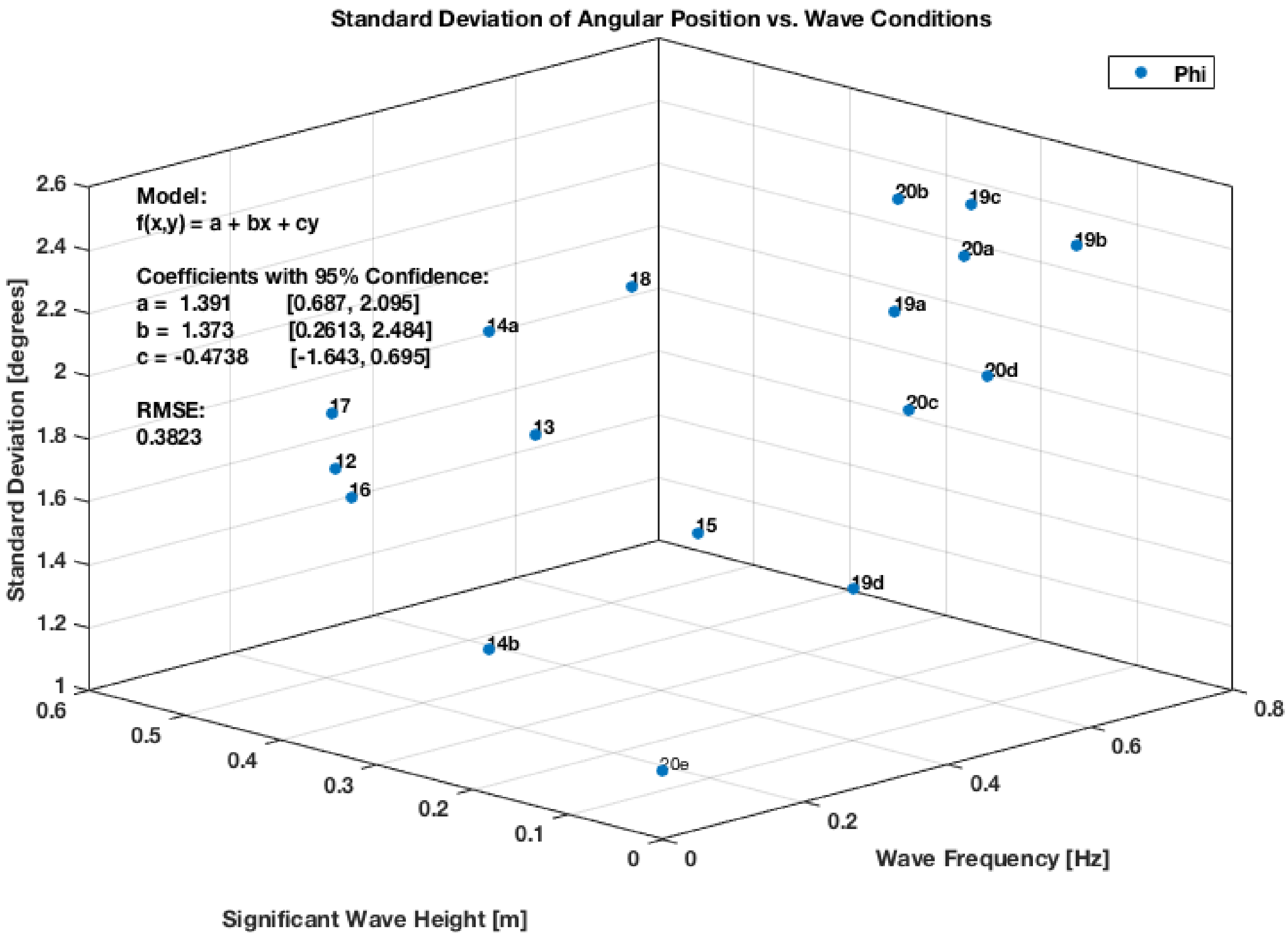

Figure 13: Distribution of Phi standard deviation as a function of wave frequency (*x*) and significant wave height (*y*). The linear fit is given by the equation *f(x,y) = 1.391 + 1.373x - 0.4738y* and carries a root-mean-square error of 0.3823.

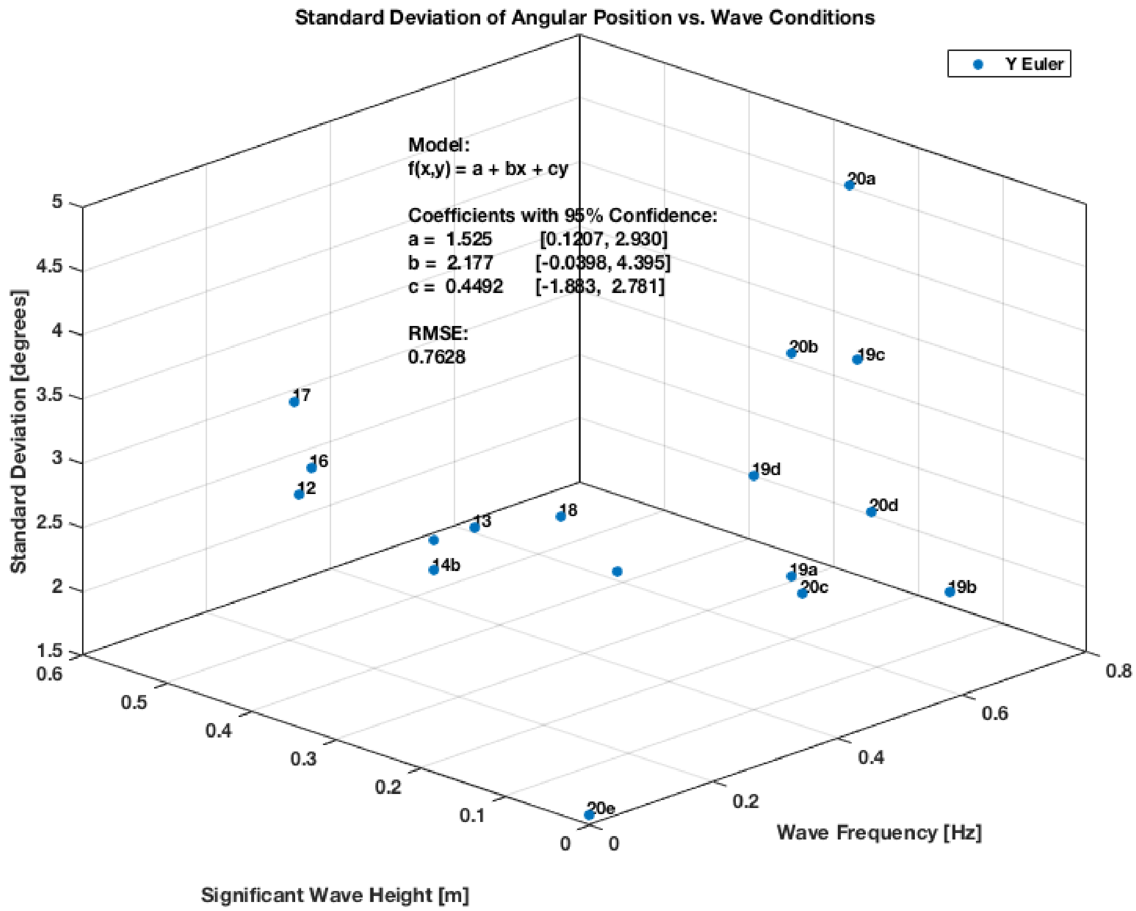

Figure 14: Distribution of Y Euler standard deviation as a function of wave frequency (x) and significant wave height (y). The linear fit is given by the equation $f(x,y) = 1.525 + 2.177x + 0.4492y$ and carries a root-mean-square error of 0.7628.

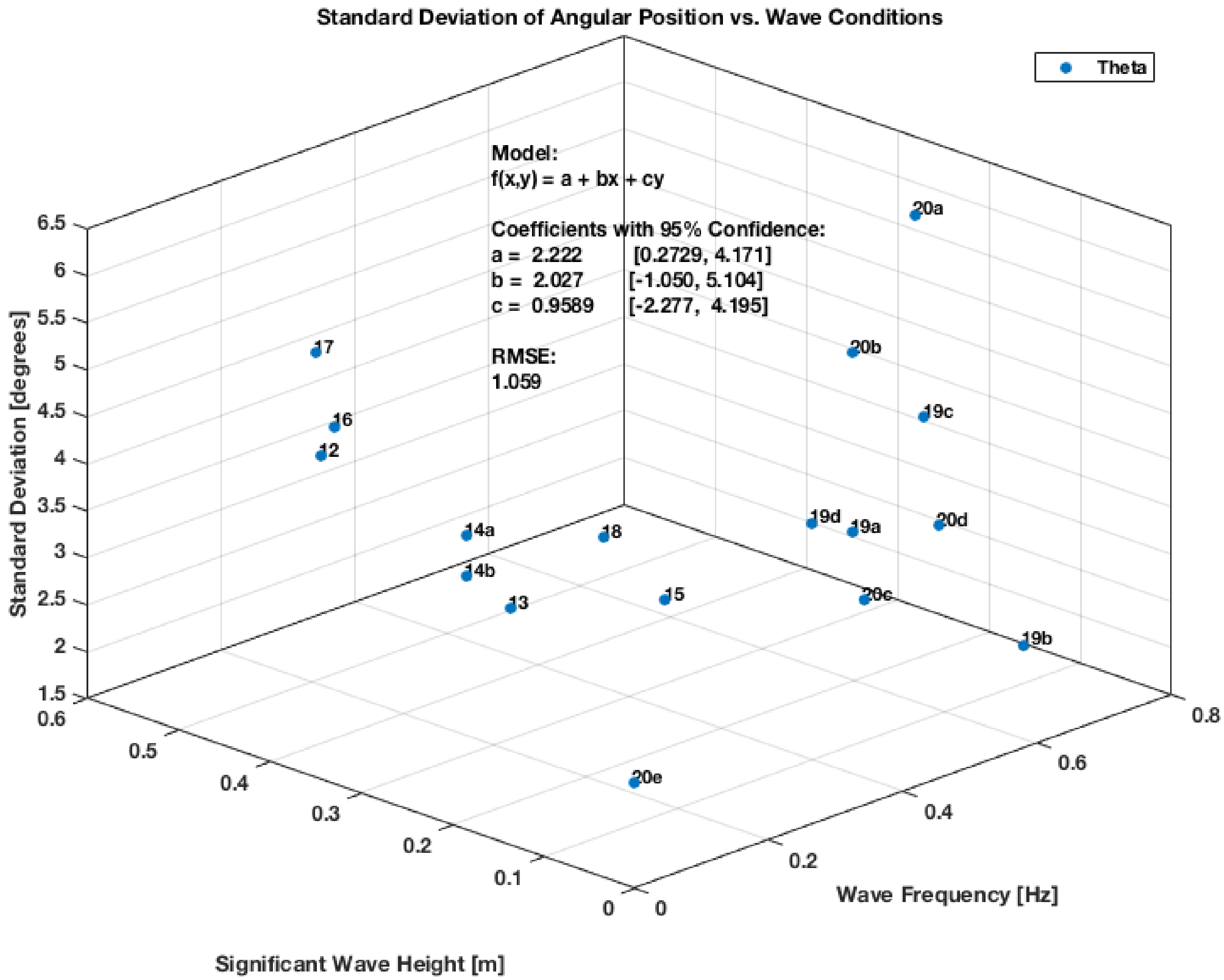

Figure 15: Distribution of Theta standard deviation as a function of wave frequency (*x*) and significant wave height (*y*). The linear fit is given by the equation *f(x,y) = 2.222 + 2.027x + 0.9589y* and carries a root-mean-square error of 1.059.

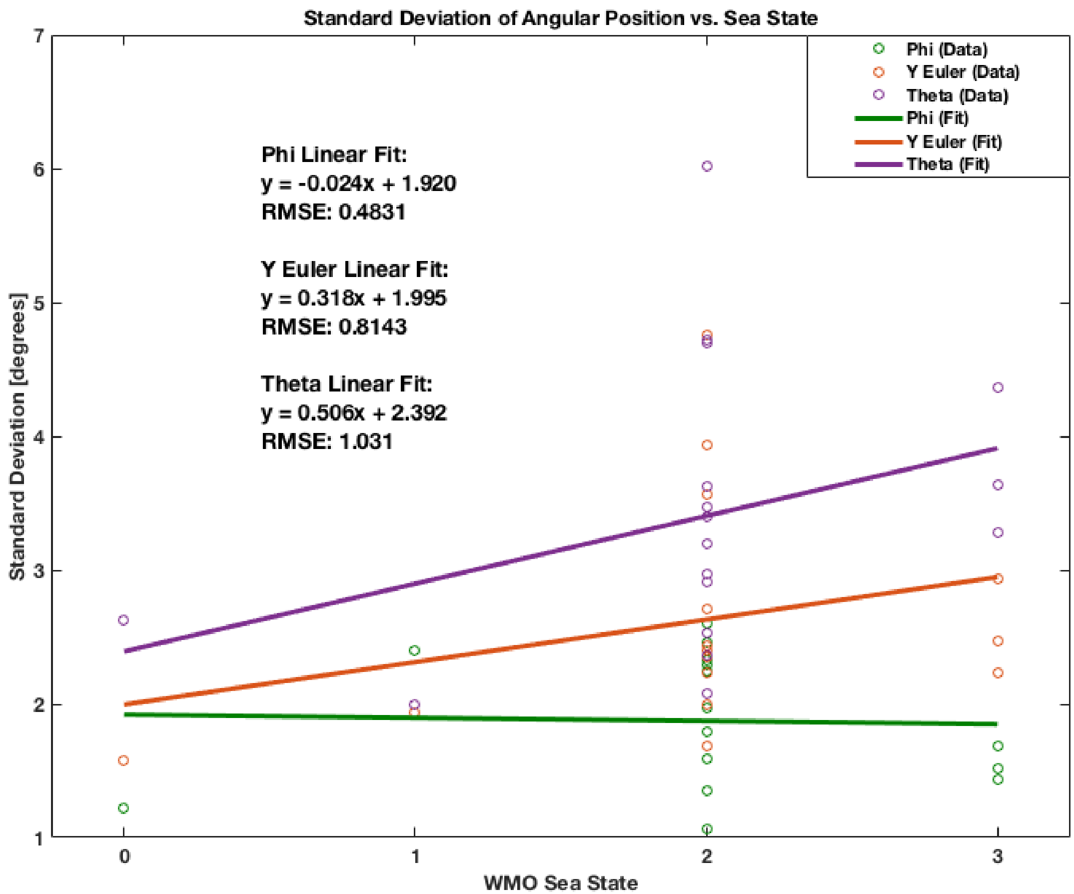

Figure 16: Standard deviation of angular position with respect to WMO sea state. Showing data and linear fits for all tests. The linear fit for Phi is given by the equation *y = -0.024x + 1.920* and carries a root-mean-square error of 0.4831. The linear fit for Y Euler is given by the equation y = 0.318x + 1.995 and carries a root-mean-square error of 0.8143. The linear fit for Theta is given by the equation *y = 0.506x + 2.392* and carries a root-mean-square error of 1.031.

DYNAMICS OF SUBSURFACE RELEASE ROV CONFIGURATION

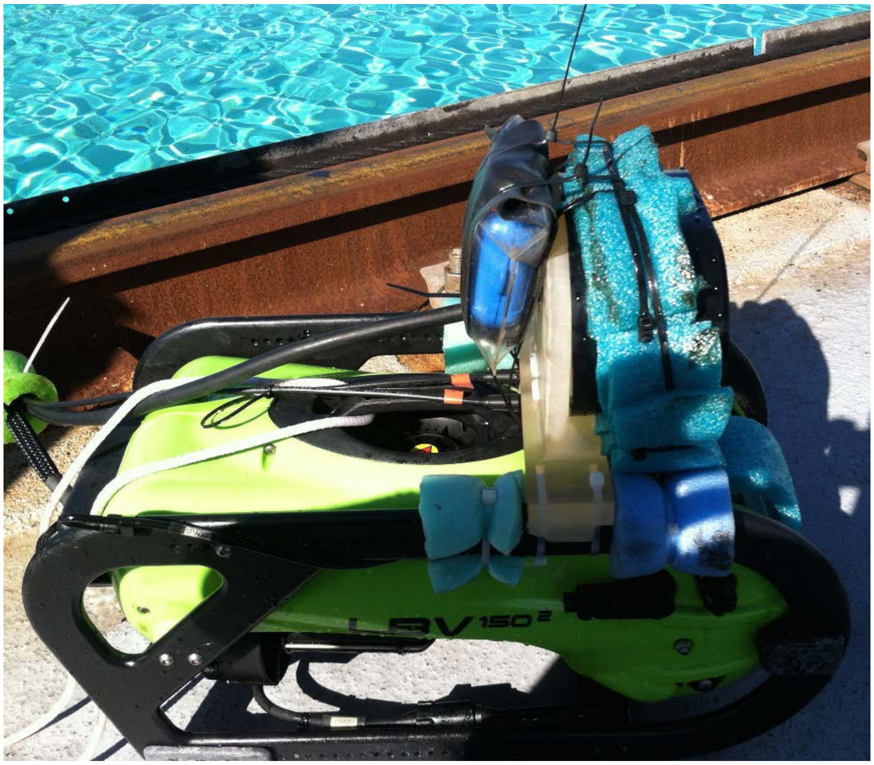

Figure 17: Mounting of the measurement device on the ROV during subsurface release testing. Note that measurement device is mounted directly posterior to the low-frequency transducer (shown wrapped with buoyancy foam).

Data File Name	Test Configuration	β (From Y Euler)	β (From Theta)	Averaged β
Feb-24_10_38_32.csv (Flights A through M)	ROV Subsurface Release	-8.1°	-6.7°	-7.4°

Figure 18: Empirically determined approximate offset angle of subsurface release configuration. Showing offset angle β to be used in coordinate transformation of accelerations using direction cosine matrix and rotational transformations of angular position vectors.

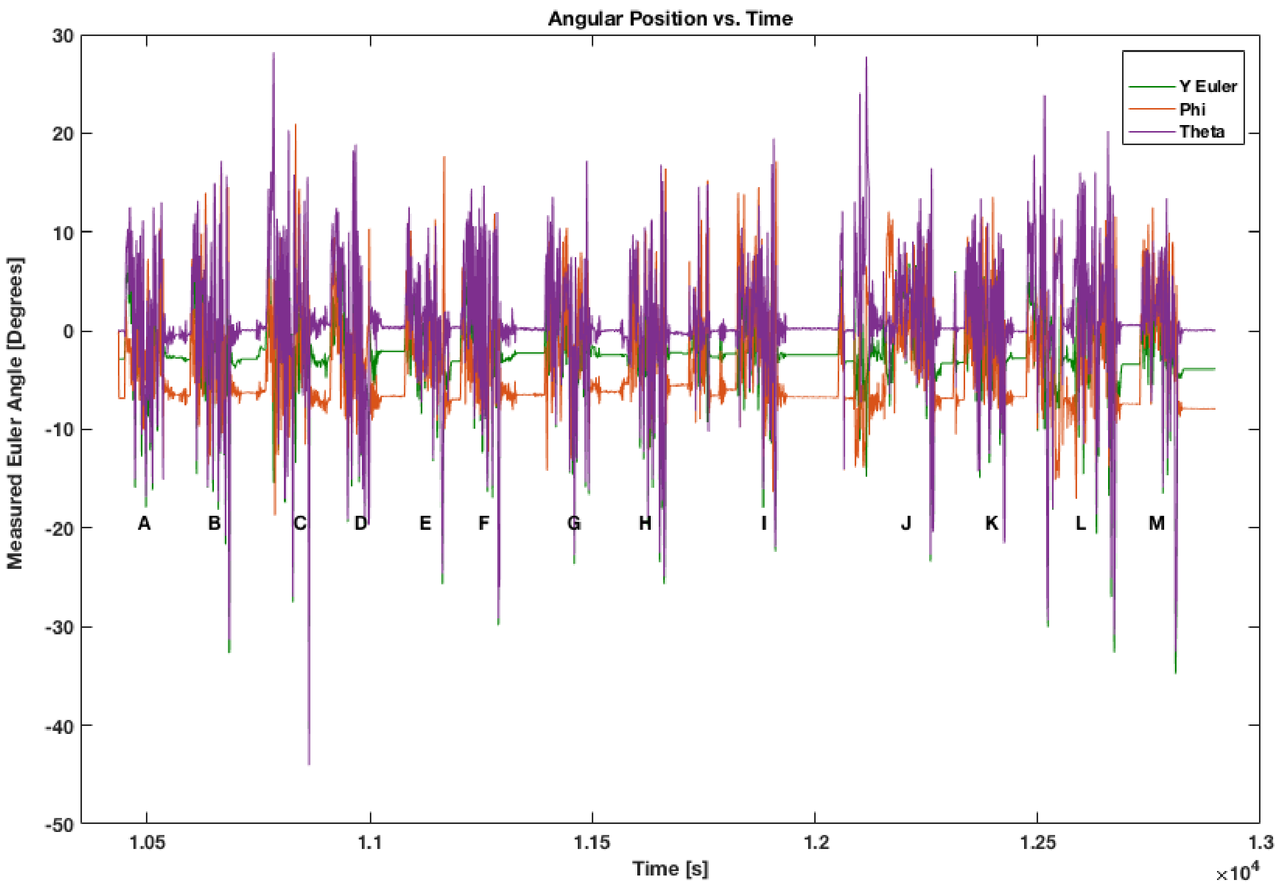

Figure 19: Intermittent flights during subsurface release testing. Showing angular position of Seabotix ROV while quipped with a low-frequency transducer.

Flight	Mean Angular Position	Standard Deviation	Time Interval [Min.]
A	Phi = -2.40° Y Euler = -1.73° Theta = 0.51°	Phi = 3.64° Y Euler = 5.63° Theta = 6.53°	174.00-175.83
B	Phi = -2.11° Y Euler = -3.44° Theta = -0.12°	Phi = 5.58° Y Euler = 6.64° Theta = 7.69°	176.5-178.40
C	Phi = -1.75° Y Euler = -3.40° Theta = 1.95°	Phi = 6.41° Y Euler = 6.68° Theta = 9.36°	179.33-181.33

D	Phi = -3.15° Y Euler = -3.29° Theta = -0.17°	Phi = 3.71° Y Euler = 6.37° Theta = 8.50°	181.83-183.50
E	Phi = -2.44° Y Euler = -2.74° Theta = -0.71°	Phi = 4.16° Y Euler = 5.59° Theta = 5.79°	184.67-186.10
F	Phi = -3.62° Y Euler = -2.75° Theta = 4.08°	Phi = 3.73° Y Euler = 6.31° Theta = 7.88°	186.67-188.40
G	Phi = -1.64° Y Euler = -2.44° Theta = -0.22°	Phi = 4.68° Y Euler = 5.28° Theta = 6.43°	189.83-191.60
H	Phi = -1.60° Y Euler = -3.40° Theta = -1.11°	Phi = 4.56° Y Euler = 7.04° Theta = 8.08°	192.83-194.30
I	Phi = -0.50° Y Euler = -2.31° Theta = 0.59°	Phi = 6.23° Y Euler = 5.83° Theta = 6.68°	197.00-198.50
J	Phi = -1.74° Y Euler = -1.45° Theta = 2.40°	Phi = 5.71° Y Euler = 4.65° Theta = 6.01°	201.50-204.50
K	Phi = -1.61° Y Euler = -1.74° Theta = 0.13°	Phi = 4.88° Y Euler = 5.81° Theta = 6.43°	205.57-207.00
L	Phi = -3.59° Y Euler = -3.74° Theta = 1.33°	Phi = 5.77° Y Euler = 6.77° Theta = 8.76°	208.00-211.00
M	Phi = 1.99° Y Euler = -1.61° Theta = 1.08°	Phi = 4.49° Y Euler = 5.19° Theta = 5.82°	212.17-213.00

Pooled Standard Deviation:	Phi = 5.25° Y Euler = 6.05° Theta = 7.58°

Figure 20: Summary of Seabotix ROV dynamic response during subsurface release testing. Showing mean and standard deviation of angular position through time for flights with low-frequency transducer.

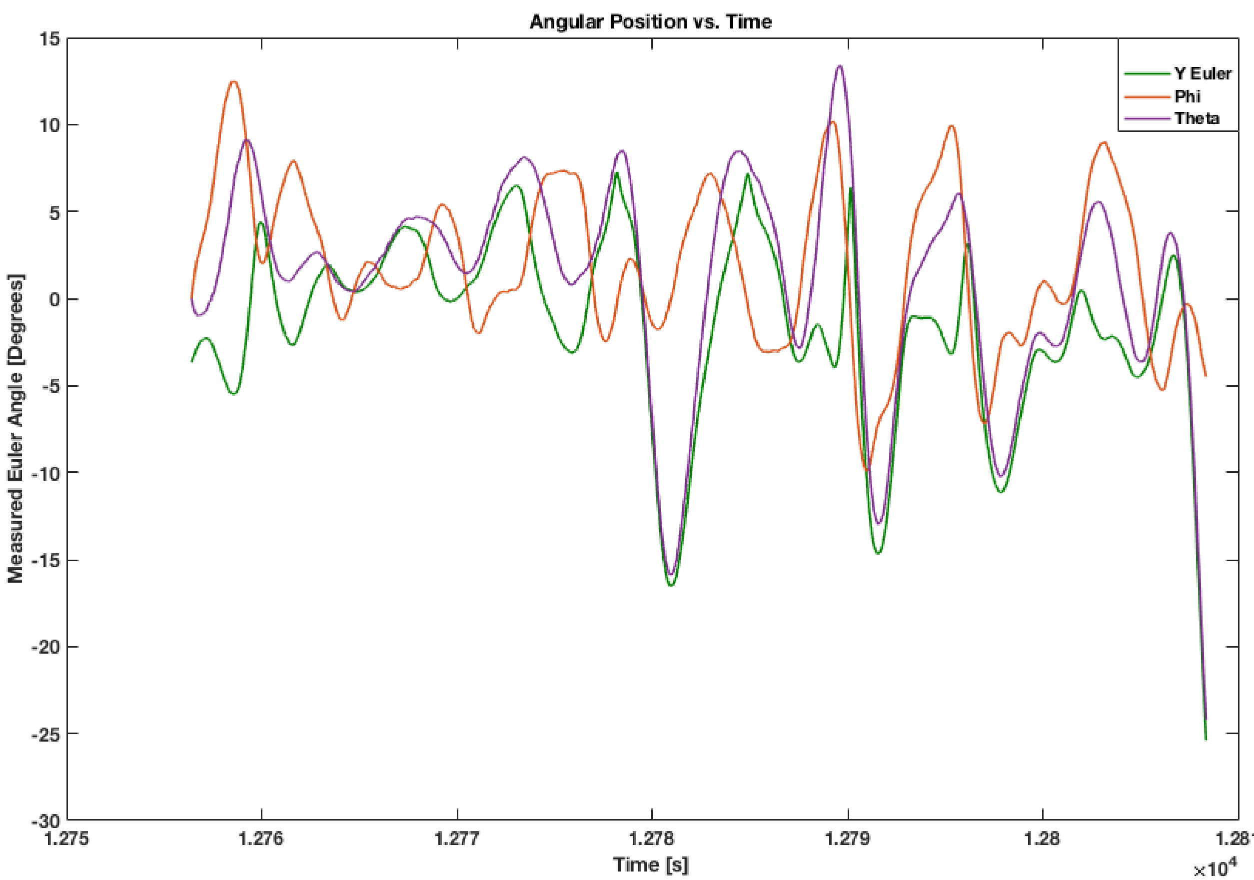

Figure 21: ROV angular position in subsurface release configuration during Flight M. Showing substantial variation in pitch and roll due to amalgamation of control input and the moment created by the off-axis drag force of the low-frequency transducer.

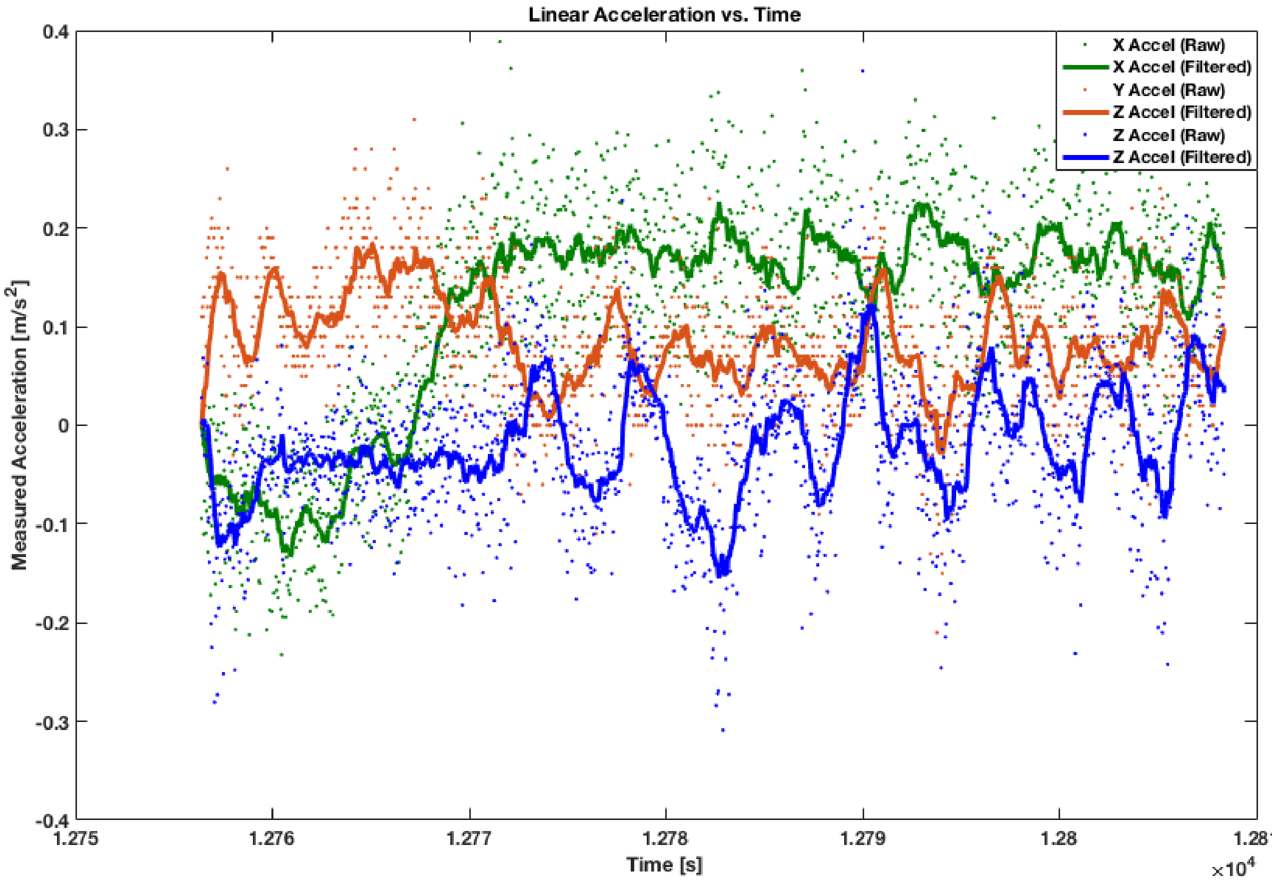

Figure 22: ROV linear acceleration in subsurface release configuration during Flight M. Showing accelerations associated with substantial variation in angular position. Note that the ROV body-fixed coordinate system continues to be defined by the x-axis-to-forward, y-axis-to-starboard, z-axis-to-downward convention.

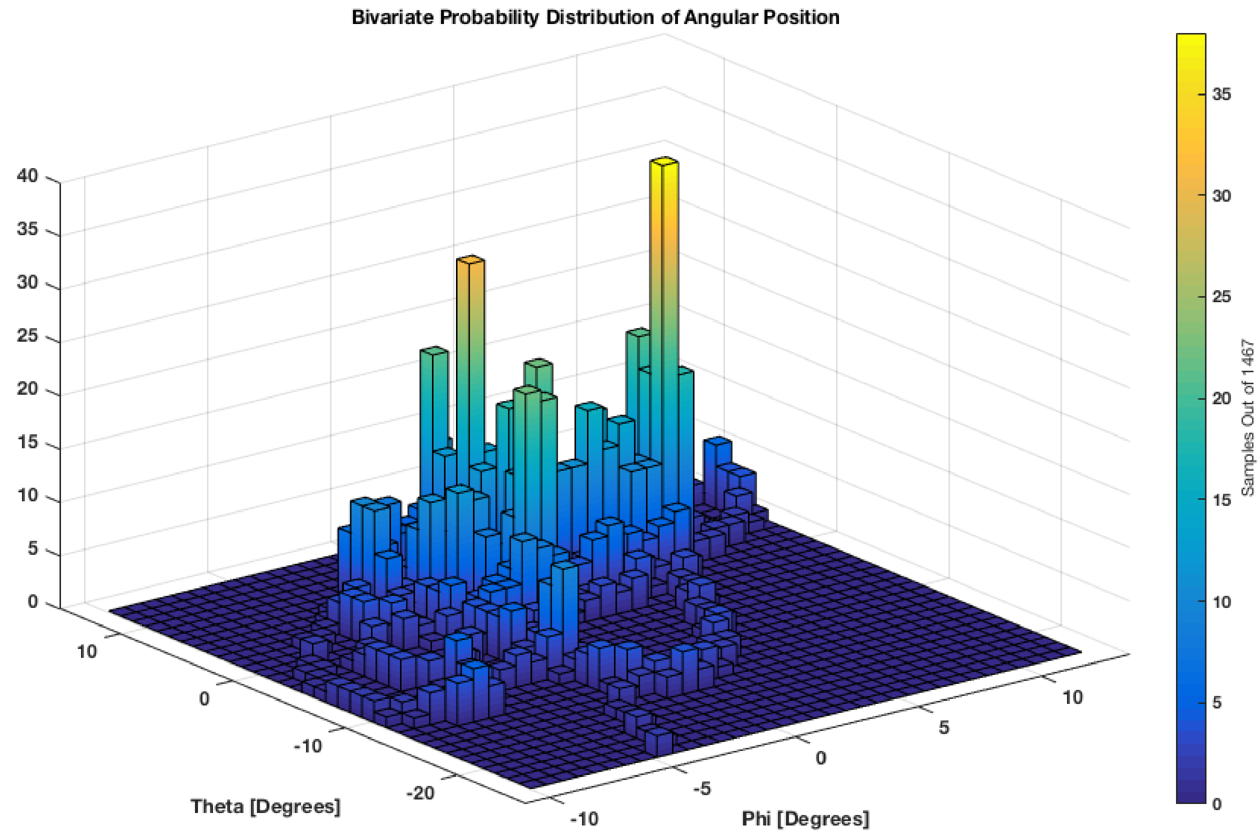

Figure 23: Probability distribution through time of Seabotix ROV angular position in subsurface release configuration during Flight M. Showing a bivariate histogram for pitch (Theta) vs. roll (Phi) derived from the posterior approximation.

References

[1] Diebel, James, 2006, *Representing Attitude: Euler Angles, Unit Quaternions, and Rotation Vectors*, Stanford University, Stanford, CA.

[2] Hover, Franz S., 2016, *Design of Electromechanical Robotic Systems: Worked Problems*, MIT Center for Ocean Engineering, Cambridge, MA.